

**Search for Diphoton Events with Large Missing
Transverse Energy in 6.3 fb^{-1} of $p\bar{p}$ Collisions using
the D0 Detector at the Fermilab Tevatron Collider**

Mark Stephen Cooke

Advisor: Professor John Parsons

Submitted in partial fulfillment of the
requirements for the degree
of Doctor of Philosophy
in the Graduate School of Arts and Sciences

COLUMBIA UNIVERSITY

2010

©2010

Mark Stephen Cooke

All Rights Reserved

ABSTRACT

Search for Diphoton Events with Large Missing Transverse Energy in 6.3 fb^{-1} of $p\bar{p}$ Collisions using the D0 Detector at the Fermilab Tevatron Collider

Mark Stephen Cooke

A search for diphoton events with large missing transverse energy produced in $p\bar{p}$ collisions at $\sqrt{s} = 1.96 \text{ TeV}$ is presented. The data were collected with the D0 detector at the Fermilab Tevatron Collider between 2002 and 2010, and correspond to 6.3 fb^{-1} of integrated luminosity. The observed missing transverse energy distribution is well described by the Standard Model prediction, and 95% C.L. limits are derived on two realizations of theories beyond the Standard Model. In a gauge mediated supersymmetry breaking scenario, the breaking scale Λ is excluded for $\Lambda < 124 \text{ TeV}$. In a universal extra dimension model including gravitational decays, the compactification radius R_c is excluded for $R_c^{-1} < 477 \text{ GeV}$.

Table of Contents

| | |
|--|-----------|
| Foreword | 1 |
| 1 Introduction | 3 |
| 2 The Standard Model | 5 |
| 2.1 Content and Principles of the Standard Model | 5 |
| 2.2 Shortcomings of the Standard Model | 12 |
| 3 Supersymmetry and Extra Dimensions | 16 |
| 3.1 Origins of Supersymmetry and Extra Dimensions | 16 |
| 3.2 Supersymmetry | 17 |
| 3.2.1 General Features of Supersymmetric Models | 17 |
| 3.2.2 Gauge Mediated Supersymmetry Breaking | 22 |
| 3.3 Extra Dimensions | 27 |
| 3.3.1 General Features of Models with Extra Dimensions | 27 |
| 3.3.2 Universal Extra Dimensions | 28 |
| 4 Experimental Apparatus | 34 |
| 4.1 The Tevatron at Fermilab | 34 |
| 4.2 The D0 Detector | 36 |
| 4.2.1 Coordinate System | 37 |
| 4.2.2 Tracking Detectors | 39 |
| 4.2.3 Preshower Detectors | 41 |
| 4.2.4 Calorimeters | 42 |

| | | |
|----------|---|-----------|
| 4.2.5 | Intercryostat Detectors | 46 |
| 4.2.6 | Muon Spectrometer | 47 |
| 4.2.7 | Luminosity Detector | 47 |
| 4.2.8 | Trigger and Data Acquisition System | 48 |
| 5 | Physics Object Reconstruction | 50 |
| 5.1 | Particle Tracks | 50 |
| 5.2 | Collision Vertex | 52 |
| 5.3 | Electromagnetic Objects | 53 |
| 5.4 | Jets | 55 |
| 5.5 | Missing Transverse Energy | 57 |
| 6 | Data Samples and Event Selection | 59 |
| 6.1 | Data Samples | 59 |
| 6.2 | Simulated Samples | 61 |
| 6.3 | Selection of the Diphoton Sample | 65 |
| 6.4 | Selection of Data Control Samples | 69 |
| 6.5 | Primary Vertex Requirement | 71 |
| 6.6 | Requirements to Reduce Instrumental Sources of \cancel{E}_T | 74 |
| 6.6.1 | $\Delta\phi(\text{EM}, \text{EM})$ | 76 |
| 6.6.2 | $\Delta\phi_{\min}(\text{EM}, \cancel{E}_T)$ | 76 |
| 6.6.3 | $\Delta\phi(\text{Leading Jet}, \cancel{E}_T)$ | 79 |
| 6.7 | Selection Efficiency for Signal Events | 80 |
| 7 | Background Estimation | 85 |
| 7.1 | Background Processes with Instrumental \cancel{E}_T | 85 |
| 7.1.1 | Modeling \cancel{E}_T in SM Diphoton Events | 86 |
| 7.1.2 | Modeling \cancel{E}_T in SM Events with Jets Misidentified as Photons | 92 |
| 7.1.3 | Normalization of the Instrumental \cancel{E}_T Contributions | 97 |
| 7.2 | Background Processes with Genuine \cancel{E}_T | 103 |
| 7.2.1 | Modeling \cancel{E}_T in SM Events with a Misidentified Electron | 103 |

| | | |
|----------|---|------------|
| 7.2.2 | SM $W/Z + \gamma\gamma$ Events | 110 |
| 8 | Results | 114 |
| 8.1 | Systematic Uncertainties | 114 |
| 8.2 | Final Search Results | 116 |
| 9 | Conclusions and Outlook | 125 |
| | Bibliography | 127 |
| A | Distributions of Kinematic Variables | 137 |

List of Figures

| | | |
|------|--|----|
| 2.1 | Particle content of the SM | 6 |
| 2.2 | Running of the gauge coupling constants in the SM | 14 |
| 2.3 | Feynman diagram illustrating the divergence of the Higgs mass | 15 |
| 3.1 | Feynman diagrams illustrating divergence cancellation in SUSY models | 19 |
| 3.2 | Running of the gauge coupling constants in the MSSM | 21 |
| 3.3 | Schematic diagram of the sectors in a prototype GMSB model | 22 |
| 3.4 | Feynman diagrams illustrating the generation of SUSY particle masses | 23 |
| 3.5 | Example spectrum of SUSY particle masses in the GMSB model | 24 |
| 3.6 | Diagrams illustrating the production and decay of SUSY particles | 25 |
| 3.7 | GMSB NLO production cross section versus the parameter Λ | 26 |
| 3.8 | Diagrams illustrating orbifold compactification and Kaluza Klein modes | 29 |
| 3.9 | Example spectrum of UED particle masses | 31 |
| 3.10 | Diagrams illustrating the production and decay of UED particles | 32 |
| 3.11 | UED LO production cross section versus the parameter R_c^{-1} | 33 |
| 4.1 | The Tevatron accelerator complex at Fermilab | 35 |
| 4.2 | Side view depiction of the D0 detector | 37 |
| 4.3 | Illustration of the coordinate system used by D0 | 38 |
| 4.4 | Side view depiction of the D0 tracking detectors | 39 |
| 4.5 | Detailed view of the D0 silicon microstrip tracker | 40 |
| 4.6 | Cross sectional view of the D0 preshower detector strips | 42 |
| 4.7 | Cutaway view of the D0 calorimeter system | 43 |

| | | |
|------|--|----|
| 4.8 | Cross sectional view showing the D0 calorimeter segmentation | 44 |
| 4.9 | Diagram depicting the readout electronics for the D0 calorimeter | 45 |
| 4.10 | Diagram showing the location of the D0 luminosity monitors | 48 |
| 4.11 | Flowchart of the D0 trigger and data acquisition system | 49 |
| 5.1 | Schematic illustration of the hits-on-the-road algorithm | 52 |
| 5.2 | Schematic illustration of the EM-CPS pointing algorithm | 55 |
| 5.3 | $\sigma_{\cancel{E}_{T,x}}$ versus $\sqrt{\sum E_T}$ in randomly triggered events | 58 |
| 6.1 | Distributions for several variables used in photon selection | 66 |
| 6.2 | Distributions for variables used to define the track veto | 67 |
| 6.3 | Photon neural net variable in $Z\gamma$ data and several MC samples | 68 |
| 6.4 | Leading EM vs. trailing EM NN distribution in the $\gamma\gamma$ / jet misID sample. | 71 |
| 6.5 | $\Delta Z_{PV}(\text{Truth, Reco})$ and \cancel{E}_T distribution in SM $\gamma\gamma$ MC events | 73 |
| 6.6 | Performance of the EM-CPS pointing algorithm in SM $\gamma\gamma$ MC events | 74 |
| 6.7 | CPS match efficiency and EM-CPS pointing resolution in $Z\gamma$ data | 75 |
| 6.8 | \cancel{E}_T from beam halo events : $\Delta\phi(\text{EM, EM})$ requirement | 77 |
| 6.9 | EM - \cancel{E}_T alignment : $\Delta\phi_{\min}(\text{EM, } \cancel{E}_T)$ requirement | 78 |
| 6.10 | Jet - \cancel{E}_T antialignment : $\Delta\phi(\text{Leading Jet, } \cancel{E}_T)$ requirement | 79 |
| 6.11 | E_T and η_{det} distributions for photons in signal model MC events | 83 |
| 6.12 | \cancel{E}_T distribution in signal model MC events | 84 |
| 7.1 | Example Feynman diagrams for several SM processes | 86 |
| 7.2 | Invariant mass and \cancel{E}_T distributions in ee data events | 87 |
| 7.3 | $Z \rightarrow ee$ and SM $\gamma\gamma$ \cancel{E}_T comparison for events without jets | 88 |
| 7.4 | $Z \rightarrow ee$ and SM $\gamma\gamma$ \cancel{E}_T comparison for events with jets | 89 |
| 7.5 | $Z \rightarrow ee$ and SM $\gamma\gamma$ \cancel{E}_T comparison for all events | 90 |
| 7.6 | \cancel{E}_T distributions in the p17 and p20 ee data samples | 91 |
| 7.7 | ee sample \cancel{E}_T distributions in three ranges of instantaneous luminosity | 91 |
| 7.8 | Number of jet misID events as a function of the IsEM-L definition | 93 |
| 7.9 | jet misID \cancel{E}_T dependence on the IsEM-L definition (p17) | 94 |
| 7.10 | jet misID \cancel{E}_T dependence on the IsEM-L definition (p20) | 95 |

| | | |
|------|--|-----|
| 7.11 | \cancel{E}_T distributions in p17 and p20 jet misID samples | 96 |
| 7.12 | jet misID sample \cancel{E}_T distributions in three ranges of instantaneous luminosity | 96 |
| 7.13 | Normalized \cancel{E}_T distributions for instrumental sources of \cancel{E}_T | 99 |
| 7.14 | Instrumental \cancel{E}_T background prediction and $\gamma\gamma$ data. | 100 |
| 7.15 | χ^2/nDoF of the instrumental \cancel{E}_T prediction fit as a function of purity | 101 |
| 7.16 | Pull values of $\gamma\gamma$ data with respect to the instrumental \cancel{E}_T prediction | 101 |
| 7.17 | Instrumental \cancel{E}_T background prediction with shape uncertainty from purity | 102 |
| 7.18 | Fit to the Z mass peak in the p17 and p20 $e\gamma$ data samples | 104 |
| 7.19 | \cancel{E}_T distribution for p17 and p20 $e\gamma$ samples with predicted components . . . | 105 |
| 7.20 | Transverse mass and photon neural net for $\cancel{E}_T > 30$ GeV $e\gamma$ events | 107 |
| 7.21 | Example Feynman diagrams for SM $p\bar{p} \rightarrow e\nu \gamma + X$ processes. | 108 |
| 7.22 | Figures depicting the presence of FSR $W\gamma$ events in the $e\gamma$ sample | 110 |
| 7.23 | \cancel{E}_T distribution for the $e\gamma$ sample (p17+p20) | 111 |
| 7.24 | Example Feynman diagrams for SM $p\bar{p} \rightarrow W/Z + \gamma\gamma$ processes | 113 |
| 7.25 | \cancel{E}_T distributions for $W + \gamma\gamma$ and $Z + \gamma\gamma$ MC events | 113 |
| 8.1 | \cancel{E}_T distribution in the $\gamma\gamma$ data sample | 118 |
| 8.2 | Illustration of impact of uncertainties on the expected cross section limit . . | 122 |
| 8.3 | GMSB 95% C.L. cross section limit as a function of Λ | 123 |
| 8.4 | UED 95% C.L. cross section limit as a function of R_c^{-1} | 124 |

List of Tables

| | | |
|-----|---|-----|
| 3.1 | Particle content of the MSSM | 20 |
| 4.1 | Several properties of the D0 calorimeters | 45 |
| 6.1 | Data samples used in the analysis | 60 |
| 6.2 | MC samples to model SM processes | 63 |
| 6.3 | MC samples for the GMSB and UED signal models | 64 |
| 6.4 | Categories used to partition the preselected diEM dataset into subsamples . | 69 |
| 6.5 | DiEM data subsample definitions | 70 |
| 6.6 | Number of events in each diEM data subsample | 72 |
| 6.7 | Event selection criteria efficiencies for signal model MC events | 81 |
| 7.1 | Different IsEM-L definitions | 93 |
| 7.2 | Number of predicted and observed $e\gamma$ events with large \cancel{E}_T | 112 |
| 8.1 | Compilation of systematic uncertainties | 115 |
| 8.2 | Expected and observed number of $\gamma\gamma$ events with $\cancel{E}_T > 50$ GeV | 119 |
| 8.3 | Expected and observed number of $\gamma\gamma$ events in three \cancel{E}_T intervals | 119 |
| 8.4 | Expected number of GMSB events for three Λ values | 120 |
| 8.5 | Expected number of UED events for three R_c^{-1} values | 120 |

Acknowledgments

I thank my advisor John Parsons for his relentless guidance, support, and patience, even during the most difficult and frustrating times when I was very stubborn and intolerable. He has taught me invaluable lessons about how to succeed in physics and in life, and though I did not always succeed to put his advice into practice, the lessons will stay with me and guide me in the future. Additionally, I would like to acknowledge the substantial guidance and assistance of Gustaaf Brooijmans and the other Columbia professors on the ATLAS and D0 experiments, Emlyn Hughes and Mike Tuts. Lastly, I would like to acknowledge my undergraduate supervisor, Yury Kolomensky, for setting me on the path that has led me to this point.

I am grateful to the Columbia University faculty and staff for providing an excellent graduate education and experience. In particular, I would like to thank the various members of the Columbia ATLAS and D0 groups over the years for a very positive and enjoyable work environment, as well as close friendships: Seth Caughron, Katherine Copic, Dominik Dannheim, Thomas Gadfort, Heather Gray, Andrew Haas, Zachary Marshall, David Lopez Mateos, Michael Mulhearn, Alex Penson, Kerstin Perez, Valeria Perez Reale, Francesco Spano, Dustin Urbaniec, Eric Williams, Evan Wulf, Lidija Zivkovic.

The work I completed as a graduate student would not have been possible without the assistance of numerous ATLAS and D0 colleagues. Particularly important for this dissertation is the help I received from Xuebing Bu, Arnaud Duperrin, Helenka Przysieznik Frey, Yuri Gerstein, Aurelio Juste, Yurii Maravin, and Maiko Takahashi.

Lastly, I would like to thank my friends, in particular the gang of very close ones I've made over the years while at Columbia and at CERN, Ana, and my family, for their constant love and support.

“A man should look for what is, and not what he thinks should be.”

- Albert Einstein

*“The scientist only imposes two things, namely truth and sincerity,
imposes them upon himself and upon other scientists.”*

- Erwin Schrödinger

To C.M. Cooke

Foreword

My work with the Columbia ATLAS group began in Summer 2005. At this time, the Front End Boards (FEBs) for the readout of the ATLAS Liquid Argon (LAr) Calorimeters were being assembled and tested at Nevis Laboratories, and I participated in this effort [1; 2; 3]. Concurrently, I began a physics study of the feasibility of extracting kinematic endpoint information at ATLAS in a particular decay chain of supersymmetric particles. The result of this analysis is documented in an ATLAS Note [4]. In Summer 2006, I moved to Geneva to work on the ATLAS experiment full-time at CERN. By this time the LAr calorimeters had been installed and instrumented in the ATLAS cavern, and I began commissioning studies with the first cosmic muon data. The measurements probed the ionization energy response uniformity at the level of 2% and timing resolution at the level of 3 ns. This work is documented in an ATLAS Note [5], and I presented these and other related ATLAS results at the CIPANP 2009 conference [6]. After completing the LAr commissioning work, my efforts moved to the ATLAS e/γ combined performance group. I carried out several studies encompassing electron and photon calibration, electromagnetic cluster algorithm performance, and photon identification criteria. My ATLAS contributions surpassed the required service work and as a result I have qualified as an ATLAS author.

In Spring 2009, I moved to the D0 experiment. I participated in the certification of new photon identification criteria that are now used in many physics analyses and described in a D0 Note [7]. For this service work, I was included as an author on a D0 publication [8] documenting a search for Randall-Sundrum gravitons in dielectron and diphoton states. In parallel, I performed a search for physics beyond the Standard Model in diphoton events with large missing transverse energy [9]. The search is the topic of this dissertation, and a

paper [10] describing the results has been submitted to the journal *Physical Review Letters*. Additionally, I recently presented these and other recent results pertaining to supersymmetric models on behalf of the D0 Collaboration at the SUSY10 conference[11].

Chapter 1

Introduction

The Standard Model (SM) is a highly successful theory for describing the interactions of matter with the electromagnetic, weak, and strong forces. Numerous predictions of the SM have been experimentally tested in the forty years since its synthesis, and very few significant deviations have been observed. The model remains incomplete, however, and unsatisfactory in several respects. The shortcomings challenge physicists to search for phenomena that are beyond the scope of the SM. Examples of such phenomena, often termed new or beyond the SM (BSM) physics, are predicted in several SM extensions that address the deficiencies of the model.

This dissertation describes a search for new physics in diphoton ($\gamma\gamma$) events with large missing transverse energy (\cancel{E}_T) produced in proton antiproton ($p\bar{p}$) collisions at a center-of-mass energy of $\sqrt{s} = 1.96$ TeV. The data, corresponding to an integrated luminosity of 6.3 fb^{-1} , were collected with the D0 detector at the Fermilab Tevatron Collider. Limits are derived on two BSM scenarios, namely gauge mediated supersymmetry breaking (GMSB) and universal extra dimensions (UED).

In the SM, the production rate of high transverse momentum $\gamma\gamma$ events with large genuine \cancel{E}_T is small. The primary experimental challenge is to identify, and reduce as much as possible, SM backgrounds which fake the $\gamma\gamma + \cancel{E}_T$ signature. Fake events arise from more common SM processes when certain physics object mismeasurements occur. The strategy adopted in this analysis uses the data to understand and model the backgrounds arising from mismeasurements. Several data control samples are defined that are independent of the

sample of $\gamma\gamma$ candidate events. These control samples are used to develop a SM prediction for the \cancel{E}_T distribution in the $\gamma\gamma$ sample. A signal of BSM physics would be observed as an excess of $\gamma\gamma$ events at high values of the \cancel{E}_T distribution. Events in the $\gamma\gamma$ sample with $\cancel{E}_T > 50$ GeV were not considered until a final prediction for the background estimate in this region was obtained. In the following this is referred to as “blinding” the $\cancel{E}_T > 50$ GeV signal region of the $\gamma\gamma$ sample.

The analysis began in March 2009 with a dataset corresponding to 4.1 fb^{-1} . A portion of the dataset corresponding to 1.1 fb^{-1} was analyzed in a previous D0 search for a GMSB signal in the $\gamma\gamma + \cancel{E}_T$ final state [12]. This portion of the data was unblinded in September 2009 and compared with the published result. The two results were consistent, with the present analysis yielding a 15% improvement in the observed GMSB cross section limit. The two analyses differ in several respects. In the present analysis, upgraded photon identification utilizing a neural net discriminant is employed. This variable is used in the definition of the independent data control samples, and is an integral part of an improved estimate of the background contribution from SM $W(\rightarrow e\nu) + \gamma$ and $W(\rightarrow e\nu) + \text{jet}$ events. Additional event topology requirements are also made to further reduce sources of \cancel{E}_T mismeasurements. Lastly, this analysis is the first to consider the UED signal model.

The methodology of the analysis was finalized and reviewed within the D0 collaboration in May 2010. The data were unblinded in the remaining 3.0 fb^{-1} portion of the 4.1 fb^{-1} dataset on June 5th. While the document for publication was being drafted and internally reviewed, an additional 2.2 fb^{-1} of new data were added to the analysis, yielding a total dataset corresponding to 6.3 fb^{-1} , upon which the final results are based.

The final results of the search are presented in this dissertation, which is organized as follows: Chapter 2 reviews the content and principles of the SM, and Chapter 3 introduces the GMSB and UED signal models. Chapter 4 describes the Tevatron Collider and the D0 detector, while Chapter 5 describes the reconstruction of physics objects. The data and simulated samples analyzed are discussed in Chapter 6, as well as the selection of $\gamma\gamma$ candidate events and independent data control samples. Chapter 7 describes the background estimation procedures. Systematic uncertainties are discussed before the presentation of the search results in Chapter 8, followed by conclusions in Chapter 9.

Chapter 2

The Standard Model

In this chapter, the content and fundamental principles of the SM are reviewed. Emphasis is placed on the role of the principle of local gauge invariance in the development of the model. Some shortcomings of the SM are then discussed. In particular, the difficulty in interpreting the SM as a complete theory at very high energies is examined.

2.1 Content and Principles of the Standard Model

In the SM, matter and force are mathematically represented by functions called fields, defined on a spacetime continuum which consists of three spatial dimensions and one time dimension. The predictions of the model are consistent with the principles of special relativity, and hence are invariant under Lorentz transformations of spacetime coordinates. Further, fields are composed of one or more components, depending on a field property called “spin”, and the components transform in a consistent manner under Lorentz transformations. In addition to being a relativistic field theory, the SM is a quantum field theory. Quantum excitations of the fields are manifested as point-like particles.

The particle content of the SM is shown in Figure 2.1. The matter content consists of three generations of spin-1/2 Dirac fermions. The electron and electron neutrino constitute the first generation of leptons. The pattern of a lepton with one unit of elementary electric charge paired with a neutral lepton is repeated in the second and third generations with the muon and tau leptons and their corresponding neutrinos. Charged leptons participate

**Three Generations
of Matter (Fermions)**

| | I | II | III | |
|----------------|---|---|---|---------------------------------------|
| mass→ | 2.4 MeV | 1.27 GeV | 171.2 GeV | 0 |
| charge→ | $\frac{2}{3}$ | $\frac{2}{3}$ | $\frac{2}{3}$ | 0 |
| spin→ | $\frac{1}{2}$ | $\frac{1}{2}$ | $\frac{1}{2}$ | 1 |
| name→ | u up | c charm | t top | γ photon |
| | | | | |
| | 4.8 MeV | 104 MeV | 4.2 GeV | 0 |
| | $-\frac{1}{3}$ | $-\frac{1}{3}$ | $-\frac{1}{3}$ | 0 |
| | $\frac{1}{2}$ | $\frac{1}{2}$ | $\frac{1}{2}$ | 1 |
| Quarks | d down | s strange | b bottom | g gluon |
| | | | | |
| | <2.2 eV | <0.17 MeV | <15.5 MeV | 91.2 GeV ⁰ |
| | 0 | 0 | 0 | 0 |
| | $\frac{1}{2}$ | $\frac{1}{2}$ | $\frac{1}{2}$ | 1 |
| | ν_e electron neutrino | ν_μ muon neutrino | ν_τ tau neutrino | Z⁰ weak force |
| | | | | |
| | 0.511 MeV | 105.7 MeV | 1.777 GeV | 80.4 GeV |
| | -1 | -1 | -1 | ± 1 |
| | $\frac{1}{2}$ | $\frac{1}{2}$ | $\frac{1}{2}$ | 1 |
| Leptons | e electron | μ muon | τ tau | W[±] weak force |
| | | | | Bosons (Forces) |

Figure 2.1: The matter content of the SM consists of three generations of spin-1/2 fermions, while forces are mediated by spin-1 bosons. The electromagnetic, weak, and strong forces are mediated by the photon, W^\pm and Z bosons, and gluons respectively.

in both the electromagnetic and weak interactions, while neutrinos only participate in the weak interaction. The other type of fundamental fermion, quarks, participate in the strong interaction in addition to the electromagnetic and weak interactions. Free quarks have not been directly detected, as they are confined by the strong force within hadrons. Examples of hadrons containing up and down quarks of the first generation are the proton, neutron, and pion. Similar to the lepton pairs, each generation contains two quarks which differ by one unit in electric charge. However, each quark carries a fraction, either $\frac{2}{3}$ or $\frac{1}{3}$ in absolute value, of the elementary electric charge. The second generation contains charm and strange quarks, and the third generation contains top and bottom quarks.

Forces are mediated by spin-1 bosons, also called vector or gauge bosons. SM interactions between the fermions and vector bosons, as well as vector bosons amongst themselves, follow from the principle of local gauge invariance [13]. This principle is illustrated by considering a spin-1/2 fermion field, ψ , of mass m , described by the Dirac Lagrangian,

$$\mathcal{L}_1 = i\bar{\psi}(\gamma^\mu\partial_\mu)\psi - m\bar{\psi}\psi. \quad (2.1)$$

Local gauge invariance stipulates that the Lagrangian be invariant (up to a total derivative) under changes in the phase of the field ψ that depend on the spacetime coordinate x ,

$$\psi(x) \rightarrow e^{i\lambda(x)}\psi(x). \quad (2.2)$$

When placed in the Lagrangian, however, the transformed field produces an extra term,

$$- \bar{\psi}\gamma^\mu\psi(\partial_\mu\lambda), \quad (2.3)$$

demonstrating that \mathcal{L}_1 is not locally gauge invariant. Consider adding a massless vector field, A_μ , to the single fermion model,

$$\mathcal{L}_2 = i\bar{\psi}(\gamma^\mu\partial_\mu)\psi - m\bar{\psi}\psi - \bar{\psi}(g_e\gamma^\mu A_\mu)\psi - \frac{1}{4}F_{\mu\nu}F^{\mu\nu}, \quad (2.4)$$

where the last term represents the kinetic energy of A_μ , with $F_{\mu\nu} = \partial_\mu A_\nu - \partial_\nu A_\mu$, and the third term an interaction between ψ and A_μ . The simultaneous transformations

$$\begin{aligned} \psi &\rightarrow e^{i\lambda}\psi \\ A_\mu &\rightarrow A_\mu + \frac{1}{g_e}\partial_\mu\lambda, \end{aligned} \quad (2.5)$$

leave \mathcal{L}_2 invariant, where the A_μ transformation corresponds to the gauge freedom observed in the classical theory of electrodynamics. Local phase transformations of the fermion field are thus compensated by a corresponding gauge transformation of the vector field.

Noether's theorems relate Lagrangian symmetries to conservation laws. \mathcal{L}_2 is actually the Lagrangian of Quantum Electrodynamics (QED), and the fields ψ and A_μ represent the electron and photon respectively. The quantity g_e represents electric charge. Noether's first theorem reveals that the conservation of electric charge is a consequence of global phase invariance, while her second theorem dictates that local phase (gauge) invariance implies new gauge fields.

Isospin is a concept introduced by Heisenberg in 1932 to explain the symmetric properties of the proton and neutron in the strong interaction, despite their distinction in the electromagnetic interaction and small mass difference. In 1954, Yang and Mills examined the consequence of promoting the approximate global isospin symmetry of the strong interaction to a local gauge symmetry [14]. The model consists of two spin- $1/2$ fermion fields, representing the proton and neutron. In analogy with Equation 2.2, the two fermion Lagrangian is stipulated to be invariant under the transformation

$$\psi(x) \rightarrow U(x)\psi(x), \quad (2.6)$$

where ψ is a doublet of fermion fields and U is a 2×2 unitary matrix with unit determinant. The phase transformation of QED, which constitutes an element of the Abelian group $U(1)_{em}$, is thus generalized to the non-Abelian group $SU(2)$. Local gauge invariance is obtained by introducing three massless gauge fields coupled to the isospin doublet ψ , one for each generator of the $SU(2)$ algebra, and each coupling with a common strength. The resulting Lagrangian resembles the QED Lagrangian of Equation 2.4, though the term analogous to the gauge boson kinetic energy contains, in addition to the kinetic energy of the three vector bosons, terms representing interactions between the gauge bosons. These self-interaction terms are a consequence of the non-Abelian nature of $SU(2)$.

Although the $SU(2)$ model of Yang and Mills did not yield a successful model of the strong interaction, the seminal work laid the foundation for the non-Abelian gauge theories of the electroweak and strong interaction in the SM. In 1958, Bludman applied the Yang-Mills model to the weak interaction [15]. In accordance with the observed parity violating structure of the weak interaction, Bludman proposed a local $SU(2)_L$ gauge invariant model with the transformation of Equation 2.6 acting only on left-handed weak-isospin doublets. These doublets remain fundamental ingredients of the SM, composed of the left-handed portions of the spin- $1/2$ quarks and leptons of each generation, *e.g.* (u_L, d_L) and (ν_e, e_L) . Bludman's $SU(2)_L$ model accurately predicted the weak interactions mediated by charged vector bosons (W^\pm) and implied the existence of an electrically neutral weak interaction. The short range of the weak force suggested the three weak vector bosons are massive. Explicit mass terms for vector bosons and fermions are not $SU(2)_L$ gauge invariant, however, and a solution to this obstacle was not provided.

In 1961, Glashow proposed a model of the electromagnetic and weak interactions using the gauge group $SU(2)_L \times U(1)_Y$ [16]. Although Bludman's $SU(2)_L$ model contains a neutral current interaction, it cannot be identified with electromagnetism as it only couples to left-handed currents. With an additional $U(1)_Y$ gauge symmetry, called weak hypercharge, the neutral $SU(2)_L$ boson, W_μ^3 , and the $U(1)_Y$ gauge boson, B_μ , are capable of forming orthogonal physical states A_μ and Z_μ ,

$$\begin{pmatrix} A_\mu \\ Z_\mu \end{pmatrix} = \begin{pmatrix} \cos \theta_w & \sin \theta_w \\ -\sin \theta_w & \cos \theta_w \end{pmatrix} \begin{pmatrix} W_\mu^3 \\ B_\mu \end{pmatrix}. \quad (2.7)$$

The mixing angle, θ_w , is not determined in the model. However, if one identifies A_μ with the photon coupling to the electromagnetic current with strength g_e , the $SU(2)_L$ coupling strength g_2 and the $U(1)_Y$ coupling strength g_1 must be related to g_e by

$$g_e = g_2 \sin \theta_w = g_1 \cos \theta_w. \quad (2.8)$$

The electromagnetic current is therefore interpreted as a combination of the neutral weak isospin current and the weak hypercharge current. In terms of the electric charge, Q , the relation is

$$Q = T_3 + \frac{1}{2}Y. \quad (2.9)$$

The eigenvalues of T_3 are $+\frac{1}{2}$ ($-\frac{1}{2}$) for the top (bottom) component of a weak isospin doublet, and thus the doublet (ν_e, e_L) carries hypercharge $Y = -1$. Likewise, the $SU(2)_L$ singlet e_R has $T_3 = 0$ and $Y = -2$. Glashow's proposition of a combined electroweak model constitutes a key development in the formulation of the SM. However, an explanation was not provided for why $U(1)_{em}$ appears to be a symmetry subgroup of a larger inexact symmetry group $SU(2)_L \times U(1)_Y$, nor a mechanism to generate gauge invariant mass terms for the gauge bosons and fermions.

Motivated by developments in the theory of superconductivity, Nambu proposed a framework [17] in the early 1960s to describe the generation of hadronic masses by postulating a Lagrangian symmetry that is not manifest in the ground state of the theory. A few years later, Higgs [18] and others [19] capitalized on an idea by Anderson [20], demonstrating that earlier problems with unwanted massless "Goldstone" bosons [21] in such models could be avoided if the hidden symmetry is local gauge invariance. Although these

efforts were carried out in the context of the generation of hadronic masses, Weinberg [22] and Salam [23] had the insight to apply the ideas to the electroweak model first proposed by Glashow.

To implement the hidden symmetry mechanism in the Glashow-Weinberg-Salam (GWS) model, a spin-0 (also referred to as complex scalar) weak isospin doublet ϕ with weak hypercharge $Y = 1$ is introduced to the $SU(2)_L \times U(1)_Y$ model. In the vacuum (ground) state, the potential energy $V(\phi)$ is assumed to achieve a minimum at a non-zero value $|\phi_0|$,

$$\phi = \begin{pmatrix} \phi^+ \\ \phi^0 \end{pmatrix} \quad \rightarrow \quad \phi_0 = \sqrt{\frac{1}{2}} \begin{pmatrix} 0 \\ v \end{pmatrix}, \quad (2.10)$$

where v is a constant referred to as the electroweak vacuum expectation value (v.e.v.). Excitations from the ground state are of the form $v \rightarrow v + h$, where h is a real scalar field called the Higgs field. The form of ϕ_0 in Equation 2.10 is not general, but any other parameterization with $|\phi_0| = \frac{1}{2}v^2$ can be transformed to this form by a suitable gauge transformation. Writing the GWS Lagrangian with this choice of ϕ_0 , one identifies the following masses for the four electroweak gauge bosons,

$$M_{W^\pm} = \frac{1}{2}vg_2 \quad (2.11)$$

$$M_Z = \frac{1}{2}v\sqrt{g_1^2 + g_2^2} \quad (2.12)$$

$$M_A = 0. \quad (2.13)$$

The W^\pm and Z bosons thus obtain masses proportional to v , while the photon remains massless. From the measured values of the weak gauge boson masses and the coupling constants g_2 and g_1 , the electroweak v.e.v. is determined to be $v = 246$ GeV. The chosen parameterization of ϕ_0 makes the physical content of the model evident, allowing for three of the four degrees of freedom of the field ϕ to be associated with the longitudinal degrees of freedom of the W^\pm and Z bosons, which appear massive in the vacuum state. The association is achieved at the expense of manifest $SU(2)_L \times U(1)_Y$ gauge invariance. The vacuum state is neutral, however, so $U(1)_{em}$ gauge invariance is preserved.

In the early 1970s, the consistency of general Yang-Mills theories was placed on stable theoretical footing. t'Hooft and Veltman demonstrated that Yang-Mills theories could be regulated and renormalized [24], both in the case of massless gauge bosons and in the case

of massive gauge bosons in models with hidden gauge symmetry. In the study of the higher order behavior of these models, the importance of the fermion content was also elucidated. Potentially dangerous anomalies [25] were avoided by a suitable choice of fermion content. The GWS model is free of such anomalies if it contains complete fermion generations [26] consisting of one lepton weak-isospin doublet and three quark weak-isospin doublets, where the quarks of each doublet carry the same of three possible types of “colors”.

The ideas of quarks [27] and color symmetry [28] had been introduced in the mid-1960s, and provided a very successful phenomenological framework for understanding data describing hadronic states. A non-Abelian gauge theory of the strong interactions, called Quantum Chromodynamics (QCD), emerged shortly after the work of t’Hooft and Veltman. The model is based on the color symmetry group $SU(3)_c$, with the strong force mediated by eight massless gauge bosons called gluons. Quarks, color symmetry, and subsequently QCD, became widely accepted after Gross and Wilczek, and independently Politzer, demonstrated that Yang-Mills theories may become, depending on the particle content, non-interacting at high energies. This property, referred to as asymptotic freedom [29], explained scaling behavior [30] observed in deep inelastic scattering experiments [31] which suggested that nearly free point-like spin- $1/2$ particles (*i.e.* quarks) are confined within hadrons. The function $\beta(\alpha)$ encodes the dependence of the coupling constant, g , on the energy scale of a given process, μ , and is given by

$$\beta(\alpha) \equiv \mu \frac{d}{d\mu} g(\alpha) = \frac{\alpha^2}{\pi} b_1 + \left(\frac{\alpha^2}{\pi} \right)^2 b_2 + \dots; \quad \alpha = \frac{g^2}{4\pi}. \quad (2.14)$$

For a non-Abelian gauge theory with gauge group $SU(N)$, Gross, Wilczek, and Politzer computed the coefficient b_1 , which depends on N , the representation of the group, and the particle content of the theory. They found that $b_1 < 0$ is generally possible, and hence so is asymptotic freedom. QCD as a fundamental theory of the strong interactions was the last major theoretical ingredient in the formulation of the SM, a local gauge theory of the strong and electroweak interactions.

The SM is based on the direct product of gauge groups $SU(3)_c \times SU(2)_L \times U(1)_Y$, and contains three complete generations of fermions. The model contains 19 free parameters that must be experimentally determined. These parameters can be categorized as “gauge sector” and “Higgs sector” parameters. The four parameters in the gauge sector are the

three gauge coupling constants g_3 , g_2 , g_1 , and a QCD parameter whose value is not known but is experimentally limited to be very close to zero. Of the 15 parameters of the Higgs sector, two values, the electroweak v.e.v. and the Higgs boson mass, m_h , parameterize the potential energy $V(\phi)$. The remaining 13 values parameterize the Yukawa-type interactions of ϕ with the fermion fields, with 9 representing fermion masses (six quark and three lepton), while the remaining four relate the weak and mass eigenstates of the down-type quarks.

The properties and interactions of the SM particles have been extensively studied [32]. In particular, precision measurements of the electroweak interactions are in excellent agreement with SM predictions [33]. The Higgs sector, however, remains the least well tested. This sector contains many arbitrary parameters, such as the masses of the fermions, which span several orders of magnitudes. Further, excitations of the Higgs field (*i.e.*, the Higgs boson) have yet to be experimentally observed. Thus, despite its many successes, the SM is still regarded as an incomplete theory.

2.2 Shortcomings of the Standard Model

In 1974, almost immediately after the discovery of asymptotic freedom, and the proposal of QCD as a non-Abelian gauge theory for the strong interactions, Georgi and Glashow suggested a unified model based on a single gauge group, $SU(5)$ [34]. The model contains a single coupling constant, embeds the SM gauge groups in a simple (in the mathematical sense) group, allows for multiplets containing both leptons and quarks, is free of anomalies, and makes a definite prediction for the weak mixing angle (an independent attempt at unification with a semi-simple gauge group was made a year earlier by Pati and Salam [35]). Even before predictions of the GWS model and QCD began to be tested and confirmed, the $SU(5)$ proposal addressed certain shortcomings of the SM. Such shortcomings are not necessarily inconsistencies of the model, or predictions in conflict with observation. They may be seemingly arbitrary features of the model that are expected to be explained in a more unified theory, such as the Georgi-Glashow proposal.

In order to unify the three forces in this manner, referred to as grand unification, an explanation must be provided for the significant differences in the values of the SM coupling

constants. Asymptotic freedom suggests that the differences may be viewed as a low energy phenomenon, a result of additional hidden symmetries of the larger gauge group which are not evident at low energies but are only manifested at higher energies. Soon after the Georgi-Glashow proposal, Georgi, Quinn, and Weinberg used Equation 2.14 to predict the dependence, or “running”, of the SM gauge coupling constants on energy [36]. The dependence is shown in Figure 2.2. The values of the coupling constants nearly, but not quite, converge at $\approx 10^{14}$ GeV. The measured values of the constants at low energy were not known with sufficient precision in the original calculation to conclude if the extrapolation converged to a common value or not. Within the uncertainty at the time, a universal value was suggested at this high scale, not far below the Planck scale ($M_P = 2.4 \times 10^{18}$ GeV) where quantum gravitational effects are expected to become important. The grand unified theory (GUT) hypothesis therefore aroused interest, and the GUT scale was considered a plausible scale to consider for physics beyond the SM.

The authors noted [36] an important issue that unification raises, although they did not address it quantitatively. The issue concerns the origin of two distinct scales, a low scale associated with the masses of the electroweak gauge bosons, characterized by $M_Z \approx 10^2$ GeV, and a high scale associated with the masses of the gauge bosons corresponding to the non-SM generators of the GUT group, assumed to be $M_{GUT} \approx 10^{14}$ GeV. Postulating a unified framework is the first step. The difficult second step is to provide a mechanism to generate two scales of such different magnitudes. Gildener [37] pointed out a difficulty in constructing GUT models with vastly different scales, termed a gauge-symmetry hierarchy, when fundamental scalar fields which obtain v.e.v.’s are employed as in the SM. Perturbative instabilities occur for hierarchies of arbitrary magnitude, and a bound may be derived on the magnitude of the hierarchy in terms of the gauge coupling strength. The ratio $M_Z/M_{GUT} \approx 10^{-12}$ is many orders of magnitude below this bound and thus presents an obstacle in the construction of realistic GUT models.

Susskind [38] pointed out an additional problem with fundamental scalar fields, such as the Higgs field. The problem is related to, but distinct from, the gauge-hierarchy problem. In the SM, the issue concerns the sensitivity of m_h to variations of the energy scale. Suppose that the SM is an effective theory that approximates a more fundamental theory (FT), and

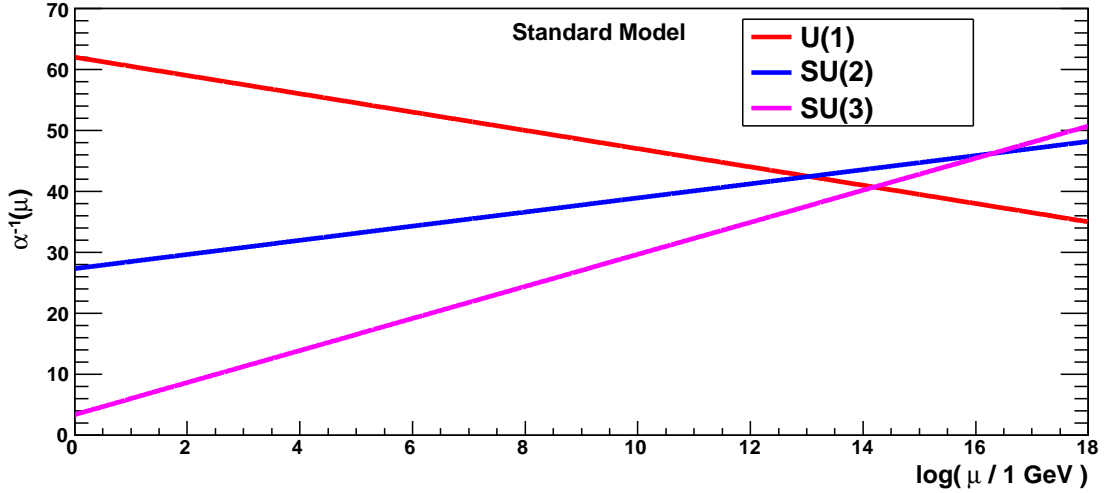


Figure 2.2: The dependence of the gauge coupling constants on energy in the SM. For each SM gauge group, the inverse of the fine structure constant, α , defined in terms the coupling constant g in Equation 2.14, is shown as a function of the energy scale parameter μ .

the approximation is valid up to a scale μ_{FT} . In analogy with the scale dependence of the coupling constant, one can use the squared Higgs mass at the scale of the fundamental theory, $m_h^2(\mu_{FT})$, to calculate the same quantity one would measure at the electroweak scale, $m_h^2(\mu_{EW} \approx v)$. The relationship [39] is

$$m_h^2(\mu_{EW}) = m_h^2(\mu_{FT}) + Cy^2 \int_{\mu_{EW}^2}^{\mu_{FT}^2} dk^2 + Ry^2 + \mathcal{O}(y^4), \quad (2.15)$$

where y is a coupling constant, C is dimensionless, and R grows approximately logarithmically with μ_{FT} . The problem Susskind emphasized is that the term proportional to C diverges quadratically as $\mu_{FT} \rightarrow \infty$. In the SM, a major contribution to this quadratically dependent term is from diagrams with a virtual fermion loop, as shown in Figure 2.3. In the limit $\mu_{FT} \gg \mu_{EW}$, a natural value of the squared Higgs mass would be $m_h^2(\mu_{EW}) \approx \mu_{FT}^2$. A value at the weak scale, $m_h^2(\mu_{EW}) \approx \mu_{EW}^2$, requires the value of $m_h^2(\mu_{FT})$ be very similar in magnitude to the divergent term. For the hierarchy of scales suggested by grand unification, the degree of similarity is at the level of the 24th decimal place. Such fine-tuning is considered “unnatural”, and the absence of a high degree of fine tuning is considered by many to be a requirement of a correct theory.

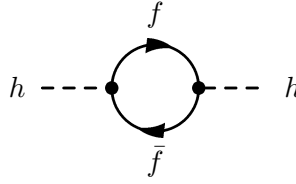


Figure 2.3: A Feynman diagram depicting the contribution from a virtual fermion (f) loop to the dependence of the squared Higgs mass on the energy scale.

Although GUT models deepen the structure relating the constituents of the SM, the scale at which the complete symmetry becomes manifest is evidently extraordinarily high. The standard method for generating a distinct scale, by means of a scalar field and a v.e.v., is not just problematic for GUT models, but also for any other BSM model whose fundamental scale is much larger than the electroweak scale. For example, a theory that encompasses the SM and gravity must address fine tuning associated with the scale M_P . As the Higgs sector of the SM contains the most number of arbitrary features, and the Higgs boson has yet to be observed, the uncertainty in the role of fundamental scalar fields currently represents one of the greatest shortcomings of the SM.

Despite its many successes, the Standard Model is an incomplete theory. Beyond the unappealing features of 19 free parameters, disparate gauge groups and fermion multiplets, and the fine tuning required at high energies, the SM does not address, for example, the origins of dark matter, dark energy, the prevalence of matter over antimatter in the universe, neutrino masses, and gravity. In the next chapter, two major BSM scenarios are examined, namely supersymmetry and extra dimensions. Supersymmetry has the attractive features of predicting a more precise convergence of the gauge coupling constants at the scale M_{GUT} , while avoiding the naturalness problem. Some models with extra dimensions predict that the Planck mass is large as a result of geometric effects, and that the dynamics of a more complete theory including quantum gravity may be revealed at, or just beyond, the electroweak scale. Although these two scenarios do not address all the shortcomings of the SM, they do create a richer theoretical structure to explore, and make interesting new predictions that can be experimentally tested.

Chapter 3

Supersymmetry and Extra Dimensions

This chapter introduces two major theoretical constructs, supersymmetry (SUSY) and extra dimensions. The two ideas underlie a considerable number of proposed BSM scenarios, and developed from a common line of theoretical research, the early history of which is briefly recounted. General features of SUSY models are described next, followed by an examination of the GMSB scenario. GMSB predictions for collider signatures, specifically in the $\gamma\gamma + \cancel{E}_T$ final state, are motivated. Similarly, some general aspects of models with extra dimensions are described, followed by a more detailed treatment of the second signal model of the analysis, the UED scenario.

3.1 Origins of Supersymmetry and Extra Dimensions

The SUSY transformation, and the modern motivation for models with extra dimensions, originated during investigations of the dual resonance model [40], which emerged in the late 1960s as a part of the analytic S-matrix approach [41] to formulating a theory of the strong interaction. Although QCD ultimately became widely accepted as the fundamental theory of the strong interaction, important theoretical ideas arose from this line of research that later spawned new perspectives for addressing the shortcomings of the SM.

In 1971, Ramond succeeded in formulating a dual model for fermions [42], and Neveu

and Schwarz reformulated and improved the bosonic dual resonance model [43]. Gervais and Sakita [44] noted a symmetry property, which they termed “super-gauge” invariance, of the combined Ramond-Neveu-Schwarz model. A separate line of research in the U.S.S.R. independently discovered the SUSY transformation and investigated its consequences [45].

In parallel with the developments that revealed SUSY invariance, other researchers were examining additional interesting properties of the dual resonance model. In 1970, Nambu, Nielson, and Susskind each independently formulated the dual resonance model in terms of the dynamics of strings [46]. Lovelace demonstrated that the original bosonic model required at least 26 dimensions in order to exhibit unitarity, a feature he described as “obviously unworldly” [47]. Goddard and Thorn quickly extended this result to the Ramond-Neveu-Schwartz model, where the additional symmetry reduced the requirement to 10 dimensions [48]. Despite the continued necessity of extra dimensions and the emergence of QCD, research on these models continued. Scherk and Schwartz relaxed the interpretation of the dual model as strictly a theory of hadrons, and revealed that a spin-2 state in the model could describe the gravitational force [49]. Shortly after, Cremmer and Scherk noted that the extra dimensions could be made compact and “compatible with everyday experience” [50]. The seeds for the subsequent “string revolutions” were sown which in turn motivated later phenomenological models with compact extra dimensions that may be accessible at, or even below, the electroweak scale.

3.2 Supersymmetry

In 1974, Wess and Zumino investigated the question of whether the super-gauge transformation of the Ramond-Neveu-Schwarz dual model could be defined in four dimensions. They abstracted the algebra generated by the transformation, and examined the consequences of representing the algebra as transformations on fields in conventional spacetime [51].

3.2.1 General Features of Supersymmetric Models

A SUSY transformation turns a fermionic state into a bosonic state and vice versa,

$$Q|\text{Boson}\rangle = |\text{Fermion}\rangle \quad Q|\text{Fermion}\rangle = |\text{Boson}\rangle, \quad (3.1)$$

where Q is an operator with fermion properties under Lorentz transformations. The operator Q and its hermitian conjugate, Q^\dagger , generate an algebra satisfying the following relations,

$$\{Q, Q^\dagger\} = P^\mu \quad (3.2)$$

$$\{Q, Q\} = \{Q^\dagger, Q^\dagger\} = 0 \quad (3.3)$$

$$[P^\mu, Q] = [P^\mu, Q^\dagger] = 0, \quad (3.4)$$

where P^μ is the four momentum operator, a generator of the Poincaré spacetime symmetry group, and spinor indices have been suppressed. Coleman and Mandula [52] proved a theorem prohibiting non-trivial relations between spacetime and internal symmetries. However, the anti-commutation relations (represented by $\{X, Y\}$) bypass certain assumptions of the Coleman-Mandula theorem. Haag, Lopuszanski, and Sohnius [53] demonstrated that the SUSY transformation is a valid extension of the known symmetries of spacetime.

Supersymmetric field theories, such as the original one introduced by Wess and Zumino, exhibit several remarkable properties. In particular, a “non-renormalization theorem” was proved [54]. An example of this theorem is illustrated by the fine tuning problem of the Higgs mass in the SM discussed previously. In a theory invariant under SUSY transformations, there must be a corresponding boson to each fermion, and this boson must be of equal mass to the fermion and carry identical internal quantum numbers, such as gauge quantum numbers. If the (Dirac) fermion is part of a “chiral supermultiplet”, then it has two associated scalar boson partners, one for each spin degree of freedom. If the fermion is part of a “vector supermultiplet”, it has a vector boson partner, also with two spin degrees of freedom. In the case of the Higgs boson mass correction, the divergent diagram with a fermion loop, shown again in Figure 3.1(a), is canceled by corresponding diagrams with the scalar “superpartners” of the fermion, as shown in Figure 3.1(b). In other words, $C = 0$ in Equation 2.15.

A supersymmetric generalization of the SM [55] therefore requires the introduction of new particles. The particle content of the minimal supersymmetric SM (MSSM) is listed in Table 3.1. The correspondence between SM particles and their superpartners is straightforward, except that two Higgs doublets are required to give masses to fermions. Revisiting the discussion of the running of the gauge coupling constants of the SM, the addition of

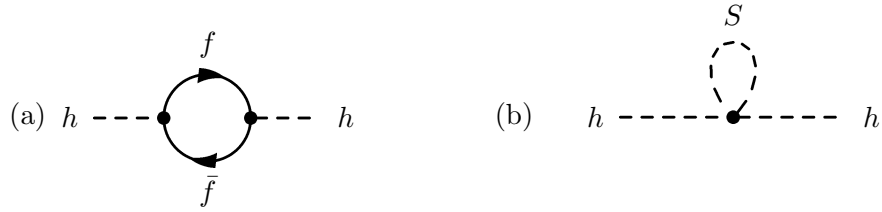


Figure 3.1: A Feynman diagram (a) depicting the contribution from a virtual fermion (f) loop to the dependence of the squared Higgs mass on the energy scale. This diagram is canceled in SUSY models by a corresponding diagram (b) with a virtual scalar (S) loop.

new particle content modifies the coefficients in Equation 2.14. An interesting consequence of the MSSM particle content is that the three coupling constants converge to a common value much more precisely [56], as shown in Figure 3.2.

Although the MSSM has attractive properties that motivate it as a possible extension to the SM, particles differing by half-integer spin that are degenerate in mass with the SM particles have not been observed. If they exist, they must be more massive, perhaps just above the electroweak scale. SUSY invariance can be explicitly broken by introducing “soft terms” in the Lagrangian, such as mass terms for the superpartners, without invalidating certain conclusions of the non-renormalization theorem [57]. The most general parameterization contains 105 new free parameters [58]. Once SUSY breaking terms are present, the mechanism to hide electroweak symmetry in the ground state occurs radiatively. Each Higgs doublet obtains a v.e.v., and their ratio is defined as $\tan\beta$. The sign of the Higgsino mass term, $sgn(\mu)$, is undetermined and is an important parameter characterizing the electroweak sector. Of the eight degrees of freedom of the two Higgs doublets, three become associated with the longitudinal degrees of freedom of the weak gauge bosons, leaving five observable Higgs fields (h, H, H^\pm, A). Additionally, some SUSY particles mix to form mass eigenstates. The electroweak gauginos and Higgsinos mix to form neutralinos ($\chi_1^0, \chi_2^0, \chi_3^0, \chi_4^0$), and charginos (χ_1^\pm, χ_2^\pm). Mixing also occurs between the chiral eigenstates of the sfermions. The effect is most relevant for the third generation sfermions.

An additional assumption of the MSSM is that of R-parity [59] conservation. R-parity is a multiplicative quantum number, and SM particles have positive R-parity, while SUSY particles have negative R-parity. In the SM, gauge invariance and renormalizability result in

| Chiral Supermultiplets | | | |
|------------------------|--|--|------------------------------------|
| Name | Spin-0 | Spin-1/2 | SU(3) \times SU(2) \times U(1) |
| squarks, quarks | $\tilde{Q} = (\tilde{u}_L, \tilde{d}_L)$ | $Q = (u_L, d_L)$ | (3, 2, 1/3) |
| | \tilde{u}_R^* | \bar{u}_R | ($\bar{3}$, 1, -4/3) |
| | \tilde{d}_R^* | \bar{d}_R | ($\bar{3}$, 1, 2/3) |
| sleptons, leptons | $\tilde{L} = (\tilde{\nu}, \tilde{e}_L)$ | $L = (\nu, e_L)$ | (1, 2, -1) |
| | \tilde{e}_R^* | \bar{e}_R | (1, 1, 2) |
| Higgs, Higgsinos | $H_u = (H_u^+, H_u^0)$ | $\tilde{H}_u = (\tilde{H}_u^+, \tilde{H}_u^0)$ | (1, 2, 1) |
| | $H_d = (H_d^0, H_d^-)$ | $\tilde{H}_d = (\tilde{H}_d^0, \tilde{H}_d^-)$ | (1, 2, -1) |
| Vector Supermultiplets | | | |
| Name | Spin-1/2 | Spin-1 | SU(3) \times SU(2) \times U(1) |
| gluino, gluon | \tilde{g} | g | (8, 1, 0) |
| winos, W's | $\tilde{W}^\pm, \tilde{W}^0$ | W^\pm, W^0 | (1, 3, 0) |
| bino, B | \tilde{B} | B | (1, 1, 0) |

Table 3.1: The particle content of the MSSM. The SM fermions are part of chiral supermultiplets (top), with the spin-0 partners of the leptons and quarks referred to as sleptons and squarks, respectively. The partners of the Higgs bosons have spin- $\frac{1}{2}$ and are called Higgsinos. The SM gauge bosons are part of vector supermultiplets (bottom), with the spin- $\frac{1}{2}$ superpartners referred to as gauginos. The gauge quantum numbers of the supermultiplets are given in the last column.

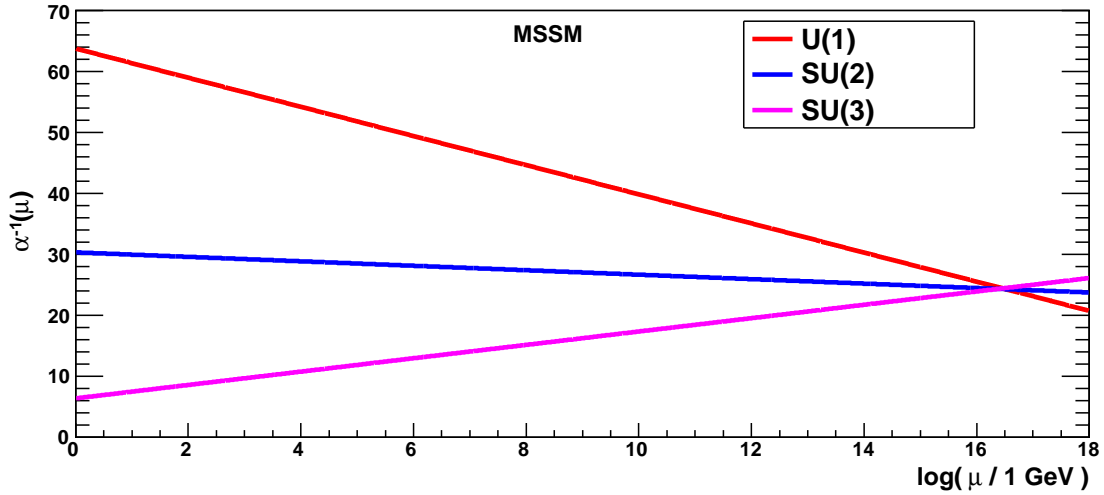


Figure 3.2: The dependence of the gauge couplings on energy in the MSSM. See the caption of Figure 2.2 and text for further details.

the conservation of lepton and baryon number. In a SUSY extension to the SM, soft terms may be added [60] to the Lagrangian which violate both and could allow for an unacceptable rate of proton decay. These terms are not present if R-parity is conserved. In this case, SUSY particles are only produced in pairs at colliders, and must decay to another SUSY particle and one or more SM particles. An important consequence of R-parity conservation is the stability of the lightest SUSY particle (LSP), which, if neutral, could serve as a dark matter candidate [61]. R-parity conservation is assumed in the following.

Proposing new unobserved superpartners and over a hundred new free parameters does not suggest progress towards a deeper description of nature. However, one expects that the MSSM with soft SUSY breaking terms parameterizes the vacuum state of a SUSY invariant theory that contains the MSSM and some additional sectors, and that properties and symmetries of the full theory dictate the values of the free parameters. Further, SUSY may be promoted from a global to a local symmetry. As SUSY is a spacetime symmetry, the coordinate transformations of general relativity are extended to include SUSY transformations. The resulting model is called SuperGravity (SUGRA) [62], and contains the spin-2 graviton and its spin- $\frac{3}{2}$ partner, the gravitino (\tilde{G}). Generally, if the vacuum state is not SUSY invariant, a massless “Goldstone fermion”, or “Goldstino”, appears. In SUGRA, a “Super-Higgs”

effect [63] occurs, and the Goldstino becomes associated with the longitudinal degrees of freedom of the gravitino. The gravitino thus obtains a mass,

$$m_{3/2} = \frac{F_0}{\sqrt{3}M_P}, \quad (3.5)$$

where F_0 is a v.e.v. with dimension mass-squared. In models where SUSY invariance is lost at a low scale, *i.e.* $\sqrt{F_0} \ll M_P$, the gravitino is typically the LSP.

3.2.2 Gauge Mediated Supersymmetry Breaking

In GMSB models [64], the consequence of a vacuum state that is not SUSY invariant is transmitted to the MSSM by gauge interactions. A schematic depiction of a prototype model is depicted in Figure 3.3. The loss of SUSY invariance occurs in a “hidden sector” containing the goldstino. A “messenger sector” is coupled to the hidden sector through a $U(1)_m$ gauge force, and contains chiral superfields X , Φ_i , and $\bar{\Phi}_i$. The field X overlaps with the Goldstino and obtains v.e.v.’s M_{mes} and F in its scalar and auxiliary components, respectively. There may be several flavors of messenger fields, Φ_i and $\bar{\Phi}_i$, indexed by i , and each transform under the same representation of a GUT group that contains the SM gauge group. For the phenomenology presented here, an index N_{mes} specifies the characteristics of the messenger superfields. The couplings of X with Φ_i and $\bar{\Phi}_i$ generate messenger masses of order M_{mes} , and positivity of the messenger masses implies $F < M_{mes}^2$.

As the messenger fields are coupled to the MSSM by SM gauge interactions, mass



Figure 3.3: Schematic depiction of the three sectors in a prototype GMSB model. The loss of SUSY invariance occurs in the hidden sector (left). A messenger sector (middle) couples to both the hidden sector and the visible sector (right). See the text for further details.

terms for the SUSY partners of SM particles are generated radiatively [65]. Representative diagrams giving rise to these mass terms are illustrated in Figure 3.4. The gaugino masses are generated at one loop, and the sfermion masses at two loops. Complete formulae for the masses are given in References [66; 67]. Qualitatively, for a superpartner carrying a SM gauge quantum number a , the generated mass is a gauge loop factor smaller than the effective SUSY breaking scale in the visible sector, Λ ,

$$\tilde{m}_a \approx \frac{\alpha_a}{4\pi} \Lambda \quad , \quad \Lambda \equiv \frac{F}{M_{mes}}. \quad (3.6)$$

Thus, for supermasses at the electroweak scale, the value of Λ is $\mathcal{O}(100 \text{ TeV})$. Additionally, as the gaugino masses arise from one loop, these masses are proportional to N_{mes} , whereas the sfermion masses are proportional to $\sqrt{N_{mes}}$. Lastly, once Λ is set, the masses depend only logarithmically on M_{mes} .

The mechanism of communicating the loss of SUSY invariance by SM gauge interactions, and in particular the universality of gauge interactions with respect to the three fermion generations, results in a significant reduction of the number of free parameters, from over a hundred to just five in the minimal GMSB model,

$$\{\Lambda, M_{mes}, N_{mes}, \tan \beta, \text{sgn}(\mu)\}. \quad (3.7)$$

The sensitivity to the GMSB model is evaluated in this analysis using a benchmark set of constraints on these parameters called SPS8 [68], in which Λ is free and the other parameters

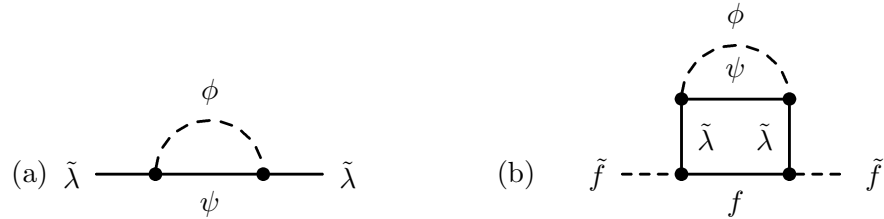


Figure 3.4: Example diagrams resulting in mass terms for MSSM particles in GMSB models. Gaugino masses ($\tilde{\lambda}$) arise at one loop (a) through interactions with messenger fields, depicted here by the fermionic component, ψ , and scalar component, ϕ , of a superfield Φ . Sfermion masses (\tilde{f}) arise at two loops (b).

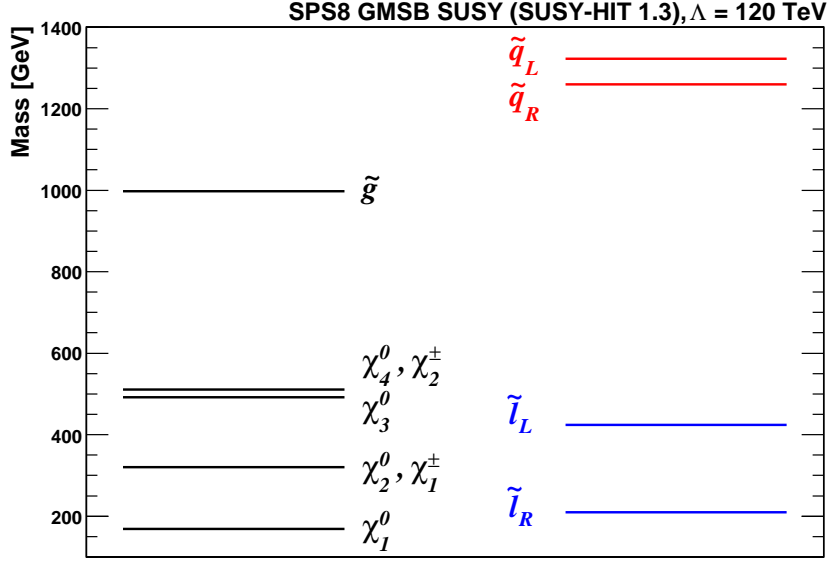


Figure 3.5: The spectrum of MSSM superpartner masses as determined by the GMSB SPS8 relations, evaluated with $\Lambda = 120$ TeV. The charginos, neutralinos, and gluinos are on the left, and sfermions on the right.

take the following values:

$$\{\Lambda, M_{mes} = 2\Lambda, N_{mes} = 1, \tan\beta = 15, \text{sgn}(\mu) > 0\}. \quad (3.8)$$

A set of SUSY particle masses, computed for SPS8 using SUSPECT v2.41 [67], as implemented in SUSY-HIT v1.3 [69], is shown for $\Lambda = 120$ TeV in Figure 3.5. For $N_{mes} = 1$, the lightest neutralino ($\tilde{\chi}_1^0$) is the next-to-lightest SUSY particle (NLSP), while values $N_{mes} > 1$ typically yield the light stau ($\tilde{\tau}_1$, the lighter mass eigenstate after mixing) as the NLSP. As the gravitino does not participate in SM gauge interactions, its mass is determined by Equation 3.5. If $F = F_0$ in Equation 3.5, and $F = \Lambda M_{mes} = 2\Lambda^2$ for SPS8, the gravitino mass is in the eV range for superpartner masses at the electroweak scale, and the gravitino is therefore the LSP.

With the masses of the superpartners defined by the GMSB model, the production of SUSY particles in $p\bar{p}$ collisions at $\sqrt{s} = 1.96$ TeV is now considered [70]. The primary process is the electroweak production of chargino and neutralino pairs, as depicted in Fig-

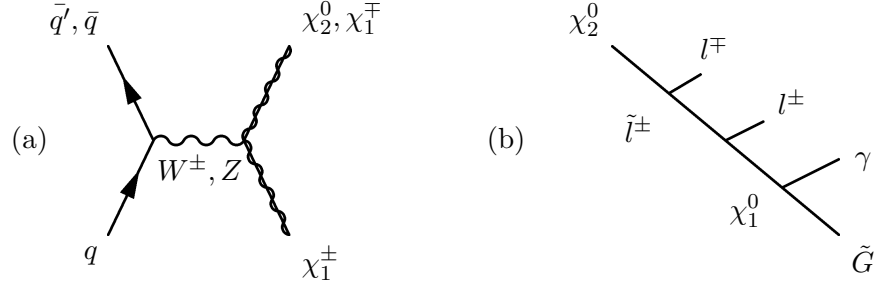


Figure 3.6: (a) Representative Feynman diagram for the electroweak production of chargino and neutralinos pairs at the Tevatron. (b) Representative decay chain depicting the cascade decay of the second neutralino (χ_2^0) to the NLSP (χ_1^0), which decays promptly via $\chi_1^0 \rightarrow \gamma\tilde{G}$.

ure 3.6(a). The next most significant production process is the electroweak production of pairs of sleptons ($\tilde{e}_R^+ \tilde{e}_R^-, \tilde{\mu}_R^+ \tilde{\mu}_R^-, \tilde{\tau}_1^+ \tilde{\tau}_1^-$). As the GMSB mass spectrum predicts heavy squarks and gluinos, they are not appreciably produced. Figure 3.7 gives the GMSB SUSY cross section, computed at next-to-leading order (NLO) using PROSPINO 2.1 [70], as a function of the scale Λ .

The two produced SUSY particles initiate decay chains involving lighter SUSY particles. An example cascade decay chain is shown in Figure 3.6(b). The major phenomenological feature of GMSB models is the gravitino as the LSP. In each SUSY event the decay chains yield two gravitinos that escape detection, resulting in missing transverse energy. The nature of the NLSP determines the other particles that define the final state. For the SPS8 criteria, and more generally $N_{mes} = 1$, the NLSP is the lightest neutralino with dominant decay mode $\chi_1^0 \rightarrow \gamma\tilde{G}$ [71]. The resulting final state is $\gamma\gamma + \cancel{E}_T + X$, where X denotes additional jets and leptons that may be produced in the decay chains. Searches for GMSB SUSY, and other BSM signatures in $\gamma\gamma + \cancel{E}_T + X$ events, have been performed at the CERN e^+e^- Collider (LEP) [72], and at the Tevatron in Run I [73] and Run II [12; 74]. Figure 3.7 shows the most recently published cross section limits on the GMSB model reported by the D0 [12] and CDF [74] collaborations.

When discussing the value of the gravitino mass for model parameters yielding superpartner masses at the electroweak scale, $F = F_0$ was assumed. The gravitino mass is

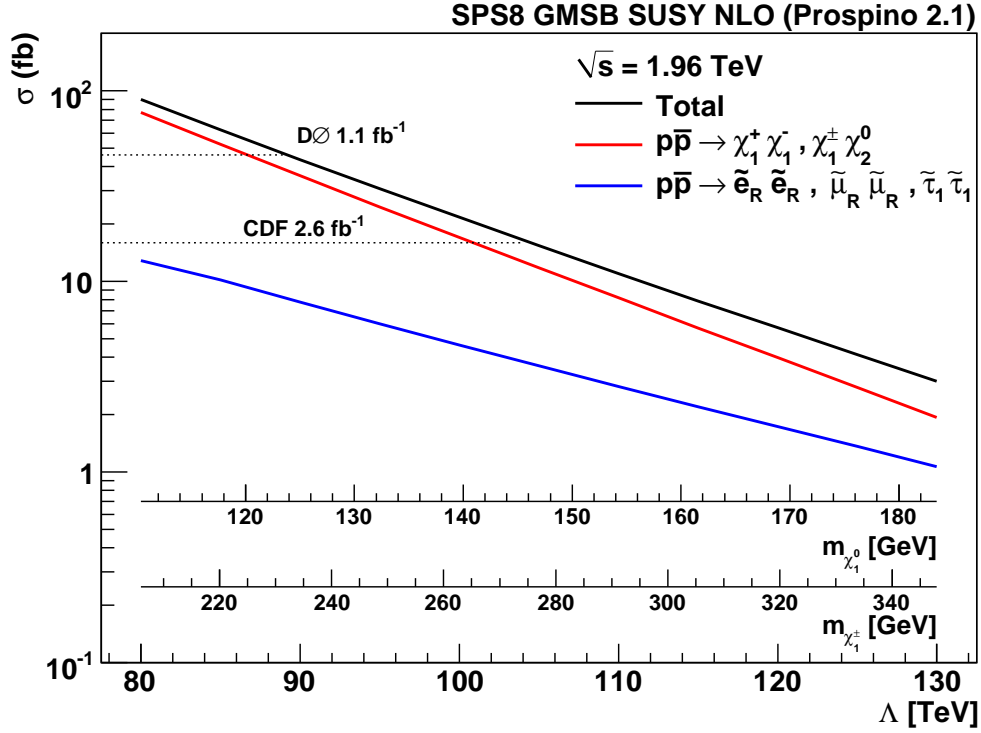


Figure 3.7: Total NLO production cross section for GMSB SUSY processes in $p\bar{p}$ collisions at $\sqrt{s} = 1.96$ TeV, and main subprocess cross sections, as a function of the scale Λ . Cross section limits [12; 74] on the SPS8 model which precede this analysis are shown. Corresponding masses for the lightest neutralino (χ_1^0) and chargino (χ_1^\pm) are also displayed.

determined by the sum of all v.e.v.'s, defined as F_0 . The field X that is responsible for the generation of messenger masses may not overlap completely with the Goldstino, and hence its associated v.e.v. is $F < F_0$. The decay width of the lightest neutralino depends on the coupling to the gravitino, via the Goldstino, and is given by [75]

$$\Gamma(\chi_1^0 \rightarrow \gamma\tilde{G}) = \zeta \frac{m_{\chi_1^0}^5}{16\pi F_0^2}, \quad (3.9)$$

where ζ is a factor typically of order unity that depends on gaugino and Higgsino mixing. Defining $\kappa > 1$ such that $F_0 = \kappa F$, the χ_1^0 decay length in terms of F is

$$c\tau(\chi_1^0 \rightarrow \gamma\tilde{G}) \approx \kappa^2 \left(\frac{100 \mu\text{m}}{\zeta} \right) \left(\frac{100 \text{ GeV}}{m_{\chi_1^0}} \right)^5 \left(\frac{\sqrt{F}}{100 \text{ TeV}} \right)^4. \quad (3.10)$$

Thus, if the overlap between X and the Goldstino is small, κ will be large, and the decay may occur over macroscopic distances, perhaps even outside the detector. Although this situation presents interesting phenomenological consequences [75], in this analysis the decay $\chi_1^0 \rightarrow \gamma \tilde{G}$ is assumed to occur promptly, *i.e.*, $c\tau < 1$ cm.

3.3 Extra Dimensions

Following the realization that the dual resonance model may form the basis of a unified theory that includes quantum gravity and compact extra dimensions, string theory developed with the assumption that the natural size of these compact dimensions is set by the Planck scale. However, developments during the second superstring revolution in the mid 1990s demonstrated that the string scale is not irrevocably tied to the Planck scale [76] and the extra dimensions could be substantially larger.

3.3.1 General Features of Models with Extra Dimensions

Several phenomenological models with extra dimensions have been proposed that are based on ideas and constructions which emerged in the investigation of string theories. The models generally differ according to:

- the number of extra dimensions considered,
- which fields are able to propagate in the extra dimension(s),
- the method of compactification (*i.e.* boundary conditions),
- whether the metric of the extra dimension(s) is flat or warped.

Some models propose one or more flat extra dimensions accessible to gauge bosons only and reveal new mechanisms to achieve vacuum states that are not SUSY invariant [77] and unification of gauge coupling constants [78]. The scale of these new mechanisms is set by the inverse radius of the compact extra dimension(s), R_c^{-1} , which could be as low as the electroweak scale. Other models restrict the SM particles to a four dimensional subspace, but allow gravity to propagate in the full extra dimensional spacetime, which may be either

flat [79] or warped [80]. These models address the fine tuning problem by predicting that the value of M_P appears large as a consequence of higher dimensional geometric effects that “dilute” the true strength of the gravitational force.

The UED model [81] considered here allows *all* SM particles to propagate in a single flat extra dimension of $\sim \text{TeV}^{-1}$ size. Further, the familiar four dimensions and UED are postulated to form a subspace of an extended space with large extra dimensions of $\sim \text{eV}^{-1}$ size [79] that are accessible to gravity only. This scenario gives rise to the possibility of enhanced production of $\gamma\gamma + \cancel{E}_T$ events at colliders.

3.3.2 Universal Extra Dimensions

The UED model begins with the SM symmetries and field content extended to a spacetime with $4 + \delta$ dimensions. The δ extra dimensions are assumed to be compact and flat. The $\delta = 1$ case is exclusively considered in this analysis, and the compactification radius is estimated to be in the range $R_c \sim (400 - 800 \text{ GeV})^{-1}$ [81].

Equations of motion are derived from the $4 + 1$ dimensional Lagrangian. For example, consider a scalar field, ϕ . The equation of motion is

$$(\partial^\mu \partial_\mu - \partial^4 \partial_4) \phi = m_0^2 \phi, \quad (3.11)$$

where $\mu = (0, 1, 2, 3)$ and the fourth partial derivative is with respect to the 5th dimension, which is labeled by y . The mass m_0 is the “5-dimensional mass”. As the extra dimension is compact with radius R_c , ϕ can be expanded in Fourier (also called Kaluza-Klein, or KK) modes,

$$\phi(x, y) = \phi(x, y)^+ + \phi(x, y)^- \quad (3.12)$$

$$\phi(x, y)^+ = \frac{1}{\sqrt{\pi R_c}} \phi_0^+(x) + \frac{2}{\sqrt{\pi R_c}} \sum_{n=1}^{\infty} \phi_n^+(x) \cos\left(\frac{ny}{R_c}\right) \quad (3.13)$$

$$\phi(x, y)^- = \frac{2}{\sqrt{\pi R_c}} \sum_{n=1}^{\infty} \phi_n^-(x) \sin\left(\frac{ny}{R_c}\right). \quad (3.14)$$

The motivation for separating the even (+) and odd (−) terms under $y \rightarrow -y$ will be discussed momentarily. In this form, one can view a given mode indexed by n as an

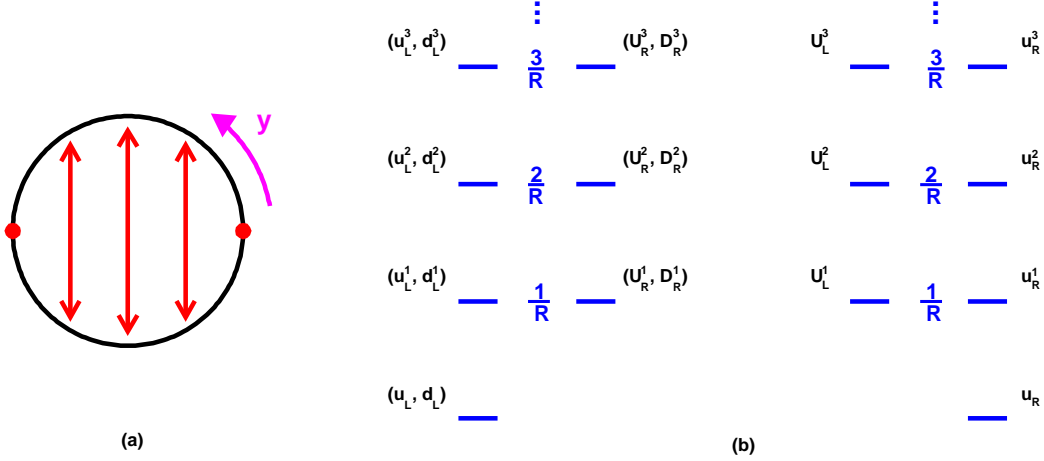


Figure 3.8: (a) Schematic depiction of S_1/Z_2 orbifold compactification for $\delta = 1$ UED. Opposite points on the circle are identified, $y \rightarrow -y$, with the fixed points shown as dots. (b) With this choice of compactification, KK reduction of 5D fermions yield the observed fermion content of the SM at the $n = 0$ level. See text for more details.

independent field in the four dimensional theory with mass,

$$m^2 = m_0^2 + \left(\frac{n}{R_c}\right)^2. \quad (3.15)$$

Instead of compactifying the 5th dimension on a circle, the UED model compactifies it on a S_1/Z_2 orbifold, which is a circle with opposite points identified, as depicted in Figure 3.8(a) [82]. Fields are therefore either even or odd under $y \rightarrow -y$, and the following assignments are made to reproduce the SM field content, *i.e.* the zero modes of the five-dimensional fields. Gauge bosons, A_M , $M = 0, 1, 2, 3, 4$, are defined such that the scalar components A_μ , $\mu = 0, 1, 2, 3$ are even fields and A_4 is odd, which ensures that the zero mode contains only the usual gauge field components. Similarly, as there is no chirality in five dimensions, there is a left-handed *and* right-handed KK mode for each SM chiral fermion. For example, the $SU(2)_L$ singlet chiral fermions, ψ_R^0 , are obtained from the decomposition

$$\psi(x, y)_R^\pm = \frac{1}{\sqrt{\pi R_c}} \psi_R^0(x) + \frac{2}{\sqrt{\pi R_c}} \sum_{n=1}^{\infty} \psi_R^n(x) \cos\left(\frac{ny}{R_c}\right) \quad (3.16)$$

$$\psi(x, y)_R^\mp = \frac{2}{\sqrt{\pi R_c}} \sum_{n=1}^{\infty} \psi_L^n(x) \sin\left(\frac{ny}{R_c}\right), \quad (3.17)$$

where the two KK fermions at a given $n > 0$ pair to give a Dirac fermion of mass $\frac{n}{R_c}$. Likewise, $SU(2)_L$ doublet chiral fermions, Ψ_L^0 , are obtained from the decomposition

$$\Psi(x, y)_L^+ = \frac{1}{\sqrt{\pi R_c}} \Psi_L^0(x) + \frac{2}{\sqrt{\pi L}} \sum_{n=1}^{\infty} \Psi_L^n(x) \cos\left(\frac{ny}{R_c}\right) \quad (3.18)$$

$$\Psi(x, y)_L^- = \frac{2}{\sqrt{\pi R_c}} \sum_{n=1}^{\infty} \Psi_R^n(x) \sin\left(\frac{ny}{R_c}\right), \quad (3.19)$$

where again the two KK fermions at a given $n > 0$ pair to form a Dirac fermion of mass $\frac{n}{R_c}$. Thus, the fermion content is doubled for modes with $n > 0$ and the chiral index (L or R) of a KK mode is understood as the index of the SM zero mode. Figure 3.8(b) depicts a tower of fermion KK modes, with $SU(2)_L$ doublets on the left and up-type singlets on the right. Finally, the geometry in Figure 3.8(a) is invariant under the interchange of the two fixed points. The associated symmetry is called KK-parity, a remnant of momentum conservation in the 5th dimension after orbifolding, and is a symmetry of the Lagrangian as long as the two fixed points are treated in a symmetric fashion. The consequences of KK-parity conservation are similar to R-parity in SUSY. For example, UED particles are only produced in pairs and must decay to another KK particle in the same mode.

For the collider phenomenology presented here, only first level ($n = 1$) KK modes are considered. At tree level, the first level KK particle masses are nearly degenerate, with masses $\approx R_c^{-1}$. Radiative corrections associated with compactification lift the degeneracies. These corrections have been computed [83] and implemented in PYTHIA 6.421 [84]. An example first level mass spectrum is shown in Figure 3.9 for $R_c = 480$ GeV using a cut-off value for radiative corrections $\tilde{\Lambda}$ such that $\tilde{\Lambda} R_c = 20$ [83]. Following the convention in PYTHIA, KK particles are labeled with (*).

At hadron colliders, the primary UED production processes are strong interaction pair production of KK quarks and gluons [85]. In $p\bar{p}$ collisions at $\sqrt{s} = 1.96$ TeV, pair production of KK quarks dominates. A representative Feynman diagram is given in Figure 3.10(a), and the leading order (LO) cross section as a function of R_c^{-1} is shown in Figure 3.11. The NLO UED production cross section has not yet been computed.

The spectrum shown in Figure 3.9 resembles a typical SUSY spectrum, although the UED spectrum is significantly more degenerate and the spins of the particles are, of course, different. UED signatures at colliders are generally very similar to those predicted by SUSY

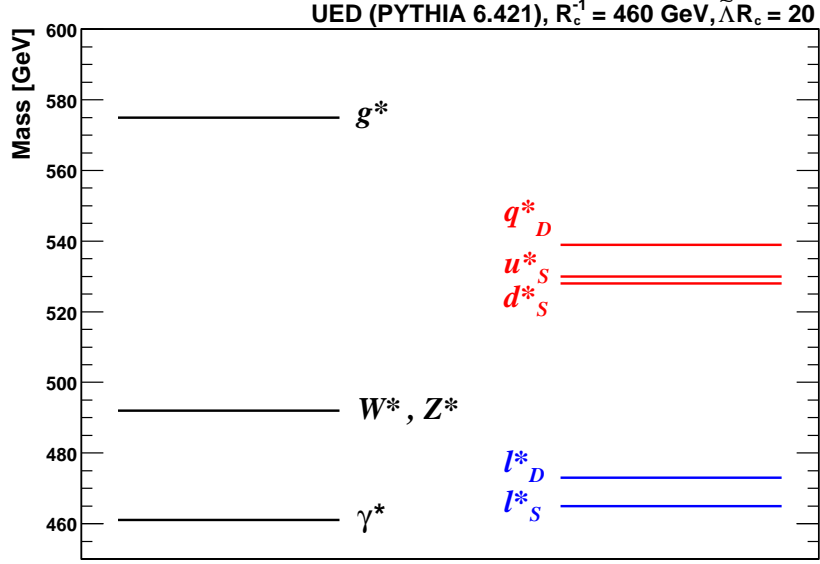


Figure 3.9: The spectrum of first level ($n = 1$) KK masses after radiative corrections, evaluated with $R_c^{-1} = 460$ GeV and $\Lambda R_c = 20$. The KK gauge bosons are on the left, and KK fermions on the right.

scenarios [86]. If KK parity is conserved, the produced KK quarks and gluons cascade decay to the lighter KK particles by emitting zero mode (*i.e.* SM) particles. The decays eventually terminate with two stable KK photons (γ^*), the lightest KK particle (LKP), and jets and leptons produced in the decay chains. The KK photons leave the detector without interacting, and the final state topology is $\cancel{E}_T + X$.

The scenario [87] investigated in this analysis considers KK-parity violation induced by gravitational interactions. If the conventional four dimensions and the UED comprise a subspace [88] of an extended spacetime that also contains large extra dimensions [79] accessible to gravity only, KK parity violating decays are induced [89]. In principle, all KK particles may decay to their corresponding zero mode and a graviton (G). The gravitational decay width of the KK modes are proportional to [90]

$$\Gamma \propto \frac{1}{M_D^{N+2}}, \quad (3.20)$$

where N is the number of large extra dimensions and M_D is the fundamental Planck

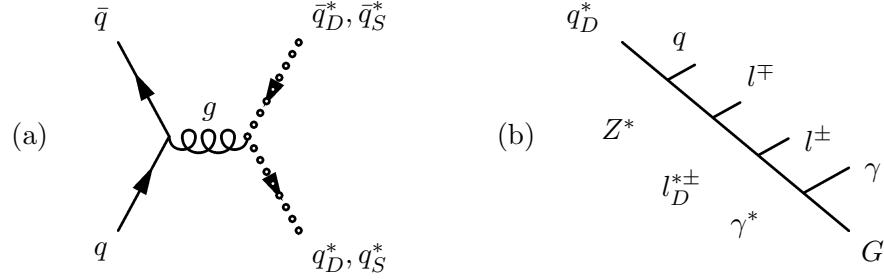


Figure 3.10: (a) Representative Feynman diagram for the strong production of KK quark pairs at the Tevatron. (b) Representative decay chain depicting the cascade decay of the $SU(2)$ doublet KK quark (q_D^*) to the LKP (γ^*), which decays promptly via $\gamma^* \rightarrow \gamma G$.

scale [79] defined such that,

$$M_P^2 = M_D^{2+N} R^N. \quad (3.21)$$

In the above equation, R represents the radius of the eV^{-1} size large extra dimensions. We consider the case where KK mass splitting decay widths are greater than the gravity mediated decay widths, which is achieved for larger N values. The values $N = 6$ and $M_D = 5$ TeV are chosen [87], and consequently the $n = 1$ KK modes decay primarily through KK mass splitting decay modes, except for the KK photon, with the only decay mode available being $\gamma^* \rightarrow \gamma G$. An example decay chain is shown in Figure 3.10(b). The graviton is effectively massive after the finely spaced KK spectrum is summed over, as in other large extra dimension scenarios [79]. The graviton escapes detection, and the resulting final state in this UED scenario with gravity mediated decays is therefore $\gamma\gamma + \cancel{E}_T + X$. This analysis presents the first limits on this UED scenario.

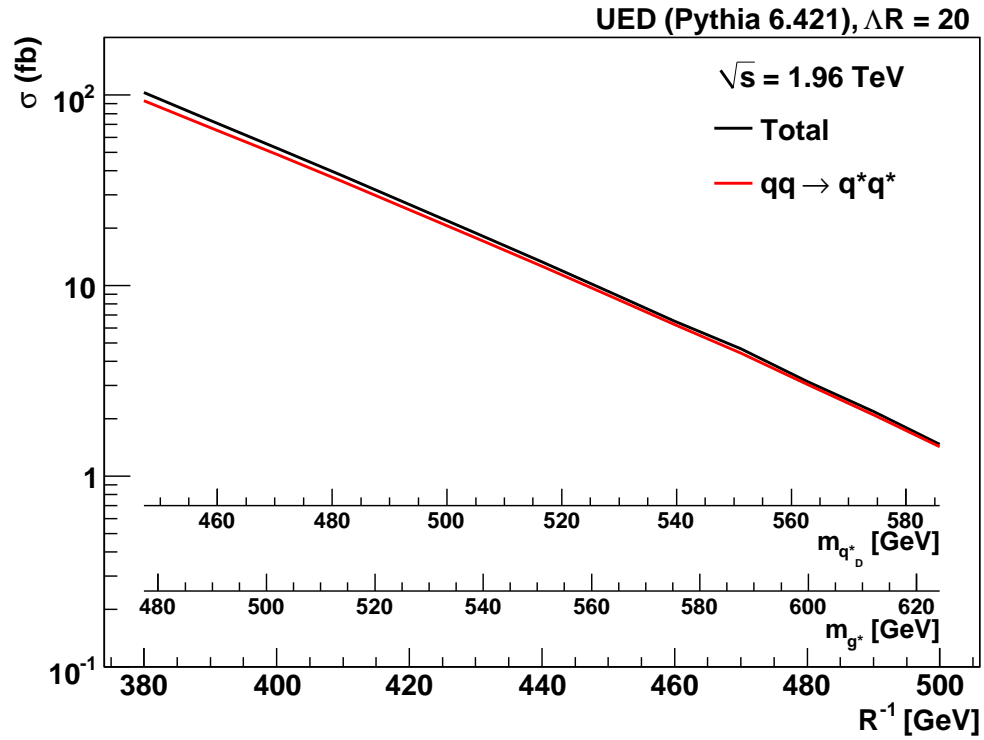


Figure 3.11: Total LO production cross section for UED processes in $p\bar{p}$ collisions at $\sqrt{s} = 1.96 \text{ TeV}$, and the KK quark pair production subprocess cross section, as a function of the scale R_c^{-1} . The corresponding masses for the KK quark (q_D^*) and KK gluon (g^*) are also shown.

Chapter 4

Experimental Apparatus

Fermilab National Accelerator Laboratory (Fermilab) [91], located in Batavia, Illinois, is a US Department of Energy laboratory specializing in high-energy particle physics. Fermilab operates the Tevatron Collider [92; 93], a machine that accelerates beams of protons and antiprotons. The beams intersect and produce $p\bar{p}$ collisions with a center-of-mass energy of 1.96 TeV. Two general purpose detectors located at opposite sides of the accelerator, D0 and CDF, record the properties of the particles that are created in these collisions. After a brief summary of the stages of the Tevatron Accelerator complex, this chapter describes the components of the D0 detector [94; 95; 96].

4.1 The Tevatron at Fermilab

The Tevatron provides the last and greatest acceleration phase in a series of accelerators at Fermilab. A schematic depiction of the accelerator complex is shown in Figure 4.1. The Cockcroft-Walton generator, Linear accelerator, and Booster constitute the Proton Source. The Debuncher and Accumulator form the Antiproton Source. Two large accelerators, the Main Injector and Tevatron, complete the chain.

The Proton Source begins with a Cockcroft-Walton generator which creates negatively ionized hydrogen gas. The hydrogen ions have an energy of 750 KeV and are then accelerated through a 150 m radio frequency (RF) linear accelerator (LINAC), reaching an energy of 400 MeV before passing through a carbon foil. The foil strips the two electrons from the

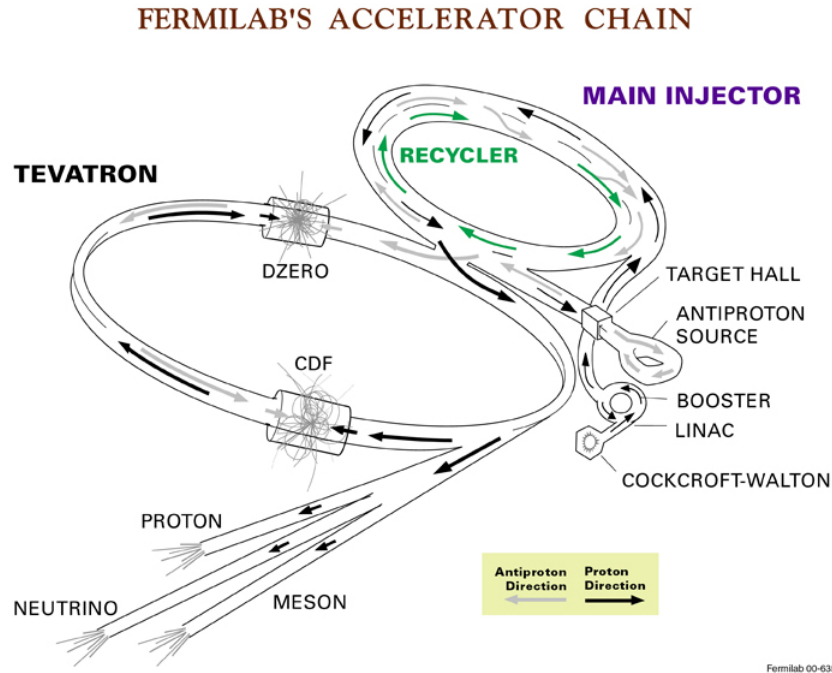


Figure 4.1: A schematic depiction of the Tevatron Accelerator Complex.

ions, thereby creating a proton beam that is injected into the Booster. The Booster is a circular synchrotron, 75 m in radius, with RF cavities that accelerate the protons to 8 GeV and magnets that maintain the circular trajectory.

The Main Injector (MI) is the smaller of the two large accelerators at Fermilab, with a radius approximately seven times larger than the Booster. The MI receives protons from the Booster and accelerates them to 150 GeV before injection into the Tevatron. Additionally, the MI plays an important role in the creation of the antiproton beam. The MI delivers 120 GeV protons to a nickel target in the Antiproton Source area, creating a cascade of hadrons. A spectrometer selects antiprotons with energy approximately 8 GeV from the collision remnants. The role of the Debuncher is to reduce the momentum spread and emittance of the captured antiprotons before transferring them to the Accumulator. After many transfers, the Accumulator delivers a stack of antiprotons to the Recycler, which is located in the same ring as the MI. The Recycler holds antiprotons from the Accumulator and remaining antiprotons from a Tevatron store. The MI accepts antiprotons from the

Recycler and accelerates them to 150 GeV before injecting them into the Tevatron.

A total of 36 bunches per beam, each consisting of more than 10^{10} protons or antiprotons, are injected in opposite directions into the Tevatron, which accelerates both beams to 980 GeV. Superconducting dipole magnets maintain the circular trajectory and superconducting quadrupoles focus the beams. The superconducting cryogenic system significantly reduces the power consumption of the magnets. The Tevatron is 1 km in radius and collides proton and antiproton bunches at the two high luminosity interaction regions inside the D0 and CDF detectors every 396 ns with a center of mass energy of 1.96 TeV.

Instantaneous luminosity, \mathcal{L} , is a measure of the collision rate per unit area per unit time, and is expressed as,

$$\mathcal{L} = fn \frac{N_1 \cdot N_2}{A}, \quad (4.1)$$

where f is the revolution frequency of the accelerator ($f = 47713$ Hz for the Tevatron), n is the number of bunches in a beam, N_1 and N_2 are the number of particles in each beam bunch, and A is the cross sectional area of the beams. The Tevatron has achieved peak luminosities over $4 \times 10^{32} \text{ cm}^{-2} \text{ s}^{-1}$. The integrated luminosity, *i.e.* the instantaneous luminosity integrated over time, is often expressed in terms of fb^{-1} , where $1 \text{ fb}^{-1} = 10^{39} \text{ cm}^{-2}$. The present analysis uses a dataset corresponding to 6.3 fb^{-1} .

4.2 The D0 Detector

The D0 detector [94; 95; 96] is a general purpose instrument designed to study a wide variety of SM processes and to perform searches for new phenomena predicted in BSM scenarios. Figure 4.2 shows a schematic cross sectional view of the detector, highlighting several detector subsystems and the physical scale of the device. The three major detector subsystems are the tracking detectors located close to the interaction region, the calorimeters, and the muon system. After introducing the D0 coordinate system and related definitions, the key features and functions of each subdetector system are described.

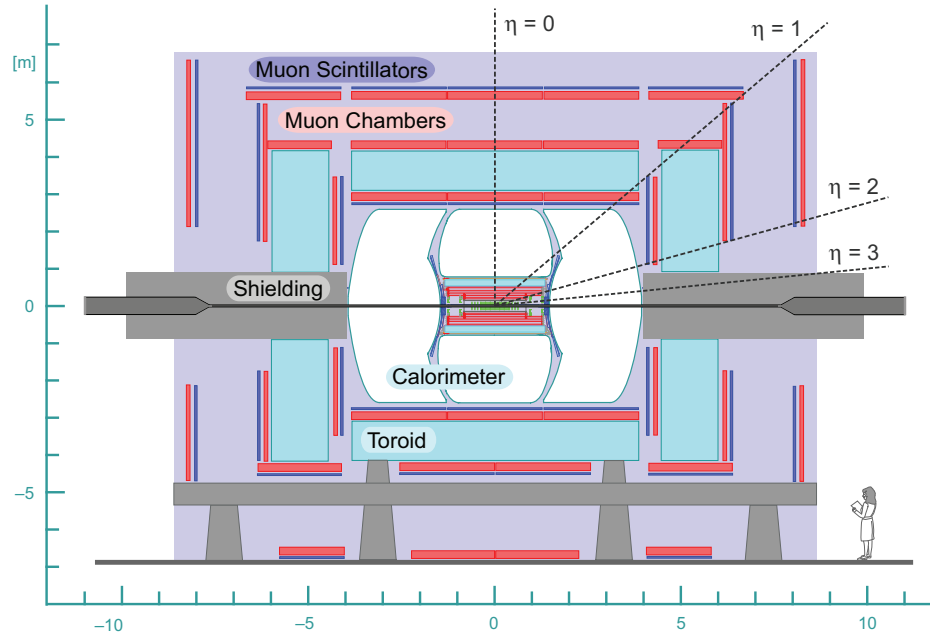


Figure 4.2: Side view depiction of the D0 detector. Several subsystems are labeled. The tracking detectors are not labeled and are the innermost elements, located within the calorimeter cryostats.

4.2.1 Coordinate System

The coordinate system used by D0 is shown in Figure 4.3. The positive z -axis is in the direction of the proton beam, and the x -axis points radially outward from the center of the Tevatron. The cartesian coordinate system is oriented in the right-handed convention, with the y -axis pointing in the vertically upward direction. The radial coordinate r is defined as $r = \sqrt{x^2 + y^2}$. The azimuthal angle, $\phi \in [0, 2\pi]$, is measured with respect to the x -axis in the x - y plane. The polar angle, $\theta \in [0, \pi]$, is measured with respect to the z -axis in the z - y plane.

The *pseudorapidity* of a particle, η , is defined as

$$\eta = \frac{1}{2} \ln \frac{|\vec{p}| + p_L}{|\vec{p}| - p_L} = -\ln \tan \left(\frac{\theta}{2} \right), \quad (4.2)$$

where $|\vec{p}|$ is the total momentum, and p_L is the momentum component along the z -axis. Pseudorapidity is commonly used in place of θ to specify the trajectory of a particle, and

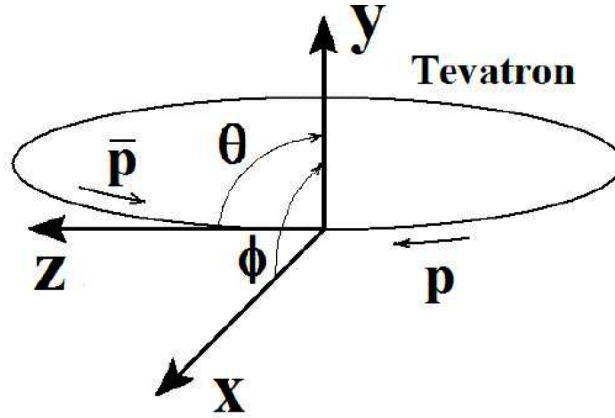


Figure 4.3: Schematic of the coordinate system adopted by D0.

is equivalent in the limit of zero particle mass to *rapidity*, y , defined as,

$$y = \frac{1}{2} \ln \frac{E + p_L}{E - p_L}, \quad (4.3)$$

where E is the particle energy. The difference in the rapidity of two particles is independent of Lorentz boosts along the beam axis.

The variable ΔR is commonly used to represent physical separation, *e.g.* between two particles, and is defined as

$$\Delta R = \sqrt{\Delta\phi^2 + \Delta\eta^2}, \quad (4.4)$$

where $\Delta\phi$ and $\Delta\eta$ represent the corresponding differences between the particles in ϕ and η . Other frequently used definitions are *transverse energy* and *transverse momentum* with respect to the beamline, defined as $E_T = E \sin \theta$ and $p_T = p \sin \theta$, respectively.

When the above coordinates and variables are evaluated with respect to the center of the detector, *i.e.* the detector origin $(0,0,0)$, they are referred to as *detector coordinates*, often denoted by a subscript *det*. This coordinate system may not coincide with the *physics coordinates* of an event, as $p\bar{p}$ collisions take place with $\sigma_z \sim 25$ cm about the detector origin. Physics quantities, such as E_T and \cancel{E}_T , are evaluated in the physics coordinate system, the definition of which depends on the location of the identified large momentum transfer $p\bar{p}$ collision vertex (PV) in the event.

4.2.2 Tracking Detectors

The tracking system of the D0 detector is designed to identify charged particle trajectories over a wide range of η values, and to perform precise track momentum and vertex measurements. The system consists of two subdetectors, the silicon microstrip tracker (SMT) [97; 98] and central fiber tracker (CFT) [99]. Both trackers are located within a 2 T superconducting solenoid magnet, as shown in Figure 4.4, which bends the trajectories of charged particles, allowing a determination of the momenta of the particles.

The SMT is the element closest to the beam pipe and utilizes doped silicon semiconductor technology. When a charged particle passes through one of the microstrip sensors of the SMT, ionizing radiation creates electrons and holes in the semiconductor which move toward electrodes under the influence of an applied electric field. The sensors are ≈ 10 cm in length with ≈ 50 μm pitch. The pulse of charge is collected and read out with spe-

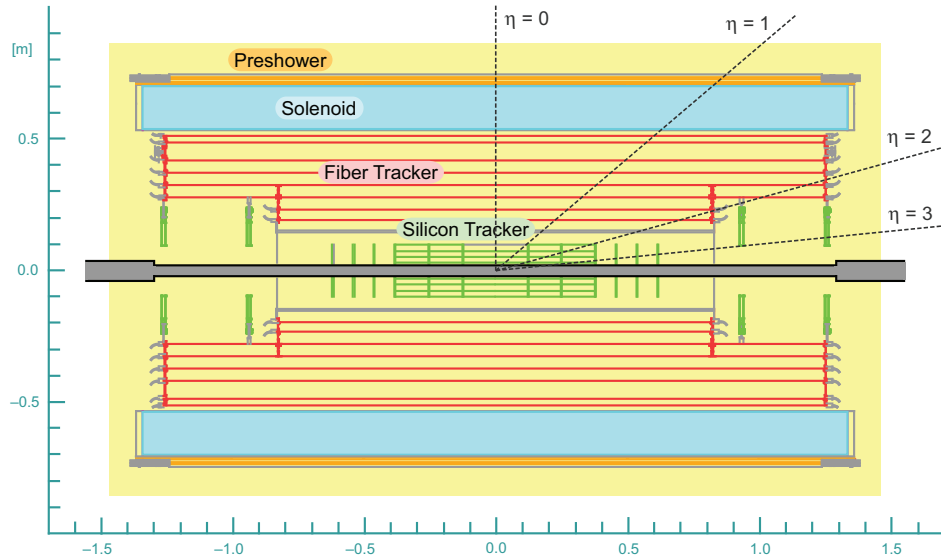


Figure 4.4: The D0 tracking system is located within a superconducting solenoid magnet. The silicon tracker (SMT) is the closest element to the beam pipe, and the fiber tracker (CFT) surrounds the SMT. The central preshower (CPS) detector is located just outside the solenoid cryostat.

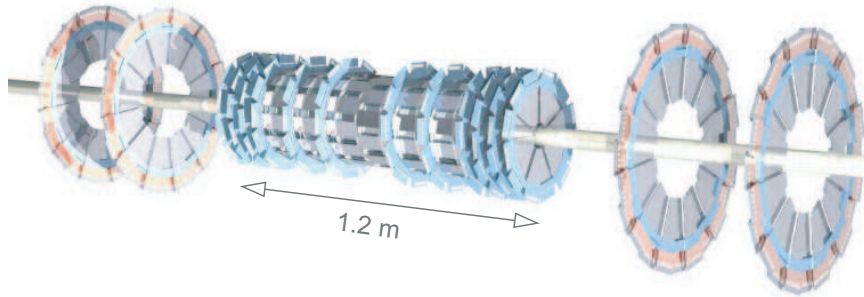


Figure 4.5: Detailed view of the SMT detector. The barrel modules are shown in the center with the different layers aligned horizontal to the beam pipe. The F-disks are seen interleaved with the barrels, oriented vertically. The large H-disks are seen oriented vertically at each end away from the barrel modules.

cialized electronics that amplify, digitize, and store the signal. The temperature of the semiconducting elements is maintained below 5°C to minimize radiation damage to the silicon.

A detailed view of the SMT detector is shown in Figure 4.5. The layout of the sensor modules is optimized to allow for good measurements of both low and high η tracks over a wide interaction region. This is achieved with a combination of barrel modules with microstrip sensors oriented horizontally along the beam pipe, and disk modules with sensors oriented vertically at fixed z -values. The barrel region is divided into six segments, with each consisting of six module layers. Barrel modules primarily measure the $r - \phi$ coordinate. An “F-disk” is located at the end of each barrel segment and consists of twelve double-sided wedge modules. Three additional F-disks are mounted at the end of each side of the barrel region, for a total of twelve. In the forward region (large $|\eta|$), two “H-disks” are placed on each side, each consisting of two sides of twelve modules. The disk modules measure $r - z$ and $r - \phi$ coordinates. With the H-disks, the SMT provides track measurements up to $|\eta| < 3$, and the typical track hit position resolution is $10\ \mu\text{m}$.

The CFT consists of scintillating fibers, $\approx 800\ \mu\text{m}$ in diameter, mounted on eight concentric support cylinders about the SMT and beam pipe, as shown in Figure 4.4. Each of the eight cylinders contains an axial (parallel to the beam pipe) and stereo (3° pitch relative

to axial) doublet layer of fibers. Light production in the fibers is a multistep process. A charged particle passing through a fiber excites a fluorescent dye that emits light, but at a frequency that is not well transmitted in the fiber. A second wavelength shifting dye in the fiber absorbs and reemits the light at a well-transmitted frequency. The non-readout end of the fiber is mirrored and the light is collected at the other end of the detector with similar clear fibers. Waveguides collect the light from the fibers and transmit it to visible light photon counters (VLPCs) located below the detector that convert the light signal into an electrical signal. Precision tracking requires small diameter fibers of low material density. Additionally, relativistic particles deposit energy near minimum ionization. These facts necessarily imply a low light output and the need for single photon detection capability. The VLPCs are kept at 9 K and achieve low noise and high quantum efficiency.

The SMT and CFT are surrounded by a thin superconducting solenoid magnet operating with a current of ≈ 5 kA and producing a uniform 2 T magnetic field parallel to the beam pipe. The magnet is enclosed in a cryostat which is approximately 0.9 radiation lengths (X_0) thick at $\eta = 0$.

4.2.3 Preshower Detectors

The D0 detector is instrumented with a central preshower (CPS) detector [100] and a forward preshower (FPS) detector [101]. The preshower detectors perform energy measurements and, as a result of their fine segmentation, allow precise measurements of shower position as well. CPS detector information is used in this analysis to enhance the association of tracks and vertices with electromagnetic (EM) calorimeter clusters, and to provide additional variables used to discriminate real EM clusters from fakes due to misidentified jets.

The CPS detector services the region $|\eta| < 1.3$ and utilizes triangular strips of scintillating material which is similar to that employed in the CFT. The detector consists of three concentric layers of strips located just outside of the solenoid and in front of the central calorimeter cryostat, as shown in Figure 4.4. The dimensions of each strip are shown in Figure 4.6(a), and the nesting of the strips in a given layer is shown in Figure 4.6(b). Each strip is wrapped in aluminized mylar for optical isolation, and the ends are painted white

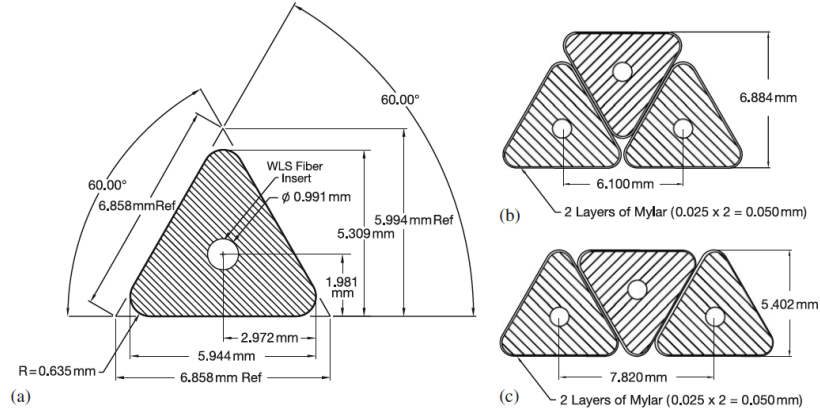


Figure 4.6: (a) The cross sectional dimensions of a triangular scintillating strip used in the D0 preshower detectors. The packing geometry in a given layer of the CPS (b) and FPS (c).

to enhance reflectivity. Each layer has 1280 strips, and each strip is split at $z = 0$ and read out from both ends of the detector. Embedded within each strip is a wavelength shifting fiber that collects the light and carries it to the end of the detector. The non-readout ends of the fibers are diamond polished and silvered. At the readout end, the fibers are grouped to connectors, and then to waveguides and VLPCs. The latter two elements and associated electronics are the same as those used for the CFT. One of the three layers is oriented axially with the strips parallel to the beampipe, while the other two are pitched with stereo angles $\pm 24^\circ$. Charged particles typically deposit energy in multiple strips and layers, allowing for an offline computation of an associated CPS cluster in the ϕ and z coordinates.

The FPS detector utilizes similar components and is mounted on each of the two endcap calorimeter cryostats. The FPS strips are packed as shown in Figure 4.6(c). The FPS detector is not used in this analysis.

4.2.4 Calorimeters

Calorimeters provide energy and incident position measurements for electrons, photons, and jets, and play a significant role in the identification of electrons, photons, jets, and the calculation of \cancel{E}_T . A cutaway depiction of the D0 calorimeter system [94] is shown in

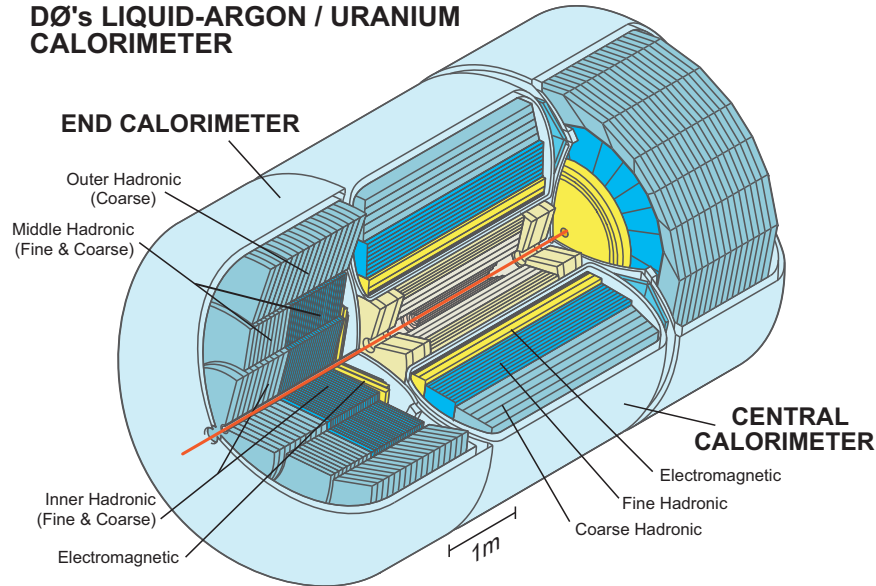


Figure 4.7: A cutaway view of the D0 calorimeter system showing the central and endcap calorimeters. The different regions of longitudinal segmentation, *e.g.* the EM, FH, CH layers, are also labeled.

Figure 4.7. The calorimeters utilize liquid argon (LAr) and uranium sampling technology, and are divided into three units. Each unit is contained within a cryostat that maintains the detector below 90 K. The central calorimeter (CC) covers $|\eta| < 1.1$, and two endcap calorimeters (EC) cover the regions $1.3 < |\eta| < 4.0$. The calorimeters are segmented in both the longitudinal and transverse directions. Longitudinal layers closest to the beam pipe comprise the electromagnetic (EM) sections, and the outer layers comprise the hadronic (HAD) sections. The HAD section is divided into the fine hadronic (FH) layers and the outermost coarse hadronic (CH) layers.

The different calorimeter layers contain both absorber and active material. The absorber material in the EM layers is plates of depleted uranium, while uranium-niobium alloy is used in the FH layers, copper in the CH layer of the CC, and stainless steel in the CH layer of the EC. The active material is LAr in all layers. EM showers are initiated by incident particles, such as electrons and photons, that produce bremsstrahlung and electron-positron pairs as they pass through the absorber plates. HAD showers are initiated by hadrons that

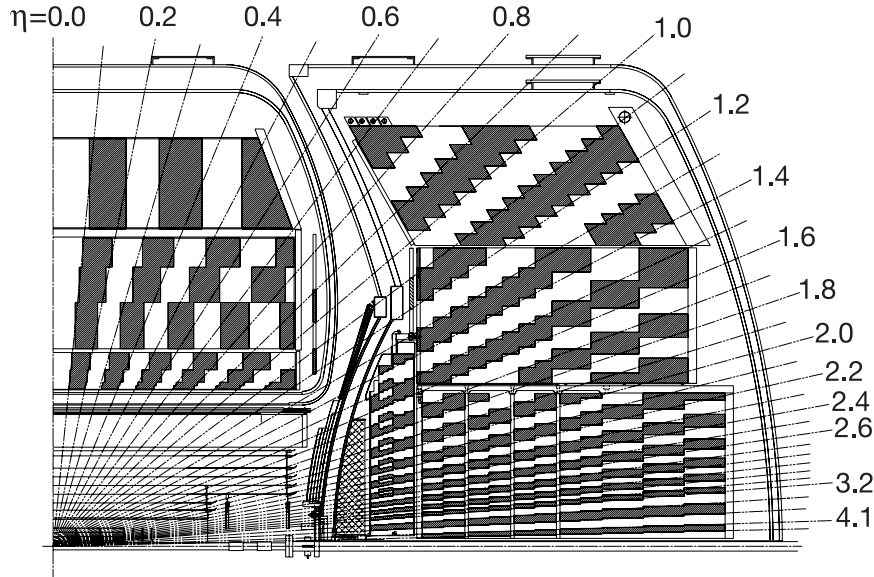


Figure 4.8: Cross sectional view of the D0 calorimeters showing the projective towers in the CC and EC and the segmentation of the detector.

interact strongly with the absorber nuclei, though HAD showers also typically have a considerable EM component as well. EM and HAD showers ionize the LAr medium, and the charge is drifted by an applied electric field to plates held at high voltage. The potential difference between the plates creates an ionization pulse which is analyzed with electronics and constitutes the calorimeter signal.

A detailed cross sectional view of the calorimeters is shown in Figure 4.8. In the CC, the EM section is segmented in four longitudinal layers, the FH section in three, and the CH in one. The EC contains the EM layers, and inner, middle, and outer HAD layers. The calorimeters are transversely segmented to form pseudoprojective towers with respect to the detector origin. The transverse segmentation is approximately 0.1×0.1 in $\Delta\eta \times \Delta\phi$. As the nominal depth of the maximum development of an EM shower occurs at the third EM layer, this layer is more finely segmented, 0.05×0.05 , in order to improve particle identification capability. The longitudinal and transverse segmentation creates more than 50k readout channels. Table 4.1 summarizes several properties of the calorimeters.

| | EM | FH | CH |
|-------------------------------------|---------|-----------------|----------------------|
| Layers | 4 | 3 | 1 |
| Absorber | Uranium | Uranium-niobium | Copper (CC) |
| Material | | | Stainless Steel (EC) |
| Radiation Lengths (X_0) | 20.5 | 96.0 | 32.9 |
| Interaction Lengths (λ_A) | 0.8 | 3.2 | 3.2 |

Table 4.1: Several properties of the D0 calorimeters.

Figure 4.9 depicts the calorimeter signal processing chain. The beam crossing period is 396 ns and the characteristic drift time of electrons across the LAr gap is approximately 450 ns. The role of the electronics is to sample and store the ionization signal at the beam crossing rate, and subtract residual signal from the previous bunch crossing. From the cell pads where the charge is collected, the ionization signal propagates to electronics beneath the detector. The readout electronics amplify, shape, split the signal according to two gain paths, and store the sampled signal in an analog switch capacitor array (SCA). Stored events for offline analysis events are selected by a dedicated trigger system, described momentarily. Upon a Level 1 trigger accept, the signal is extracted from the SCA, and

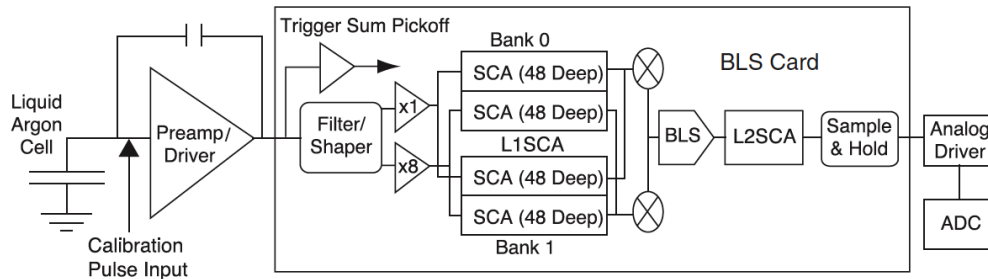


Figure 4.9: Schematic diagram of the signal processing electronics for the DO calorimeter.

a baseline subtraction (BLS) calculation is made to account for residual signal from the previous bunch crossing. Additionally, a gain choice appropriate to the analog to digital converter (ADC) dynamic range is made. The analog signal is then stored in a second SCA. Upon a Level 2 accept the signal is digitized and sent, along with the rest of the event information, to the Level 3 computers.

A calibration system [102] is used to inject charge into the electronics system to calibrate the gain and linearity of the response. Different channels may have different gain factors as a result of slight differences in the amplifier properties, and a small non-linear response may result from saturation effects in the ADC. Additionally, some channels are masked as a result of anomalous noise [103; 104] or dead SCA components within the signal processing electronics [105].

The calorimeters achieve the following fractional energy resolutions [94] for EM and HAD showers, respectively:

$$\frac{\sigma_E}{E} = \frac{15\%}{\sqrt{E \text{ (GeV)}}} \oplus 2\% \quad \text{EM} \quad (4.5)$$

$$\frac{\sigma_E}{E} = \frac{60\%}{\sqrt{E \text{ (GeV)}}} \oplus 5\% \quad \text{HAD}, \quad (4.6)$$

where \oplus denotes a quadrature sum. The predominant $\sigma_E \propto \sqrt{E}$ dependence reflects the stochastic nature of particle showers. The resolution for EM showers is better than for HAD showers, as a greater fraction of the incident energy is sampled in EM showers.

4.2.5 Intercryostat Detectors

The region $0.8 < |\eta| < 1.4$, referred to as the intercryostat region, is not entirely covered as a result of the separate CC and EC calorimeters. In addition, there is substantial unsampled material in this region that degrades the energy resolution. The region on each side of the detector has been instrumented with scintillating tiles to regain lost sensitivity. The combination of devices in the region is referred to as the Intercryostat Detector (ICD). The ICD increases the acceptance for some analyses, particularly those with electrons well matched to inner detector tracks and low backgrounds. The performance for photons is poor in this region, however, and the ICD is not used in this analysis.

4.2.6 Muon Spectrometer

The muon spectrometer is the detector element furthest away from the interaction region, and located outside the toroid magnets. The magnet system consists of three elements, the central toroid, which produces a 1.8 T field, and two forward toroids located at each end of the detector, which produce 1.9 T fields. The magnets curve the trajectory of muons, allowing for momentum measurements that are independent of those made by the inner detector.

As muons are minimum ionizing particles, they typically deposit only a small fraction of their energy in the calorimeter. The muon detectors therefore surround the calorimeter and toroid magnets. Different muon detector elements are used in different regions. The central detector, covering the $|\eta| < 1$ region, utilizes proportional drift tubes (PDTs). These are gaseous detectors, with the gas ionized by the passage of a muon and charge collected by high voltage wires. A similar technology, utilizing detectors called mini drift tubes (MDTs), is employed in the forward region, $1 < |\eta| < 2$. In addition to the gaseous detectors, layers of scintillators are employed. Roughly speaking, the scintillators are used to trigger and identify muons, while the gaseous detectors chambers are used for precise measurements of the trajectory.

Muons are reconstructed by combining hits in the muon system to form segments, which are then matched to reconstructed tracks in the inner detector. Muons are only used in this analysis in relation to the calculation of \cancel{E}_T . A handful of events in the selected $\gamma\gamma$ sample contain low to intermediate p_T muons, and the \cancel{E}_T is corrected in these events accordingly.

4.2.7 Luminosity Detector

Two luminosity monitor (LM) detectors are located ± 140 cm from the detector origin and cover the range $2.7 < |\eta| < 4.4$, as shown in Figure 4.10. Each LM is made of scintillating plastic wedges, and the scintillating light from each wedge is measured with a photo-multiplier tube. The time resolution of the LM is better than 3 ns, which allows coincident measurements between the two detectors and is useful to suppress beam halo hits.

The majority of $p\bar{p}$ collisions produce low p_T particles with small scattering angles. The

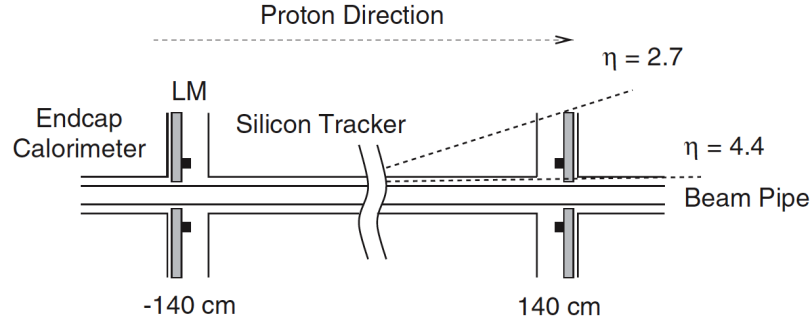


Figure 4.10: Schematic drawing of the location of the LM detectors.

luminosity is determined from the average number of inelastic collisions per beam crossing (\bar{N}_{LM}) measured by the LM. The number of crossings with and without hits follows a Poisson distribution and \bar{N}_{LM} can be determined using the fraction of beam crossings with no collisions. The instantaneous luminosity measured in a short interval of time, called a luminosity block, is determined by

$$\mathcal{L} = \frac{f_b \bar{N}_{LM}}{\sigma_{LM}}, \quad (4.7)$$

where $f_b = 1.7$ MHz is the bunch crossing frequency and σ_{LM} is the effective cross section, which accounts for both the acceptance and efficiency, observed by the LM [106].

4.2.8 Trigger and Data Acquisition System

The bunch crossing rate is 1.7 MHz, while the practical rate at which recorded events can be stored for detailed analysis is ≈ 100 Hz. The majority of $p\bar{p}$ collisions are low momentum transfer, so requirements are made to select, or “trigger”, events with interesting properties for more detailed consideration before choosing to record the event to tape. The D0 trigger system consists of three levels. The Level 1 (L1) system utilizes custom hardware and firmware closely integrated with the readout of the subdetectors. A $4.2 \mu\text{s}$ buffer holds the information from each bunch crossing, allowing the detector to operate continuously. After L1 trigger requirements the event rate is reduced to ≈ 2 kHz. Level 2 (L2) utilizes single board computers (SBCs) which parse information from each subdetector using dedicated

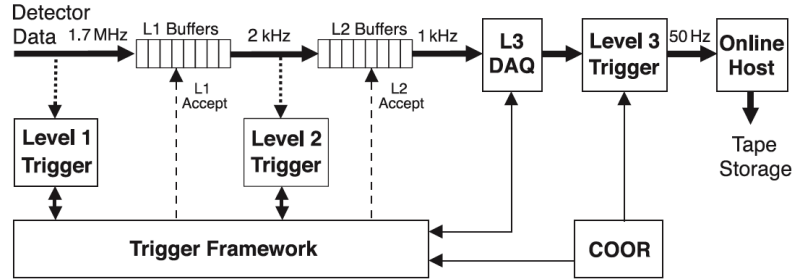


Figure 4.11: Flowchart of the D0 trigger and data acquisition system.

algorithms, reducing the event rate to ≈ 1 kHz. Lastly, Level 3 (L3) uses more sophisticated algorithms, similar to those performed on stored events in offline reconstruction, and is run on a farm of computers. Figure 4.11 shows a flowchart of the trigger and data acquisition system. The final rate of events stored to tape is ≈ 100 Hz.

A stored event must pass a logical AND of L1, L2, and L3 requirements. L1 triggers relevant in this analysis are calorimeter based triggers which search for energy depositions in towers that are above a predefined threshold. There are 1280 calorimeter towers at L1, each covering $\Delta\eta \times \Delta\phi = 0.2 \times 0.2$. The granularity is increased to 2560 towers at L2, and calorimeter based triggers at this level perform rough measurements to identify narrow EM showers that are isolated from HAD showers. Algorithms are run at L3 that analyze calibrated EM clusters for potential electrons and photons.

Chapter 5

Physics Object Reconstruction

Stored data in triggered events recorded by the D0 detector are reconstructed by certified algorithms in a common software architecture [107]. These algorithms assemble the data from each detector subsystem and create *physics objects*, such as tracks, track vertices, electromagnetic objects (*e.g.* electrons and photons), hadronic jets, muons, and missing transverse energy. Features of these algorithms are described in this chapter.

5.1 Particle Tracks

The transverse momentum of a charged particle traversing through the volume within the solenoid is given by $p_T = qB/\rho$, where q is the particle's charge, ρ is the radius of curvature of the trajectory, and B is the magnetic field produced by the solenoid. The trajectory is reconstructed from the measurements, or hits, recorded by the tracking detectors as the particle interacts with the detector elements. For the SMT, a hit represents charge collection in a microstrip, while for the CFT a hit represents light collected by a fiber. A charged particle typically creates hits in adjacent strips and fibers, and groups of nearby hits are combined by a process called track hit clustering.

Two algorithms are used by D0 to reconstruct the trajectory, or *track*, of a charged particle. The algorithms are seeded by clusters, and the tracks reconstructed by each algorithm are later combined into a common pool and recomputed using a Kalman filter [108] that accounts for ionization energy loss and multiple scattering. Optimal track parameters are

determined using predictive algorithms and a multi-dimensional χ^2 minimization.

The first track finding algorithm is called the *Histogram Track Finder* (HTF) [109]. This algorithm uses a mapping, called a Hough transformation, from the (x, y) coordinate of a hit to the (ρ, ϕ) coordinate space. The advantage of this transformation is that all hits along a trajectory between the origin and (x, y) map to a single point in the (ρ, ϕ) plane. Thus, hits from a single particle trajectory will form a peak in the (ρ, ϕ) plane, while random hits will uniformly populate the plane. A two-dimensional histogram in (ρ, ϕ) is created with the collection of hits, and local maxima about seed clusters are sought. The HTF method performs well for medium to high p_T tracks that are well isolated from other track activity. The shortcomings of the HTF method include diminished performance in a high luminosity environment and low efficiency for tracks that produce few hits.

The second algorithm, called the *Alternative Algorithm* (AA) [110], utilizes a “road-following” methodology. This algorithm begins with a cluster of hits in the inner SMT layers and moves radially outward, searching for an additional hit within a small window in $\Delta\phi$. Further hits are then included if the track hypothesis satisfies $p_T > 180$ MeV and a minimum χ^2 requirement. The track is then extrapolated to the outer SMT layers and CFT, including additional hits if the contribution of a hit to the χ^2 of the track fit is less than a specified amount, and a maximum number of layer “hit misses” is not surpassed. The AA algorithm is also run from the CFT inward, as long as the CFT seeded track hypothesis is also matched to a SMT cluster in the inner layer. The AA algorithm requirements are strict, but the algorithm is well suited to maintaining efficiency in a high luminosity environment.

A supplementary algorithm, known as *hits-on-the-road* (HOR) [111], is employed in this analysis to search for a density of hits along a “road” defined by an EM object and the PV, as shown in Figure 5.1. The HOR variable reduces the rate that electrons are misidentified as photons in cases where the HTF and AA algorithms fail to identify the electron track. Given the energy measurement of the EM object and the PV location, and assuming a massless particle, a corresponding trajectory can be determined up to a two-fold ambiguity due to the unknown charge of the particle. If CPS clusters are associated with the EM object, they assist in defining a more precise road. Two roads are therefore defined, and the number of SMT and CFT hits within a narrow window about each road are counted. A

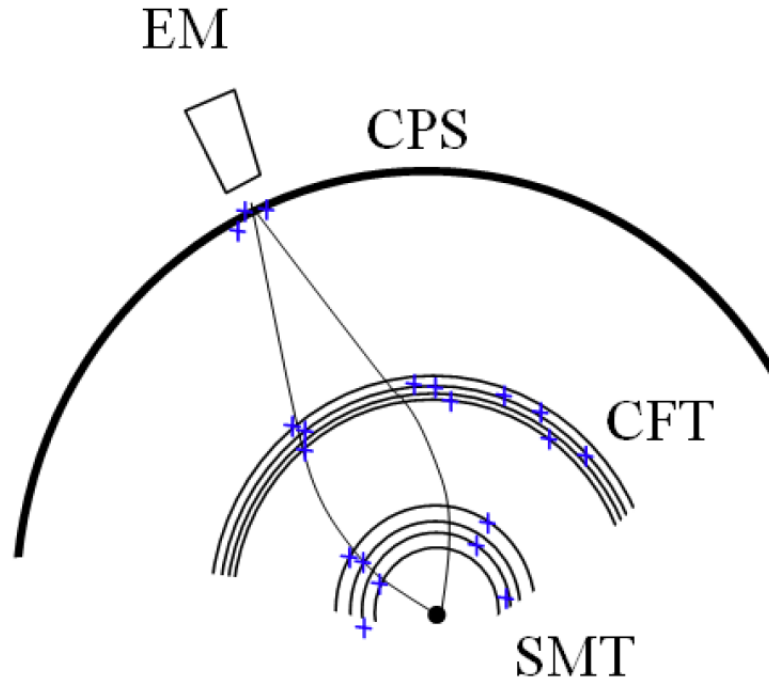


Figure 5.1: Illustration of the HOR algorithm. Two “roads” are defined as described in the text. SMT and CFT hits are searched for along the two roads. CPS clusters associated with the EM cluster assist in defining a more precise road.

distribution of the number hits created by electrons along the road is obtained using $Z \rightarrow ee$ data events. Similarly, a distribution of random hits is obtained by examining the directions perpendicular to the main calorimeter objects in $Z \rightarrow ee$ events and events containing two jets. A discriminating variable called HOR is built from these two hit number distributions, characterizing whether the number of hits observed along a road is more consistent with an electron or random hit activity.

5.2 Collision Vertex

On the order of ten $p\bar{p}$ collisions occur per bunch crossing at the highest instantaneous luminosities delivered by the Tevatron. Most triggered events, however, contain only one large momentum transfer, or “hard”, $p\bar{p}$ collision. The tracks created by charged particles

originating from this collision define the PV. The location of the PV defines the physics coordinate system, and thus the correct PV must be identified among the possibly several other “soft”, or “minimum bias”, collision vertices in order that quantities such as E_T and \cancel{E}_T are correctly measured.

The algorithm to reconstruct the PV proceeds by first grouping together tracks that contain at least two SMT hits, satisfy $p_T > 0.5$ GeV, and agree to within 2 cm in the z-coordinate at their closest approach to the z-axis. Next, an Adaptive Primary Vertex algorithm [112] fits the tracks to a common vertex hypothesis, and those tracks that contribute the most to the χ^2 of the fit are iteratively removed until the χ^2 is below a threshold value. At the end of this stage, several vertex candidates remain.

As the tracks from a hard collision typically have higher p_T than those from minimum bias collisions, a measure based on the p_T of the tracks associated with each vertex candidate is computed that assigns a probability that the given vertex is associated with a minimum bias collision [113]. The PV is defined to be the vertex with lowest minimum bias probability, and the typical resolution of the PV in the z-coordinate is $35 \mu\text{m}$. When the peak luminosity surpassed a certain value, the definition was slightly modified such that if the vertex with the lowest minimum bias probability has three tracks, and there exists another vertex (or vertices) with four or more tracks, the algorithm chooses the vertex with the most tracks [114].

The default PV algorithm and criteria are used in this analysis. Only events in which the PV has at least three tracks and is within $|z| < 60$ cm of the detector origin are selected.

5.3 Electromagnetic Objects

An electromagnetic object is a general term for a cluster of energy deposited primarily in the EM section of the calorimeter which satisfies properties similar to those of electrons and photons. The term is often used before the criteria that distinguish electrons, photons, and jets are specified. In this analysis, electrons and photons satisfy the same calorimeter and CPS based requirements that distinguish them from highly electromagnetic jets, but an electron has an associated track or high density of track hits, quantified by the HOR

variable, while photons do not.

Electrons and photons interact with absorber material in the calorimeter and initiate showers through bremsstrahlung ($e \rightarrow e\gamma$) and pair production ($\gamma \rightarrow e^+e^-$), respectively. The development of a shower reaches a maximum at $\approx 6 X_0$, and then attenuates exponentially, with $\approx 98\%$ of the shower contained within $22 X_0$. The nominal location of the shower maximum is at the more finely segmented third EM layer, though the introduction of new material during the upgrade [96] has resulted in shower development that is on average earlier. The transverse size of the shower is $\approx 3R_M$, where R_M is the Molière radius. Shower properties are very similar between electrons and photons, though the showers of photons start on average $\frac{9}{7}X_0$ further in the detector than those of electrons.

The simple cone algorithm [115] is used to identify clusters of energy in the EM calorimeter. The clustering algorithm begins with EM calorimeter towers satisfying $E_T > 0.5$ GeV, which consist of the cells in the four EM and first FH layer that are within a $(\Delta\eta \times \Delta\phi) = (0.1 \times 0.1)$ projective calorimeter tower. The towers are ordered according to E_T , and a $\Delta R = 0.4$ cone is defined about the highest E_T seed tower. The algorithm adds a new tower in the cone to the seed tower, computes an energy weighted position, and repeats this process with a new $\Delta R = 0.4$ cone until a stable cluster centroid is obtained. Any potential seed tower within the cone of a stable cluster is removed from the list of seeds, and the algorithm proceeds until there are no more seeds.

Final EM clusters are recomputed with cone size $\Delta R = 0.2$ and require at least 90% of the total energy be contributed by EM cells. To discriminate electrons and photons from jets, additional requirements are made that further restrict the fraction of hadronic energy behind the EM cluster, the fractional energy surrounding the EM cluster, and the number of nearby tracks. These and additional requirements are described in the next chapter.

The energy scale of EM clusters is calibrated with data using a very pure sample of $Z \rightarrow ee$ events. The calibration is performed as a function η_{det} and ϕ , and uses the precisely measured Z boson mass at the CERN LEP collider as a constraint in the calibration scheme [116; 117].

The segmentation of the EM calorimeter allows for good η and ϕ measurements of the cluster centroid. Additionally, “pointing” capability is achieved when the four EM

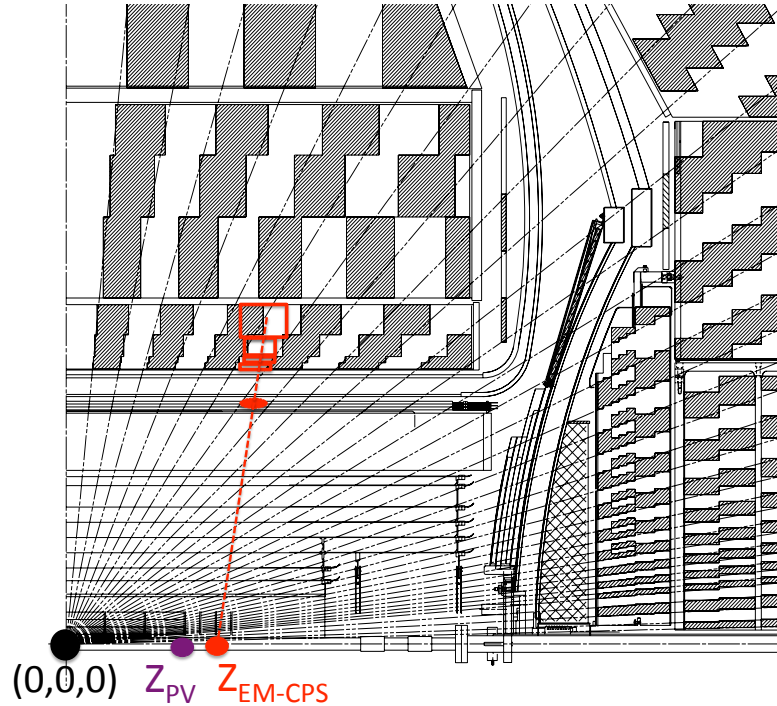


Figure 5.2: Illustration of the EM-CPS pointing algorithm. The figure depicts an EM cluster and associated CPS cluster match. The inferred z -coordinate in the plane $y = 0$ is labeled Z_{EM-CPS} , and can be compared with the z -coordinate of the PV, Z_{PV} .

layer measurements in a cluster are combined with associated CPS clusters, as shown in Figure 5.2. The EM-CPS pointing algorithm [118; 119] fits a straight line through the centroid position of each EM layer measurement and the average CPS cluster position of all clusters within a window in front of the EM cluster. The algorithm is used in this analysis to verify that photon candidates originate from the PV. Further details are provided in the next chapter.

5.4 Jets

As a result of the property of the strong interaction called *color confinement*, quarks and gluons produced in $p\bar{p}$ collisions *hadronize* to form collimated *jets* of multiple hadrons. This analysis allows jets to be present in the candidate $\gamma\gamma$ sample, as events with jets are common

in the signal models under consideration. However, an explicit requirement for jets to be present is not made. Jets are studied at several points in this analysis, particularly in regard to their impact on \cancel{E}_T .

The D0 jet algorithm [120] begins by assigning a four-momentum vector to each calorimeter cell, (E, \mathbf{p}) , where E is the energy measured in the cell, $|\mathbf{p}| = E$, and the direction of \mathbf{p} is defined by the line between the PV and cell center. Next, *jet tower* four-momentum vectors are built by summing the four-momenta of cells above a low energy threshold within pseudo-projective towers.

Pre-clusters are formed from the collection of jet towers. The jet towers are ordered according p_T , and all towers within a $\Delta R = 0.3$ cone about the leading p_T tower are assigned to the first pre-cluster. The next leading tower not already assigned to a pre-cluster defines the seed for the subsequent pre-cluster. The process continues until no more seeds towers remain.

The input to the cone algorithm used to construct jets is the collection of pre-clusters. A $\Delta R = 0.5$ cone (in $y \times \phi$ space, where y is rapidity) is defined about the leading pre-cluster, and other pre-clusters within the cone are iteratively added, as in the EM simple cone algorithm, until a stable object, called a *proto-jet*, is achieved. The next leading pre-cluster is considered, and if it is greater than $\Delta R/2$ away from the proto-jet, seeds the next proto-jet. The process continues until all pre-clusters are associated with proto-jets. With the collection of proto-jets defined, the midpoints between the proto-jets are also considered as seeds in order to reduce the likelihood that soft radiation could collapse two proto-jets.

The final step in jet reconstruction removes double counting of energy among the proto-jets. If the overlapping region of two proto-jets constitutes more than half the energy of either one, the two are merged. Otherwise, the proto-jets are split so that the constituent pre-clusters are associated with the closer proto-jet.

After the split/merge step, the jet energies are calibrated. A jet energy scale function [121] transforms the measured energy into one more closely matching the particle level energy. An energy offset correction is applied to account for noise and energy from additional soft $p\bar{p}$ collisions. Scale corrections account for the different response of individual particles in the jet, as well as the fraction of the particle jet energy contained within the

cone.

The jets considered in this analysis have $p_T > 15$ GeV and $|\eta_{det}| < 2.5$, and satisfy certain quality criteria to reduce the number of fake jets from noise. Further, some identified jets are found within $\Delta R < 0.4$ with respect to good photon candidates. These jets are considered equivalent to the photons, and therefore are removed from consideration as jets.

5.5 Missing Transverse Energy

The vector sum of the transverse momenta of all particles produced in a $p\bar{p}$ collision is expected to be zero. The vector sum of the transverse energy measured by calorimeter cells is defined as,

$$\vec{E}_T = \sum_i (E_{T,x}^i, E_{T,y}^i), \quad (5.1)$$

where

$$E_{T,x}^i = E^i \sin \theta^i \cos \phi^i \quad (5.2)$$

$$E_{T,y}^i = E^i \sin \theta^i \sin \phi^i, \quad (5.3)$$

and the sum is performed over all calorimeter cells with $|\eta_{det}| < 4$. The angles θ^i and ϕ^i define the direction from the origin of the physics coordinate system to the i^{th} calorimeter cell. The vector \vec{E}_T can be nonzero for a variety of reasons. First, stable neutral particles, such as neutrinos, do not deposit energy in the calorimeter, and create an imbalance of \vec{E}_T . Additionally, muons are minimum ionizing particles that typically deposit a small fraction of their energy in the calorimeter. Lastly, measurement errors arising from the energy resolution of the calorimeter can induce a non-zero \vec{E}_T , even if there are no neutrinos or muons in the event.

The uncorrected missing transverse energy vector is

$$\vec{\cancel{E}}_T = (\cancel{E}_{T,x}, \cancel{E}_{T,y}) \equiv -\vec{E}_T \quad (\text{uncorrected}). \quad (5.4)$$

The variable used in this analysis to distinguish signal and background events is the magnitude of the vector, \cancel{E}_T , after several corrections are applied [122; 123]. First, CH cells are not included in Equation 5.1 unless they are contained within well identified jets, as

the noise from these cells degrades the resolution of \vec{E}_T . If a jet is present, the associated cells are removed from the sum, and the fully calibrated jet E_T is added back in its place. Similarly, if an EM cluster satisfying shower properties consistent with an electron or a photon is identified in the event, the corresponding EM cells are removed and the fully calibrated cluster E_T is added back. The final correction accounts for muons in the event. Any calorimetric energy associated with the muon is removed from the sum, as it is accounted for when the reconstructed muon p_T is added.

Figure 5.3 shows the standard deviation of the corrected $\vec{E}_{T,x}$ distribution, $\sigma_{\vec{E}_{T,x}}$, as a function of the square-root of the scalar sum of the E_T of all calorimeter cells, $\sqrt{\sum E_T}$, in randomly triggered collision events. The data follow a linear dependence reflecting the stochastic term of the calorimeter resolution, and the slope, 0.42 in this class of events, quantifies the rate of decrease of \vec{E}_T resolution as a function of the total energy measured in the event.

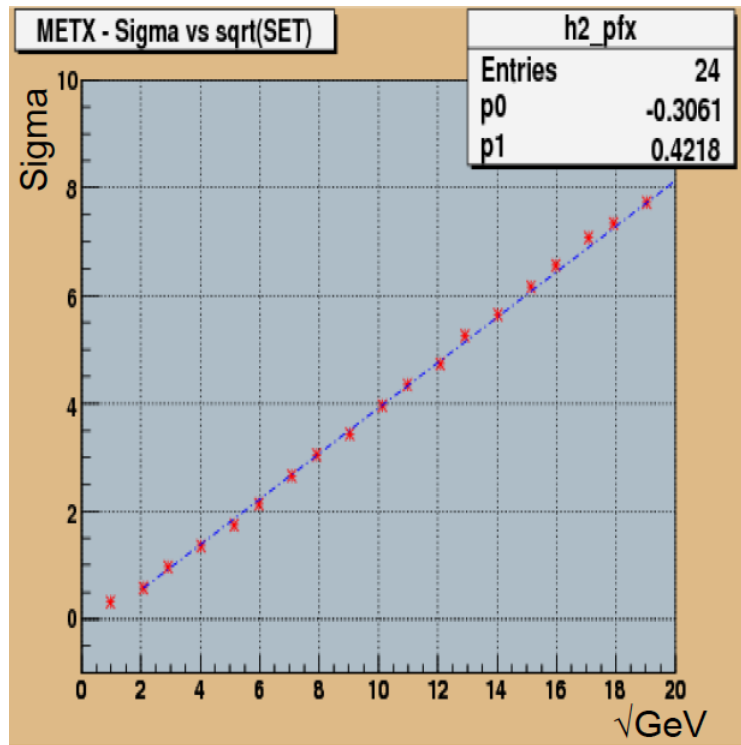


Figure 5.3: $\sigma_{\vec{E}_{T,x}}$ [GeV] versus $\sqrt{\sum E_T}$ in randomly triggered events [124].

Chapter 6

Data Samples and Event Selection

This chapter presents the data samples which are analyzed, and the selection of $\gamma\gamma$ candidate events. Simulated Monte Carlo (MC) samples for the signal and SM background processes are also introduced, as well as several independent data control samples that are used to estimate SM background contributions in the candidate $\gamma\gamma$ sample. After describing the basic event selection criteria, additional requirements are discussed that are targeted to reduce the number of events with significantly mismeasured \cancel{E}_T . Lastly, the efficiency for GMSB and UED MC events to satisfy the complete selection criteria is examined.

6.1 Data Samples

Events are selected from a set of data samples produced by the D0 Common Samples Group [125] for use in analyses containing two EM objects. These samples are listed in Table 6.1 and contain ~ 150 million events that are preselected to have at least two EM clusters with $E_T > 12$ GeV satisfying loose EM cluster selection criteria. The list constitutes the official “Summer 2010” dataset and is divided into four periods. In the following, Run IIa data are often also referred to as “p17 data”, and the data from the three periods of Run IIb are often collectively referred to as “p20 data”.

The analyzed events satisfy standard D0 data quality criteria. This analysis uses version v2010-03-11 of the data quality package (`dqdefs`) [126], which is specific to the Summer 2010 dataset. The data quality criteria require that events are selected from good lumi-

| Run Period, <i>Run Range</i> (reco) | Sample Definition | Events ($\times 10^6$) |
|--|--|-----------------------------|
| IIa (4/2002 - 2/2006) <i>151817 - 215670</i> (p17) | CSG_CAF_2EMhighpt_PASS3_p18.14.00 | 36.3 |
| IIb-1 (6/2006 - 8/2007) <i>221698 - 234913</i> (p20) | CSG_CAF_2EMhighpt_PASS2_p21.10.00 | 29.2 |
| IIb-2 (10/2007 - 6/2009) <i>237342-252918</i> (p20) | CSG_CAF_2EMhighpt_PASS4_p21.10.00_p20.12.00 | 9.4 |
| | CSG_CAF_2EMhighpt_PASS4_p21.10.00_p20.12.01 | 0.9 |
| | CSG_CAF_2EMhighpt_PASS4_p21.10.00_p20.12.02 | 19.6 |
| | CSG_CAF_2EMhighpt_PASS4_p21.10.00_p20.12.04 | 0.3 |
| | CSG_CAF_2EMhighpt_PASS4_p21.12.05_p20.12.05_allfix | 33.7 |
| IIb-3 (9/2009 - 3/2010) <i>255329 - 259547</i> (p20) | CSG_CAF_2EMhighpt_PASS5_p21.18.00_p20.16.07_fix | 10.0 |
| | CSG_CAF_2EMhighpt_PASS5_p21.18.00_p20.16.07_summer2010 | 12.1 |
| 2002 - 2010 | | 151.5 |

Table 6.1: Data samples in the D0 Common Sample Group's Summer 2010 2EM dataset.

nosity blocks in good runs in which all subdetector systems are in a good state. Events are discarded if they are flagged by standard tools [105] for certain anomalous calorimeter noise patterns. In addition, analyzed events must have been triggered by at least one of a standard set of triggers that require a single EM object. The efficiency of this trigger combination [127] is $\approx 99\%$ for the kinematic requirements of this analysis, and a conservative 2% systematic uncertainty on this efficiency is assigned. The full dataset corresponds to an integrated luminosity of $6.3 \pm 0.4 \text{ fb}^{-1}$ [106], with the p17 data contributing 1.1 fb^{-1} and the p20 data contributing 5.2 fb^{-1} .

6.2 Simulated Samples

Simulated MC samples for the SM processes studied are listed in Table 6.2. Many of the samples were generated with PYTHIA [128], and version v6.409 is used unless stated otherwise. The processes are direct photon pair production (SM $\gamma\gamma$), Drell-Yan production of a Z boson that decays to an electron and positron ($Z \rightarrow ee$), QCD multijet production, a W boson produced in association with a photon ($W\gamma$), and a Z boson produced in association with a photon ($Z\gamma$). The multijet sample, referred to as “EM-jet MC”, was filtered to contain more events with highly electromagnetic jets for use in studying the properties of fake photon candidates from misidentified jets. MC events with a W boson produced in association with jets ($W + \text{jets}$) were generated using ALPGEN [129] for different numbers of light partons (lp) in the final state. The parton level events were then processed with PYTHIA to create events with hadrons. Similarly, events with W and Z bosons produced in association with two photons ($W/Z + \gamma\gamma$) were generated with MADGRAPH [130] followed by PYTHIA.

With the exception of the small $W/Z + \gamma\gamma$ contribution estimated with MC, all SM background components in the $\gamma\gamma$ sample are estimated using methods that derive the contributions from data. The MC samples listed in Table 6.2 are generally used to study and verify certain assumptions about the properties of background events, provide cross-checks to the data based estimation methods, and deduce selection efficiencies in MC that are compared with, and sometimes corrected by, measurements with data in dedicated studies. The context in which each SM process sample is used is given in the table.

Table 6.3 lists the samples generated for signal model MC events. The particle masses, decay widths, and branching ratios for the GMSB SPS8 model were computed with SUSYHIT [69] and interfaced with PYTHIA to produce MC events. PYTHIA v.6421 is used for the computation of UED particle masses, decay widths, and branching ratios, as well as for the generation of MC events [84]. The cross section for each point is listed in the table. For GMSB, the cross section is the NLO value calculated with PROSPINO [70], while for UED the cross section is the LO value and obtained from PYTHIA. The NLO cross section prediction for UED has not yet been computed.

All MC samples used in this analysis have been generated using `cteq611.LHpdf` par-

ton distribution functions [131]. The events are processed with a full GEANT [132] based simulation of the D0 detector and reconstructed with the same algorithms that are applied to data. Although the detector performance is in general modeled very well, certain features in simulated events do not sufficiently match those of data events, and corrections must therefore be applied to the MC events. The corrections are implemented as “weights” which are applied to simulated events in order that the distribution of a discrepant variable matches, in weighted simulated events, the distribution observed in data. For example, MC events overlay real data collected with random triggers in order to better model effects from the possibly several soft collisions that may occur in the same beam crossing as the hard collision. However, the randomly triggered data are not typically collected with the same instantaneous luminosity spectrum as the selected data. Therefore, a weight is applied to each simulated event such that the luminosity spectra of MC and data agree. Likewise, a correction is applied to the z-position of the PV. The z-position distribution is slightly non-Gaussian in data, while it is a perfect Gaussian in simulation.

Several EM object weights are applied as well. A trigger weight accounts for the difference in trigger efficiency as a function of the E_T of the EM cluster [127]. The D0 EMID group certifies electron and photon [7] identification criteria, and part of the certification effort involves measuring with data the corrections which must be applied to MC events in order that the object performance is similar in data and MC. These correction factors account for small efficiency and energy resolution differences between data and MC. Data events from a high purity $Z \rightarrow ee$ sample are extensively used to measure the energy resolution of an EM cluster and the efficiency to pass certain calorimeter based requirements. Many of the calorimeter performance results with $Z \rightarrow ee$ can be applied to photons as well, as electrons and photons leave similar energy depositions in the calorimeter. $Z(\rightarrow ll)\gamma$ ($l = e, \mu$) data events, though more rare than $Z \rightarrow ee$ events, are also studied carefully to test the performance of a photon specific neural network variable used to reject fake candidates from misidentified jets, and to measure the efficiency for photons to pass an associated track veto.

| Process | Generator | ReqID | Use |
|---|-----------------|----------------------------------|---|
| SM $\gamma\gamma$ ($m_{\gamma\gamma} = 50 - 130$ GeV) | PYTHIA | 80052-3 90252-3 99619-21 | (i) induced \cancel{E}_T from PV misID (Sec. 6.5) (ii) $\gamma\gamma$ and ee \cancel{E}_T comparison (Sec. 7.1.1) |
| SM $\gamma\gamma$ ($m_{\gamma\gamma} = 130 - 250$ GeV) | PYTHIA | 90254 | |
| SM $\gamma\gamma$ ($m_{\gamma\gamma} = 250 - 500$ GeV) | PYTHIA | 110281 | |
| $Z \rightarrow ee$ ($m_{ee} = 60 - 130$ GeV) | PYTHIA | 86882-6 | $\gamma\gamma$ and ee \cancel{E}_T comparison (Sec. 7.1.1) |
| Filtered QCD Multijet ("EM-jet MC") | PYTHIA | 93013-16 93174,93187 93196 | fake photon NN shape (Sec. 6.3, 7.2.1) |
| W + jets (1 lp) | ALPGEN-PYTHIA | 100622 | W + jet \cancel{E}_T shape for $e\gamma + \cancel{E}_T$ contribution (Sec. 7.2.1) |
| W + jets (2 lp) | ALPGEN-PYTHIA | 100632 | |
| W + jets (3 lp) | ALPGEN-PYTHIA | 100682 | |
| W + jets (4 lp) | ALPGEN-PYTHIA | 100696 | |
| W + jets (≥ 5 lp) | ALPGEN-PYTHIA | 100700 | |
| $W\gamma$ | PYTHIA | 88458 | $e\gamma + \cancel{E}_T$ contribution (Sec. 7.2.1) |
| $W\gamma$ | PYTHIA | 88459 | |
| $Z\gamma$ | PYTHIA | 88452 | PhotonID (Sec. 6.3) CPS-PV pointing (Sec. 6.5) |
| $Z\gamma$ | PYTHIA | 88454 | |
| $Z\gamma$ | PYTHIA | 90532 | |
| $Z\gamma$ | PYTHIA | 90534 | |
| $W + \gamma\gamma$ | MADGRAPH-PYTHIA | 121313, 119933 | $\gamma\gamma + \cancel{E}_T$ bkgd (Sec. 7.2.2) |
| $Z + \gamma\gamma$ | MADGRAPH-PYTHIA | 121314, 119934 | |

Table 6.2: MC samples for SM processes. The first column lists the process, the second the generator used to produce the MC events, the third a unique sample identification number, and the last the context in which the sample is used in this analysis.

| Process | ReqID (p17, p20) | σ (fb) |
|-------------------------------|------------------|---------------|
| SPS8 GMSB $\Lambda = 80$ TeV | 121301, 119961 | 90.4 |
| SPS8 GMSB $\Lambda = 90$ TeV | 121303, 119963 | 43.6 |
| SPS8 GMSB $\Lambda = 100$ TeV | 121305, 119965 | 21.7 |
| SPS8 GMSB $\Lambda = 110$ TeV | 121307, 119967 | 11.0 |
| SPS8 GMSB $\Lambda = 120$ TeV | 121309, 119969 | 5.70 |
| SPS8 GMSB $\Lambda = 130$ TeV | 121311, 119971 | 2.99 |
| SPS8 GMSB $\Lambda = 135$ TeV | 122393, 122396 | 2.19 |
| UED $R_c^{-1} = 380$ GeV | 121292, 119952 | 103 |
| UED $R_c^{-1} = 400$ GeV | 121293, 119953 | 52.8 |
| UED $R_c^{-1} = 420$ GeV | 121294, 119954 | 26.7 |
| UED $R_c^{-1} = 440$ GeV | 121295, 119955 | 13.3 |
| UED $R_c^{-1} = 460$ GeV | 121296, 119956 | 6.52 |
| UED $R_c^{-1} = 480$ GeV | 121297, 119957 | 3.15 |
| UED $R_c^{-1} = 500$ GeV | 121298, 119958 | 1.47 |

Table 6.3: PYTHIA MC samples for GMSB and UED signal events. The GMSB events were generated according to the previously defined SPS8 parameter set, while the UED events were generated setting the cut-off $\tilde{\Lambda}R_c = 20$, $N = 6$ large extra dimensions, and fundamental Planck scale $M_D = 5$ TeV. The first column lists the model and energy scale parameter specified for the given sample, and the second a unique sample identification number. Each sample number corresponds to 20k simulated events. The last column gives the NLO cross section for GMSB and the LO cross section for UED.

6.3 Selection of the Diphoton Sample

Diphoton candidate events are selected by requiring at least two photon candidates identified in the central cryostat (CC) region, $|\eta_{det}| < 1.1$, with both satisfying $E_T > 25$ GeV. The photon candidates are required to pass the “CCcore1” identification requirements defined and optimized in Reference [7]. The main variables that comprise this definition, and the corresponding requirements, are:

- EM fraction (EMfrac): $EMfrac > 0.95$
- Calorimeter Isolation (CaloIso): $CaloIso < 0.10$
- Track Isolation (TrkIso): $TrkIso < 2.0$ GeV
- EM3 shower width (EM3w): $EM3w < 14(18)$ cm²
- Track Veto (TrkVeto): $TrkPrb < 0.0001(0)$ and $HOR < 0.5(0.9)$.
- Photon neural net (NN): $NN > 0.10$

A number in parentheses is the value applied in p20 data, if different than the value applied in p17 data.

EMfrac is defined as $E_{EM}(0.2)/E_{tot}(0.2)$, where $E_{EM}(0.2)$ is the EM energy within a $\Delta R = 0.2$ cone about the cluster centroid, and $E_{tot}(0.2)$ is the total EM+HAD energy within the same $\Delta R = 0.2$ cone. CaloIso is defined as $(E_{tot}(0.4) - E_{EM}(0.2))/E_{EM}(0.2)$, and quantifies the amount of EM+HAD energy just outside the cluster relative to the EM cluster energy. TrkIso is defined as the scalar sum of the transverse momenta of all $p_T > 0.5$ GeV tracks in a $0.05 < \Delta R < 0.40$ hollow cone about the EM cluster centroid. EM3w, referred to as *sigphi* in some references, is the energy weighted shower width squared measured in the third EM layer of the calorimeter. TrkProb is the χ^2 probability that a track is matched to the EM cluster, and HOR is the hits-on-the-road variable [111].

Figure 6.1 shows the distributions of the first four variables listed above for photons in $Z\gamma$ data and MC, and demonstrates good agreement between data and simulation. The $Z\gamma$ sample study is described in Reference [7] and was performed with the primary objective of measuring the EM-CPS pointing performance in data. The results of this study are

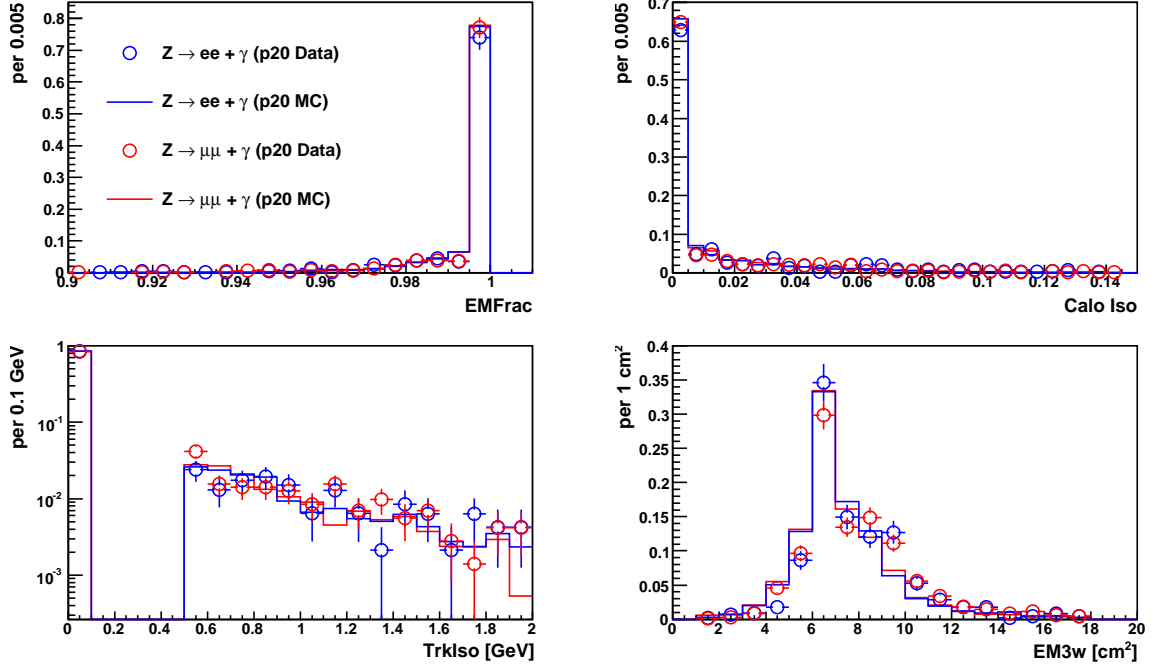


Figure 6.1: Distributions for the photons in $Z\gamma$ data and MC events of the EM fraction, calorimeter isolation, track isolation, and EM3 shower width variables.

presented in Section 6.5. The photon candidates in the pointing study satisfy a looser set of requirements and $E_T > 10$ GeV.

Figure 6.2 presents the distributions in $Z \rightarrow ee$ and SM $\gamma\gamma$ MC events for the variables which comprise the track veto. The left plot shows the TrkProb variable. The region to the left of the arrow indicates that $\sim 93\%$ of photons and $\sim 3\%$ of electrons pass the requirement. The HOR variable is shown in the right plot for all TrkProb values. Additionally, to illustrate the shape of the distribution when a good track match is not identified, the HOR variable is shown for only those electrons that pass the TrkProb requirement. The HOR requirement suppresses those electrons passing the TrkProb requirement by a factor of 2, while remaining very efficient for photons. The photon efficiency to pass the TrkVeto is measured with data using $Z\gamma$ data events, while the rate an electron fakes a photon is measured using $Z \rightarrow ee$ events. The TrkVeto efficiency for photons is determined to be 0.898 ± 0.019 , and the $e \rightarrow \gamma$ fake to be 0.020 ± 0.005 [135; 7].

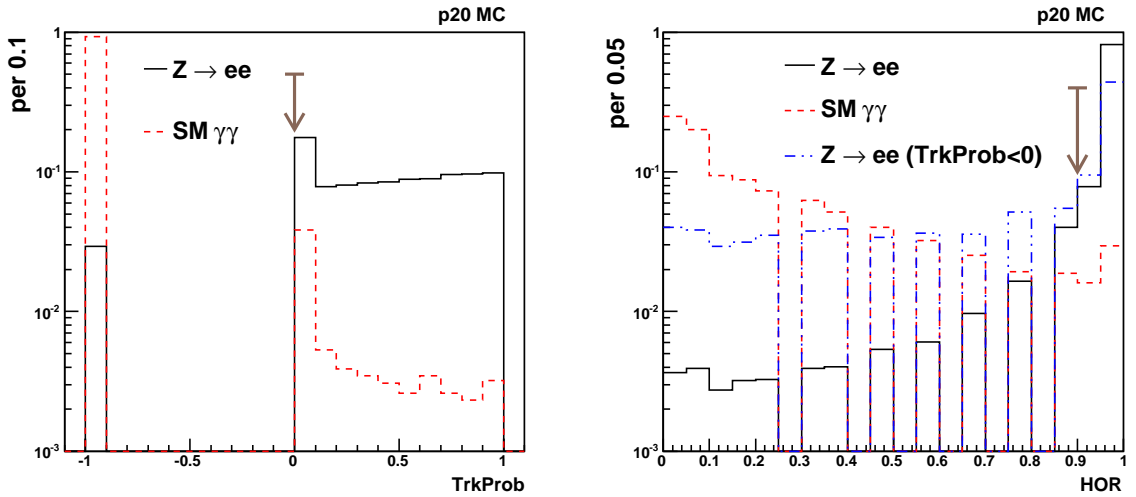


Figure 6.2: Distributions for variables used to define the track veto. The TrkProb variable is shown in the left plot for SM $\gamma\gamma$ and $Z \rightarrow ee$ MC events. The HOR variable is shown in the right for all values of TrkProb, and also for only those electrons in $Z \rightarrow ee$ events that pass the TrkProb requirement. The requirements on the variables are denoted by arrows.

The photon NN variable [133; 134; 135; 136; 7] uses the following five discriminating variables:

- the number of first layer EM cells in the cluster with $E > 450$ MeV in a $\Delta R < 0.20$ cone about the cluster centroid
- the number of first layer EM cells in the cluster with $E > 450$ MeV in a $0.20 < \Delta R < 0.40$ hollow cone about the cluster centroid
- track isolation (TrkIso)
- the number of CPS clusters in a $\Delta R < 0.10$ cone about the cluster centroid
- the energy weighted CPS RMS in ϕ [137].

The top plot of Figure 6.3 shows the NN distribution for photons in $Z\gamma$ data events. The bottom plot shows the NN distribution in events from a fake photon enriched data sample that is obtained using inclusive photon selection requirements with the exception that

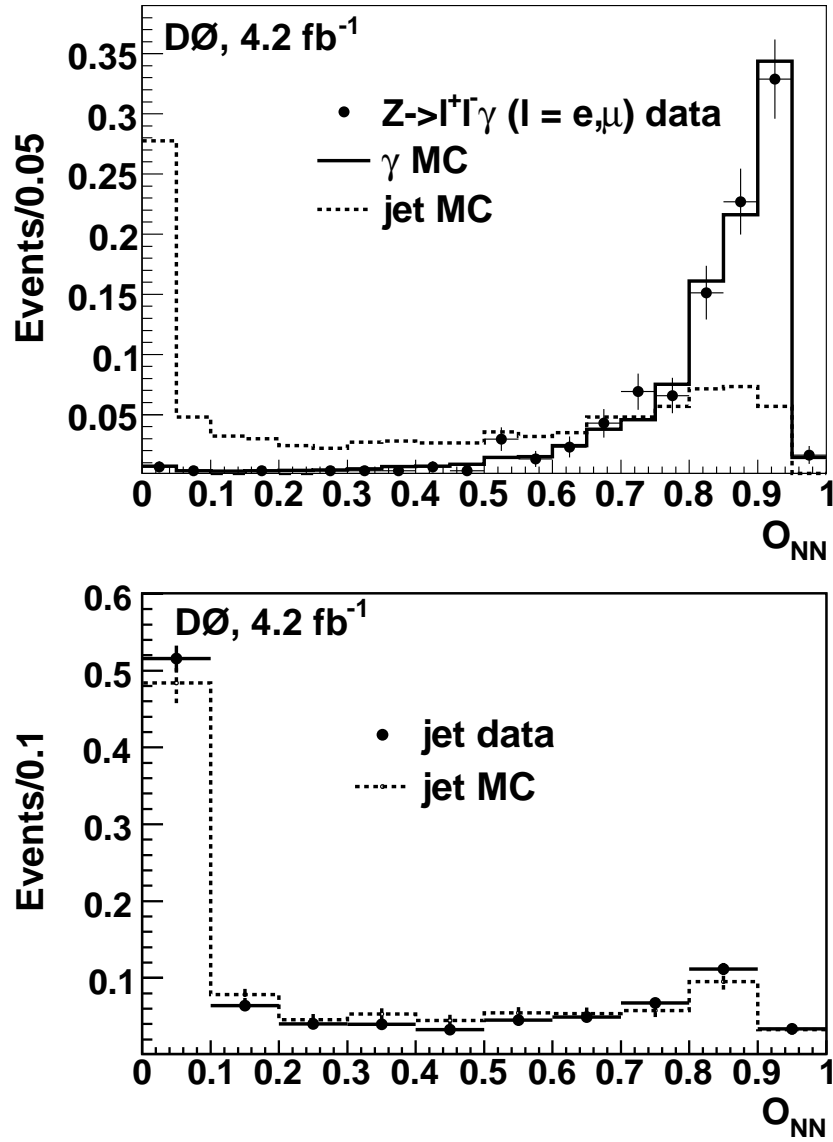


Figure 6.3: The distribution of the NN variable (here labeled O_{NN} [136]) is shown for photons in $Z\gamma$ data (top) and data enriched with fake photon candidates from jets (bottom). Distributions in MC events with real photons (solid line) and fake photons (dashed lines) are also shown.

photon candidates fail the CaloIso requirement. Good separation is observed between real photons and fake candidates from jets. Corresponding distributions are shown for real and fake photons from MC events, and demonstrate good agreement with the data.

6.4 Selection of Data Control Samples

Several data control samples are used to study the properties of SM backgrounds to the $\gamma\gamma$ sample and to construct a prediction for the \cancel{E}_T distribution. These samples are derived from a preselected sample of two EM objects (diEM sample) that also contains the $\gamma\gamma$ sample. The E_T , $|\eta_{det}|$, EMfrac, and CaloIso requirements remain the same as those used to define the $\gamma\gamma$ sample. Table 6.4 defines four pass/fail categories based on the remaining variables used for photon selection. The NN and TrkVeto categories reflect whether or not a candidate EM cluster passes the photon NN and TrkVeto requirements. Likewise, the IsEM-T(ight) category reflects whether a candidate EM cluster passes both the EM3w and TrkIso requirements. The IsEM-L(oose) category is a superset of IsEM-T(ight) with looser requirements on the EM3w and TrkIso variables.

Table 6.5 defines how these categories partition the selected diEM sample into independent, nonoverlapping subsamples. The two entries per category in Table 6.5 correspond to the two EM objects. Cases where there are two rows per subsample indicate that a logical OR is applied. Therefore, both EM objects in $\gamma\gamma$ sample events are required to pass the TrkVeto, pass the IsEM-T requirement, and pass the NN requirement. Similarly, the ee sample requirements are the same as those for the $\gamma\gamma$ sample except that both EM objects fail the TrkVeto, while $e\gamma$ sample events require that one *or* the other EM object fails the TrkVeto.

| Category | Selection |
|--------------|--|
| NN | NN > 0.10 |
| TrkVeto | TrkPrb < 0.0001(0) and HOR < 0.5(0.9) |
| IsEM-T(ight) | EM3w < 14(18) cm ² and TrkIso < 2.0 GeV |
| IsEM-L(oose) | EM3w < 100 cm ² and TrkIso < 5.0 GeV |

Table 6.4: Categories based on the photon identification variables which are used to partition the preselected diEM dataset into independent subsamples. Numbers in parentheses indicate p20 values, if different than p17 values.

| Sample | TrackVeto | | IsEM-L | | IsEM-T | | NN | |
|----------------|-----------|---|--------|---|--------|---|----|---|
| $\gamma\gamma$ | P | P | P | P | P | P | P | P |
| ee | F | F | P | P | P | P | P | P |
| $e\gamma$ | F | P | P | P | P | P | P | P |
| | P | F | P | P | P | P | P | P |
| jet misID | P | P | P | P | - | - | F | - |
| | P | P | P | P | - | - | - | F |
| eh | F | P | P | P | P | - | P | F |
| | P | F | P | P | - | P | F | P |

Table 6.5: The preselected diEM dataset is divided into several subsamples according to whether one EM cluster, both, or neither passes the TrkVeto, IsEM, and NN criteria. Two rows per subsample indicate that a logical OR is applied. A hyphen denotes the question is not asked.

Events in which a jet has been misidentified as a photon are studied with samples that require an EM object which fails the NN requirement. For example, the jet misID sample, which is used to model QCD multi-jet backgrounds, requires that at least one of the EM objects fails the NN requirement, potentially both (the hyphen in Table 6.5 means the question is not asked). Figure 6.4 illustrates how the NN requirement divides the TrkVeto pass-pass portion of the diEM sample (combined $\gamma\gamma$ / jet misID sample) further into the $\gamma\gamma$ (IV) and jet misID (I+II+III) subsamples. The eh sample is defined similarly to the $e\gamma$ sample except that the EM cluster which passes the TrkVeto is required to fail the NN.

Simply inverting the NN requirement typically does not yield samples of sufficient size to estimate the backgrounds to the desired precision. Therefore, the IsEM-T criteria is loosened to IsEM-L. The process of relaxing the IsEM requirement for the jet misID sample is discussed in Section 7.1.2. Care must be taken to avoid introducing a possible bias in the resulting \cancel{E}_T distribution.

The number of events in each sample is provided in Table 6.6. The numbers of events are listed after the diEM selection described to this point, as well as after the primary vertex

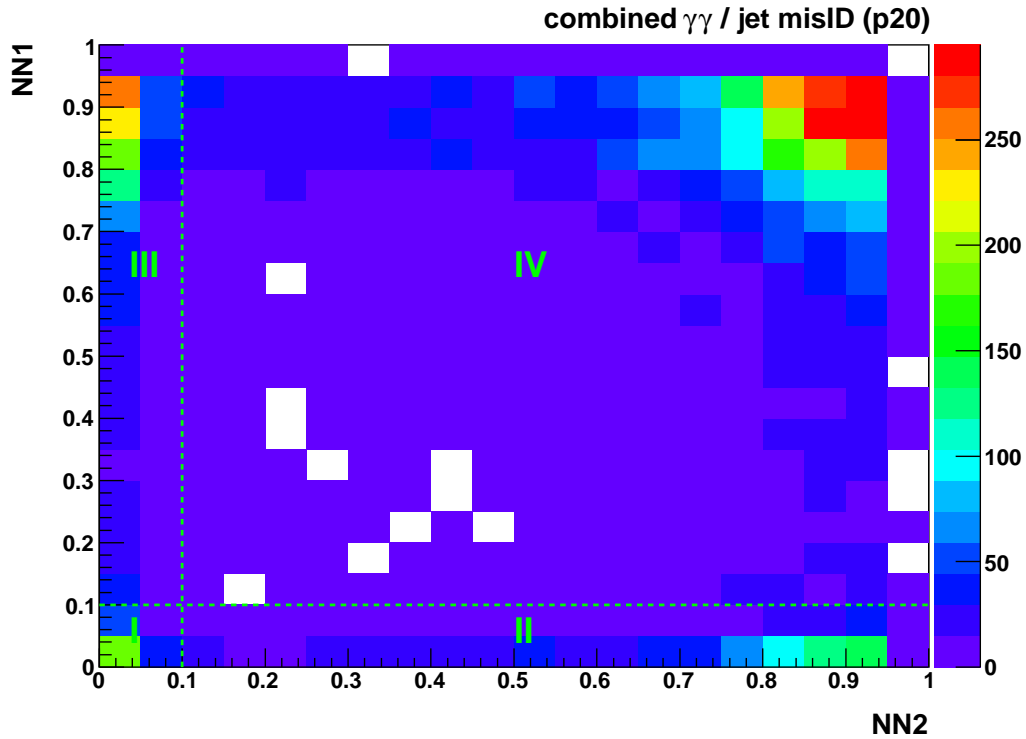


Figure 6.4: Leading EM NN vs. trailing EM NN for the combined $\gamma\gamma$ / jet misID sample. The fail-fail region (I) is rich in dijet events, while the pass-fail regions (II and III) are rich in γ -jet events. Together, regions I, II, and III form the jet misID sample with the IsEM-T criteria. The pass-pass region (IV) is the selected $\gamma\gamma$ data sample.

and $\Delta\phi$ requirements described next.

6.5 Primary Vertex Requirement

The default D0 PV algorithm is used in this analysis. The left plot of Figure 6.5 shows the difference in z-position between the reconstructed and truth PV, $\Delta Z_{PV}(\text{Truth}, \text{Reco})$, in SM $\gamma\gamma$ MC events. The fraction of events with $\Delta Z_{PV}(\text{Truth}, \text{Reco}) < 10$ cm is $\sim 80\%$. The relatively high degree of PV identification inefficiency reflects the fact that SM $\gamma\gamma$ events do not typically produce many tracks. SM $\gamma\gamma$ and other background events with low vertex activity may therefore enter the $\gamma\gamma$ candidate sample with an incorrectly identified

| | p17 (1.1 fb ⁻¹) | | | p20 (5.2 fb ⁻¹) | | |
|----------------|------------------------------|-----------|-------------------|------------------------------|-----------|-------------------|
| Sample | N(diEM) | N(CPS-PV) | N($\Delta\phi$) | N(diEM) | N(CPS-PV) | N($\Delta\phi$) |
| $\gamma\gamma$ | 2,921 | 2,166 | 1,561 | 16,349 | 11,828 | 6,373 |
| ee | 26,951 | 20,922 | 19,263 | 135,296 | 103,509 | 87,777 |
| $e\gamma$ | 2,282 | 1,678 | 1,264 | 16,635 | 12,128 | 6,913 |
| jet misID | 21,313 | 15,064 | 6,995 | 65,554 | 45,831 | 19,245 |
| eh | 2,148 | 1,526 | 857 | 11,635 | 8,082 | 3,745 |

Table 6.6: The number of events in each diEM subsample after partitioning the preselected diEM dataset, after the CPS-PV agreement requirement is applied, and lastly after the three $\Delta\phi$ requirements are applied.

PV, and hence mismeasured \cancel{E}_T . The right plot of Figure 6.5 shows the \cancel{E}_T distribution in events with a correctly identified PV events on top of a harder \cancel{E}_T distribution from events with a misidentified PV. The highest \cancel{E}_T events result when the true and reconstructed PV z-position disagree by 30 cm or more.

In GMSB and UED signal events, the additional activity associated with the cascade decays of the SUSY and UED particles results in an efficiently identified PV ($\sim 99\%$). Therefore, it is sufficient to use the default PV in conjunction with EM-CPS pointing in order to confirm the selected PV and discard those events which fail the confirmation. The confirmation protects against SM events with a misidentified PV and subsequent large induced \cancel{E}_T . Figure 6.6 demonstrates the effectiveness of the pointing confirmation in SM $\gamma\gamma$ MC. The confirmation is efficient for events with a correctly identified PV, shown on the left, as little difference is observed before and after the confirmation. On the right, the pointing requirement greatly reduces the rate of those events with a misidentified PV.

In order to verify the MC photon pointing performance in data, a study of $Z\gamma$ data events was performed [7]. The photon EM cluster must have an associated CPS cluster in order to utilize the EM-CPS pointing algorithm. The match efficiency as a function of η_{det} is shown in the top plot of Figure 6.7 and is 72% in data and 77% in MC. The bottom plot shows the difference between the z-coordinate inferred by EM-CPS pointing and that

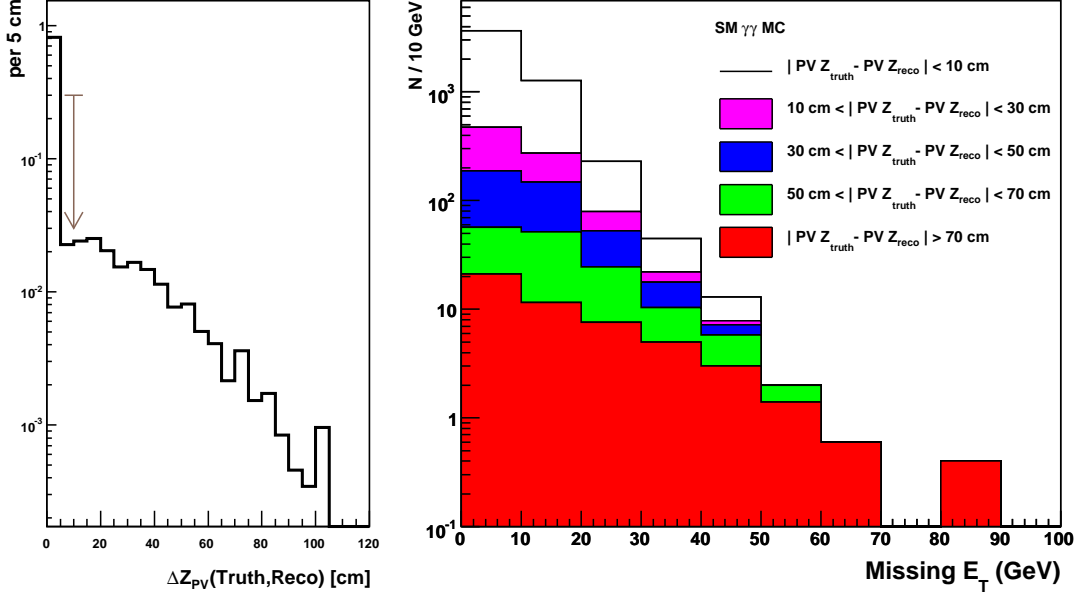


Figure 6.5: The difference in z-position between the reconstructed and truth PV, $\Delta Z_{PV}(\text{Truth}, \text{Reco})$, in SM $\gamma\gamma$ MC events (left). The \cancel{E}_T distribution is shown stacked according to intervals of ΔZ_{PV} (right).

of the PV, $\Delta Z(\text{CPS}, \text{PV})$. The resolution is ~ 3.8 cm in data and ~ 2.5 cm in MC (to be compared with the $\sigma_z \sim 25$ cm spread in the distribution of collision vertices), and the efficiency to pass a $\Delta Z(\text{CPS}, \text{PV}) < 10$ cm requirement is 94% in data and 97% in MC. In general, Figure 6.7 indicates that the CPS performance is somewhat overestimated in MC. The overall match efficiency is 5% lower in data, though the data confirms the material effect causing the η_{det} dependence seen in MC. A scale factor, discussed below, is applied to the MC to account for the higher CPS match efficiency in MC. Concerning the z-position agreement, the difference in resolution is small in comparison with the spread in vertex position, indicating the pointing algorithm is effective. A $\Delta Z(\text{CPS}, \text{PV}) < 10$ cm requirement is sufficiently tight to suppress potential induced \cancel{E}_T , but the difference in efficiency must be taken into account.

In this analysis, all diEM subsample events are required to have *at least one* EM cluster with a CPS match. Using the single CPS match efficiencies quoted above this requirement

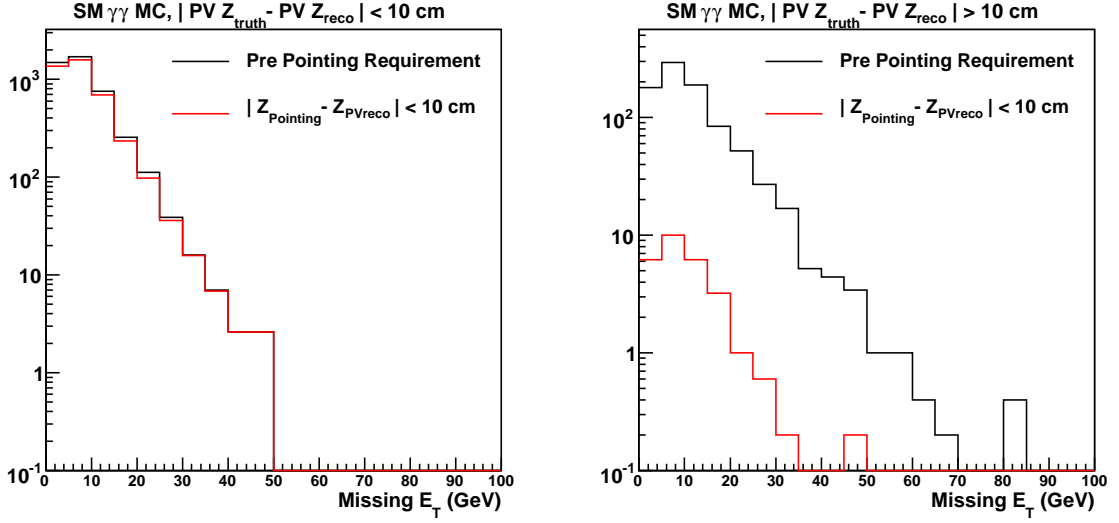


Figure 6.6: The left plot shows the \cancel{E}_T distribution in SM $\gamma\gamma$ MC events with a correctly identified PV, $\Delta Z_{PV}(\text{Truth}, \text{Reco}) < 10$ cm, before and after the EM-CPS pointing confirmation. Similarly, events with an incorrectly identified PV, $\Delta Z_{PV}(\text{Truth}, \text{Reco}) > 10$ cm, are shown on the right.

is 92% efficient for data and 95% for MC. If the event has only one match, the CPS-PV z-position agreement must be within 10 cm. If both clusters have matches, the CPS-CPS agreement must be within 10 cm, and the average CPS z-position must agree to within 7 cm with the PV. A scale factor of 0.94, the ratio of the combined CPS match and ΔZ efficiencies in data and MC, is applied to the signal and $W/Z + \gamma\gamma$ MC samples entering the final \cancel{E}_T analysis. A 3% systematic uncertainty is assigned to this scale factor, primarily arising from the statistical error associated with the $Z\gamma$ sample size.

6.6 Requirements to Reduce Instrumental Sources of \cancel{E}_T

Three topological requirements are applied to reduce various sources of \cancel{E}_T mismeasurements:

- $\Delta\phi(\text{EM}, \text{EM}) > 0.1$
- $\Delta\phi_{\min}(\text{EM}, \cancel{E}_T) > 0.2$

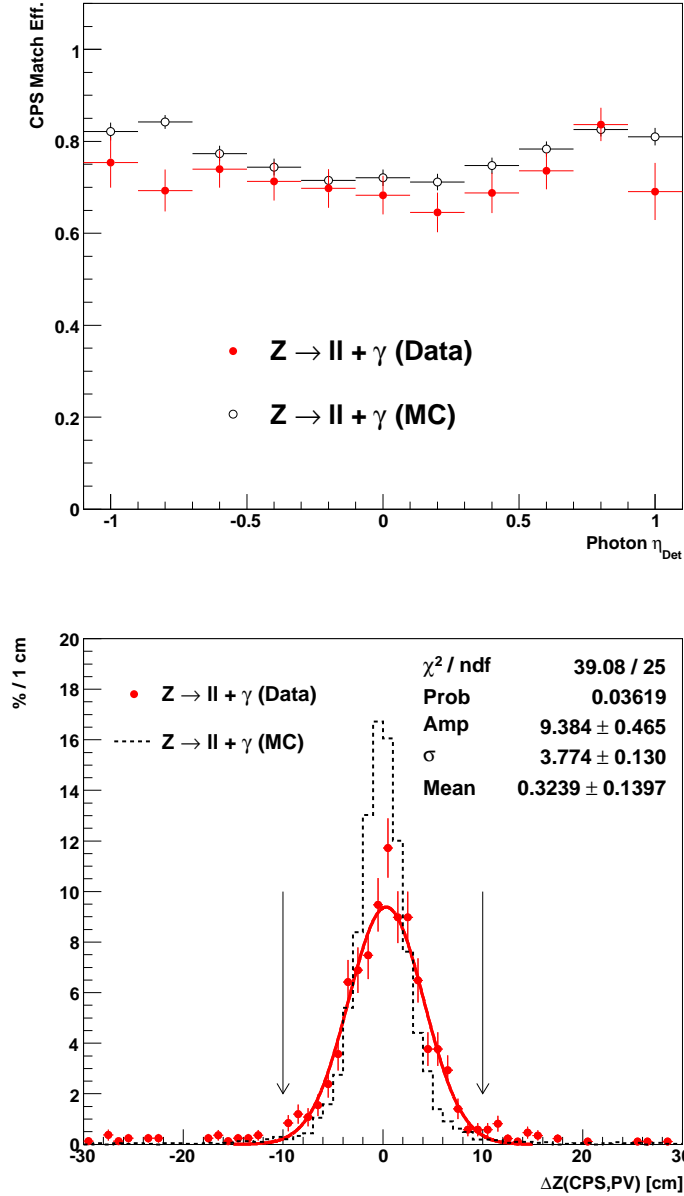


Figure 6.7: The CPS match efficiency as a function of η_{det} in $Z\gamma$ data and MC (top). The difference in z-position between the reconstructed PV and that predicted by EM-CPS pointing (bottom). The arrows indicate the interval of agreement required for the pointing confirmation.

- $\Delta\phi(\text{Leading Jet}, \cancel{E}_T) < 2.5$, if jet(s) present.

This section describes the motivation and implementation of each $\Delta\phi$ requirement.

6.6.1 $\Delta\phi(\text{EM}, \text{EM})$

The purpose of the $\Delta\phi(\text{EM}, \text{EM})$ requirement is to reduce the impact of non-collision background events, in particular beam halo events. Histogram (1) of Figure 6.8 shows the $\Delta\phi(\gamma, \gamma)$ distribution in data events without imposing the pointing requirements (neither the CPS match, nor the $\Delta Z(\text{CPS}, \text{PV})$ requirement), and for any number of jets in the event. A clear excess of events is observed at $\Delta\phi(\gamma, \gamma) \sim 0$. The excess becomes more prominent when the sample is restricted to $N_{\text{jet}} = 0$, shown in histogram (2), as expected since the diphoton system is less likely to be recoiling against a hadronic system. When at least one CPS match is required, as shown in histogram (3), the accumulation of events near zero is almost entirely removed. This observation suggests the peak is a result of beam halo particles originating upstream of the detector and traveling roughly parallel to the beamline. Selecting the $\Delta\phi(\gamma, \gamma) < 0.1$ events for further investigation, the bottom left plot of Figure 6.8 reveals the average of the ϕ coordinates of the two photon candidates tends to be near 0 or π , consistent with the upstream beam optics and beam halo hypothesis. Lastly, the \cancel{E}_T direction in these events is strongly peaked opposite to the average ϕ photon coordinate candidates, as shown in the bottom right plot.

Although the CPS match requirement is highly effective in reducing beam halo events, a few such events remain after the match requirement. As the EM clusters are each required to satisfy $E_T > 25$ GeV, \cancel{E}_T in these events is at least ~ 50 GeV. In order to suppress surviving beam halo events after the CPS match and pointing requirements are applied, a $\Delta\phi(\text{EM}, \text{EM}) > 0.1$ requirement is imposed. The $\Delta\phi(\gamma, \gamma)$ distribution is relatively flat for signal model events, with a slight increase for increasing $\Delta\phi(\gamma, \gamma)$. The efficiency of the $\Delta\phi(\gamma, \gamma) > 0.1$ requirement in signal events is $\sim 98\%$.

6.6.2 $\Delta\phi_{\min}(\text{EM}, \cancel{E}_T)$

Figure 6.9 shows the $\Delta\phi$ distribution between \cancel{E}_T and the EM cluster that yields the smaller $\Delta\phi$ value, $\Delta\phi_{\min}(\text{EM}, \cancel{E}_T)$, in p17 and p20 jet misID sample events with $\cancel{E}_T > 20$ GeV. The

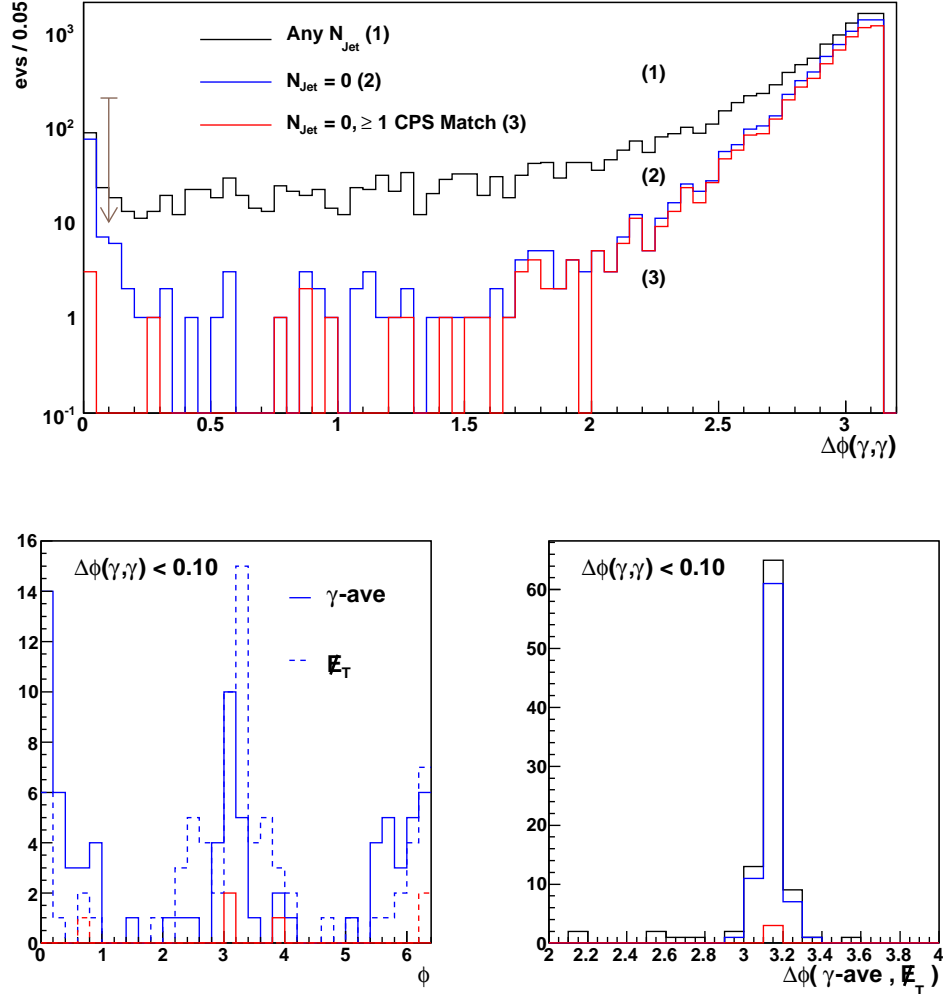


Figure 6.8: The distribution of $\Delta\phi(\gamma, \gamma)$ (top). Histogram (1) shows the distribution for events with any number of jets, while the histogram (2) shows the distribution after restricting to events with no jets. The CPS match requirement is applied in histogram (3). The region to the left of the arrow is studied in the bottom plots. In the bottom left plot, the average of the ϕ coordinate of the two photons (solid), and the ϕ of the \cancel{E}_T (dashed), are shown for events with $N_{\text{jet}} = 0$ before and after the CPS match requirement. The bottom right plot shows the difference, $\Delta\phi(\gamma_{\text{ave}}, \cancel{E}_T)$, for the three stages of selection depicted in the top figure. Selected events are required to satisfy $\Delta\phi(\text{EM}, \text{EM}) > 0.1$, as shown by the arrow in the top plot.

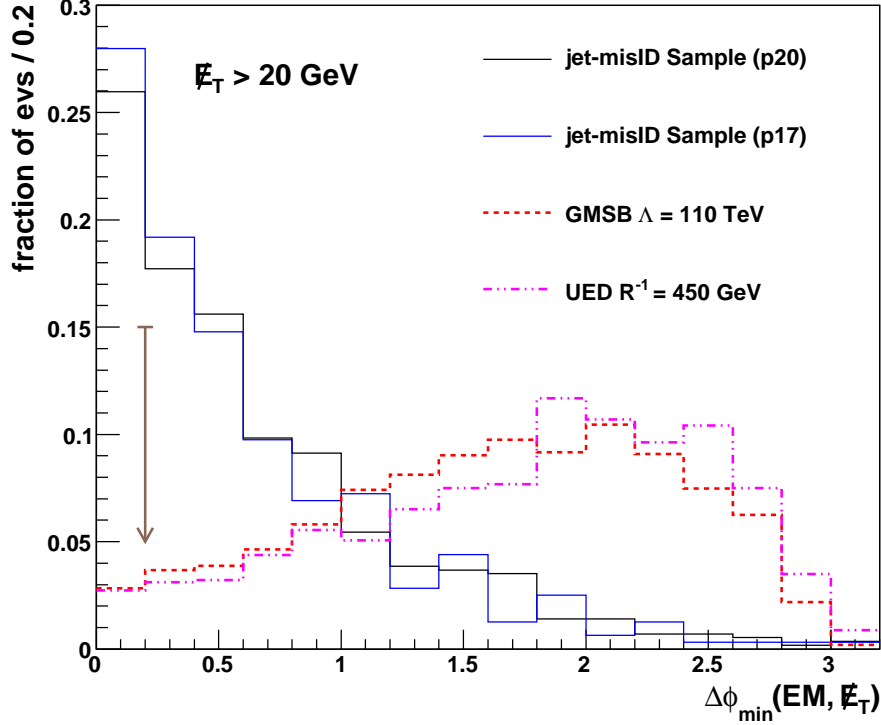


Figure 6.9: The distribution of $\Delta\phi$ between \cancel{E}_T and the EM cluster that yields the smaller $\Delta\phi$ value for p17 and p20 jet misID sample events with $\cancel{E}_T > 20$ GeV. The distribution in signal events for two model points is also shown. Selected events are required to satisfy $\Delta\phi_{\min}(\text{EM}, \cancel{E}_T) > 0.2$, as indicated by the arrow.

figure illustrates the tendency for alignment between \cancel{E}_T and one of the two EM clusters. In general, \cancel{E}_T is more often aligned with the trailing EM cluster and antialigned with the leading EM cluster. The interpretation is that \cancel{E}_T is mismeasured as a result of hadronic shower fluctuations of jets that fake photon candidates. For example, \cancel{E}_T could be aligned with a fake photon from the jet in a γ +jet event.

Figure 6.9 reveals that both EM clusters in signal events are more likely to be antialigned with \cancel{E}_T than aligned. $\Delta\phi_{\min}(\text{EM}, \cancel{E}_T)$ is therefore a good discriminating variable, and a $\Delta\phi_{\min}(\text{EM}, \cancel{E}_T) > 0.2$ requirement is made. The efficiency of this requirement in signal events is $\sim 96\%$.

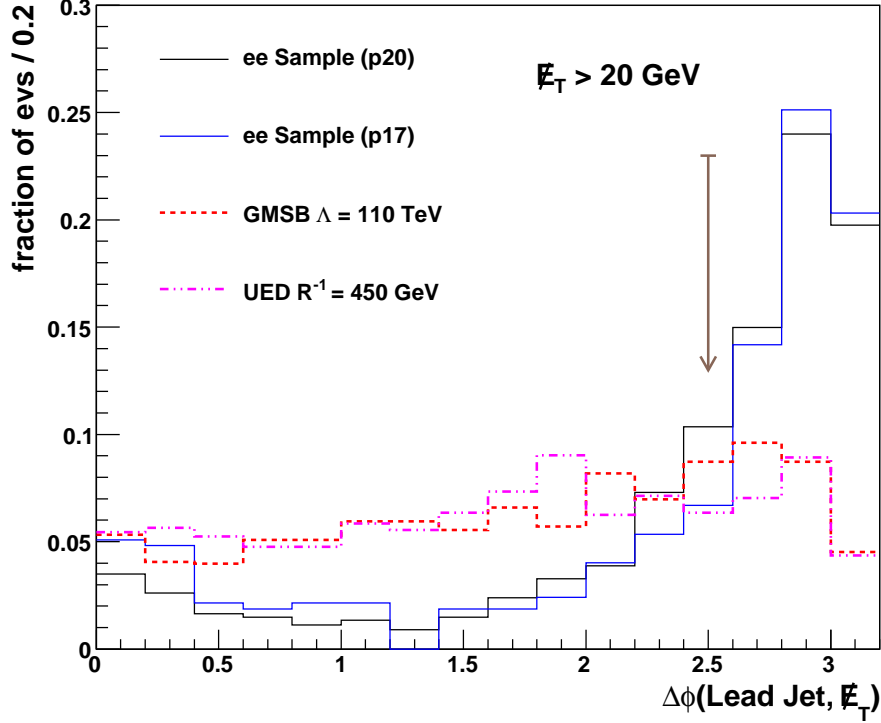


Figure 6.10: The distribution of $\Delta\phi$ between \cancel{E}_T and the leading jet in the event, if present, for p17 and p20 ee data sample events with $\cancel{E}_T > 20$ GeV. The distribution in signal events for two model points is also shown. Selected events are required to satisfy $\Delta\phi(\text{Lead Jet}, \cancel{E}_T) < 2.5$, as indicated by the arrow.

6.6.3 $\Delta\phi(\text{Leading Jet}, \cancel{E}_T)$

A jet is present in approximately 20% of events in each diEM subsample. However, approximately 80% of events with $\cancel{E}_T > 20$ GeV have at least one jet. Figure 6.10 illustrates the tendency for \cancel{E}_T to be antialigned with the leading jet in ee sample events with one or more jets and \cancel{E}_T values larger than 20 GeV. The antialignment is understood as a result of the jet energy resolution and the decrease of the jet p_T spectrum with increasing p_T . For a given narrow interval $p_T \pm \delta p_T$ in the true jet p_T , the jet energy resolution will result in a roughly equal number of jets leaving the interval on either side, but more jets will be entering from below than above. Slight antialignment is also observed between \cancel{E}_T and the

second leading jet, though it is not as prominent as for the leading jet.

In order to reduce the impact of instrumental \cancel{E}_T resulting from jet mismeasurements, a $\Delta\phi(\text{Leading Jet}, \cancel{E}_T) < 2.5$ requirement is made if a jet is present in the event. The efficiency of this requirement in signal events is $\sim 75 - 80\%$, depending on the model point.

6.7 Selection Efficiency for Signal Events

The efficiency for MC signal events to pass the selection criteria is now considered. For ease of comparison, two GMSB points and two UED points are treated in detail. The GMSB $\Lambda = 90$ TeV point is near the exclusion limit set in Reference [12], and will serve as a low scale reference point. As we will see, the GMSB $\Lambda = 130$ TeV point is slightly beyond the reach of this analysis, and thus will represent a high scale reference point. The $R_c^{-1} = 400$ GeV and $R_c^{-1} = 500$ GeV UED points are comparable in terms of cross section to the respective GMSB points.

Every GMSB or UED event that is produced yields, at the end of cascade decays, two χ_1^0 particles or two γ^* particles, respectively. In GMSB, the χ_1^0 decays to $\chi_1^0 \rightarrow \gamma \tilde{G}$ with a 98.2% branching ratio at $\Lambda = 90$ TeV, and a 89.8% branching ratio at $\Lambda = 130$ TeV, as recorded from the SUSY-HIT decay table (the additional decay mode which opens up with increasing values of Λ is $\chi_1^0 \rightarrow Z \tilde{G}$). In contrast, every γ^* in KK-parity violating UED decays via $\gamma^* \rightarrow \gamma G$.

For the signal efficiency studies presented here, the daughter photons of χ_1^0 / γ^* decays were located in the MC truth record. The proportion of 2, 1, and 0 signal photon events was found to be in good agreement with that expected from the branching ratios discussed above. The fraction of signal diphoton events is given in the first row of Table 6.7 for each signal point. The z-positions of the production vertex of these signal photons were verified to agree and used to define a truth primary vertex. The efficiency that the reconstructed primary vertex and truth vertex agree within $|\Delta Z| < 0.5$ cm is $\sim 99\%$ and listed in the second row of Table 6.7.

Reconstructed EM clusters were searched for within $\Delta R < 0.1$ about the truth signal photons, satisfying $E_T > 15$ GeV and located in either the CC ($|\eta_{det}| < 1.1$) or EC ($1.5 <$

| | GMSB $\Lambda = 90 \text{ TeV}$ | UED $R^{-1} = 400 \text{ GeV}$ | GMSB $\Lambda = 130 \text{ TeV}$ | UED $R^{-1} = 500 \text{ GeV}$ |
|---|------------------------------------|-----------------------------------|-------------------------------------|-----------------------------------|
| $\gamma\gamma$ Signal | 96.5 | 100 | 80.6 | 100 |
| PV Match | 98.4 | 99.4 | 98.7 | 99.3 |
| γ_1 Match | 83.5 | 83.7 | 85.1 | 85.4 |
| γ_2 Match | 71.1 | 70.2 | 74.7 | 72.1 |
| γ_1 Acc | 94.7 | 95.0 | 96.3 | 96.1 |
| γ_2 Acc | 77.3 | 78.2 | 80.7 | 79.3 |
| γ_1 Eff | 76.6 | 77.5 | 77.0 | 77.8 |
| γ_2 Eff | 75.5 | 77.9 | 76.3 | 77.0 |
| CPS-PV | 85.6 | 85.9 | 86.0 | 87.1 |
| $\Delta\phi(\gamma, \gamma)$ | 98.6 | 98.4 | 98.1 | 98.2 |
| $\Delta\phi_{\min}(\gamma, \cancel{E}_T)$ | 95.5 | 96.7 | 95.6 | 96.3 |
| $\Delta\phi(\text{Lead Jet}, \cancel{E}_T)$ | 80.4 | 79.9 | 78.0 | 76.3 |
| Cumulative (Matched) | 15.5 ± 0.3 | 17.1 ± 0.3 | 14.6 ± 0.3 | 17.6 ± 0.3 |
| Total Efficiency | 16.8 ± 0.3 | 17.5 ± 0.3 | 16.5 ± 0.3 | 18.5 ± 0.3 |

Table 6.7: Event selection efficiencies (%) for example signal model MC points. As discussed in more detail in the text, the efficiency at each stage in the truth match study is listed, followed by the cumulative efficiency. The total efficiency for events to pass the selection criteria, evaluated without truth matching, is listed in the final line. The uncertainties shown in the final two lines are statistical and determined by the MC sample size.

$|\eta_{det}| < 2.5$) calorimeter regions. The efficiency of such a match is given in the third row of the table for the leading truth photon and the fourth row for the trailing truth photon. The solid histograms of Figure 6.11 show, for the GMSB $\Lambda = 90$ TeV point, the η_{det} and E_T distributions of the reconstructed EM clusters matched to the leading and trailing truth signal photons. The primary source of efficiency loss with respect to truth at this stage is in the ICR region. After the matching requirements, $\sim 80\%$ of events have both photons located in the CC region (CC-CC), $\sim 20\%$ have one CC and one EC photon (CC-EC), and $\sim 1\%$ have two EC photons (EC-EC). A modest fraction of signal events are in the CC-EC region. However, the rate of fake photon candidates from jets increases in the forward region, and the ability to suppress fake photons from electrons in $W \rightarrow e\nu$ events is greatly diminished as well, as the pointing confirmation is significantly less efficient, since a single CC photon must have a CPS match, as opposed to either one in the CC-CC case. Thus, the CC-CC region is the focus of this analysis.

The acceptance criteria of this analysis, $E_T > 25$ GeV and $|\eta_{det}| < 1.1$, are then applied to the truth matched clusters, yielding the dashed histograms in Figure 6.11. The acceptance efficiencies are given in the fifth and sixth rows of Table 6.7 and are dominated by the $|\eta_{det}|$ requirement. After the $|\eta_{det}| < 1.1$ requirement, the leading photon satisfies the E_T requirement with $\sim 100\%$ efficiency, while the trailing photon satisfies it with $\sim 95\%$ efficiency.

Next, the photon identification requirements are applied. The efficiency per photon is $\sim 76\%$, as shown in the seventh and eighth rows of the table. The breakdown of efficiencies for each non TrkVeto selection variable is EMfrac 98%, CaloIso 98%, TrkIso 92%, EM3w 98%, NN 96%, for a combined efficiency of 85%. The TrkVeto efficiency is $\sim 90\%$, with 93% for the TrkProb variable and 97% for HOR. The photon identification efficiency is a bit lower than in SM $\gamma\gamma$ MC, for example, as the TrkIso requirement is $\sim 5\%$ less efficient in the more active signal events. The photon NN uses TrkIso as an input, and a strong correlation is observed between photons with a high TrkIso value and a low NN value. After the TrkIso cut, however, the NN cut for signal MC events is only 2% less efficient than for SM $\gamma\gamma$ MC events.

The CPS-PV requirement efficiency, which includes both the CPS match and pointing

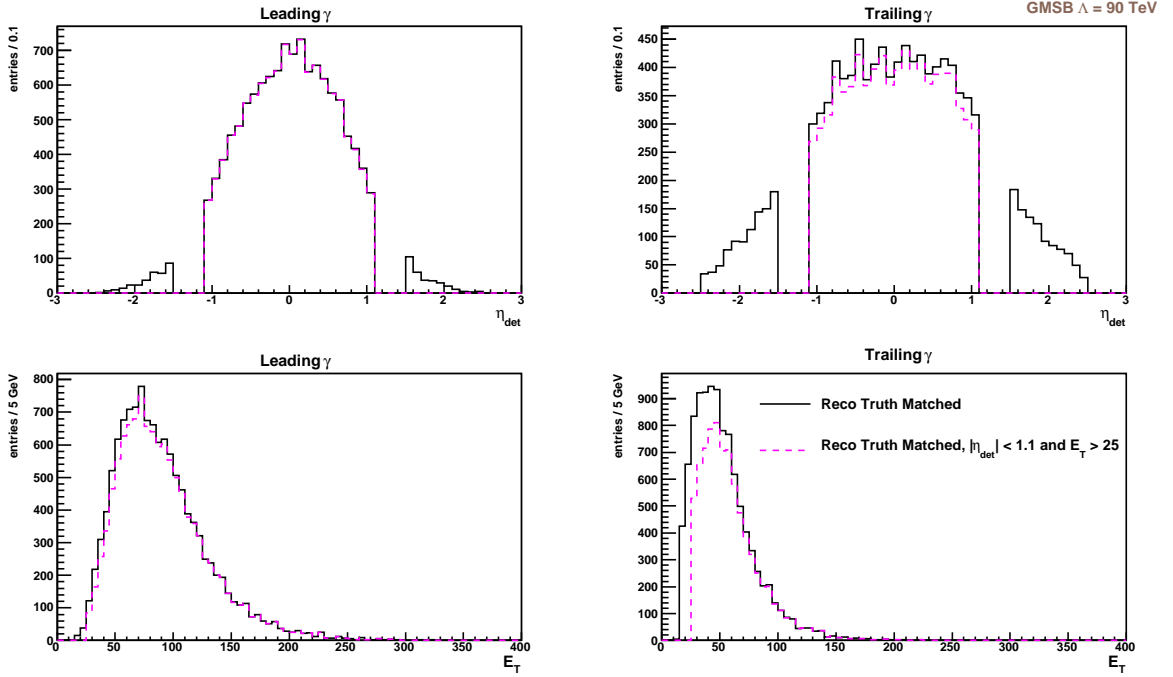


Figure 6.11: The η_{det} and E_T distribution for reconstructed EM clusters truth matched to leading (left) and trailing (right) signal photons in GMSB $\Lambda = 90$ TeV MC events. The distributions before (after) the acceptance requirements of this analysis are applied are shown as solid (dashed) histograms.

requirements, is listed next in Table 6.7. The efficiency is $\sim 92\%$ in MC and a 0.94 scale factor has been applied as previously discussed. Following the CPS-PV efficiencies in the table are the efficiencies for the three $\Delta\phi$ requirements described previously.

The cumulative efficiency after each stage in the truth match study is listed in the second to last row of Table 6.7. The total efficiency is given in the final row, evaluated by dividing the number events passing the selection criteria versus the total considered, without truth matching. The total efficiency is $\approx 17\%$ for GMSB, and $\approx 18-19\%$ for UED in the range of the respective energy scale parameter relevant for this analysis. For GMSB, an increase in total acceptance with Λ is offset by a decrease in the branching ratio to the $\gamma\gamma$ final state.

Normalized E_T distributions for the four signal model points considered in the truth study after all selection requirements are shown in Figure 6.12. The average E_T value in

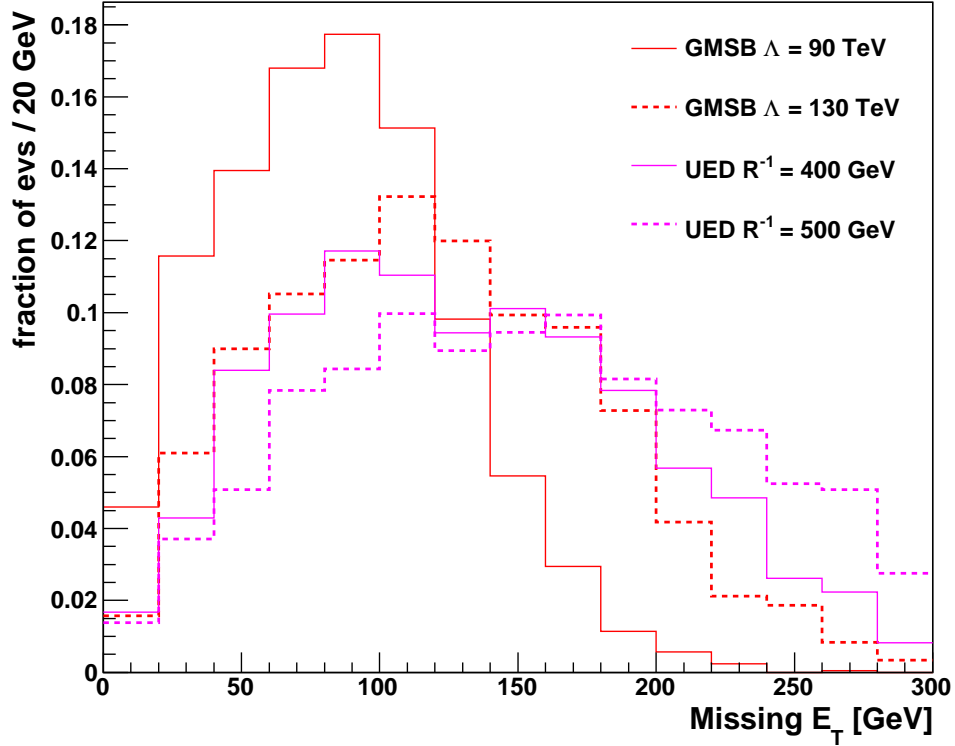


Figure 6.12: Normalized \cancel{E}_T distributions after all selection requirements for four example signal model points.

both signal models increases with the energy scale parameter. The dependence is more pronounced for the GMSB model than the UED model for respective Λ and R_c^{-1} values that yield cross sections in the range relevant for this analysis.

For reference, the distributions of several other kinematic variables are presented in Appendix A for example signal model points as well as for the $\gamma\gamma$ data sample and various data control samples.

Chapter 7

Background Estimation

SM backgrounds in the sample of candidate $\gamma\gamma$ events are broadly classified into two categories. The first category consists of events without genuine \cancel{E}_T , and the methods to model the different contributions in this category are described in Section 7.1. The second category consists of events with genuine \cancel{E}_T , and is treated in Section 7.2.

7.1 Background Processes with Instrumental \cancel{E}_T

The term *instrumental* \cancel{E}_T describes \cancel{E}_T that is induced in an otherwise E_T balanced event as a result of object mismeasurement, such as the E_T of a photon candidate or any jet which may be present in the event. The processes that contribute most significantly to this class of background are SM $\gamma\gamma$, γ +jet, and multi-jet processes. Representative Feynman diagrams for the SM $\gamma\gamma$ and γ +jet processes are shown in Figure 7.1(a) and (b), respectively. Events with at least one photon candidate originating from a misidentified jet, namely γ +jet and multi-jet events, are henceforth referred to as “jet misID” events. Sections 7.1.1 and 7.1.2 define the methods to model the \cancel{E}_T distribution shape in SM $\gamma\gamma$ and jet misID events, respectively, while Section 7.1.3 describes the procedure of normalizing these two distributions.

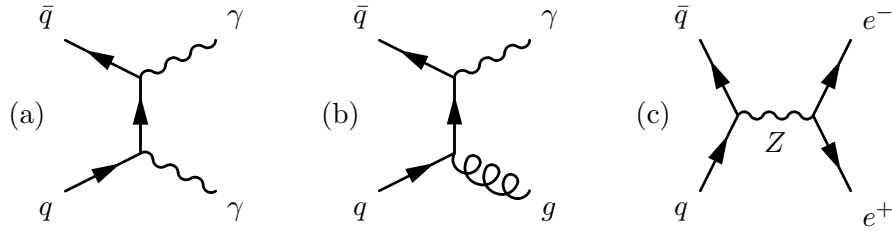


Figure 7.1: Representative LO Feynman diagrams contributing to the SM processes (a) $p\bar{p} \rightarrow \gamma\gamma$, (b) $p\bar{p} \rightarrow \gamma + \text{jet}$, and (c) $p\bar{p} \rightarrow e^+e^-$.

7.1.1 Modeling \cancel{E}_T in SM Diphoton Events

As instrumental \cancel{E}_T is ultimately a result of incorrect measurements of the objects in the event, the MC description of instrumental \cancel{E}_T should be regarded with caution. In particular, one does not expect the MC to model precisely the most dramatic mismeasurements, and hence the largest instrumental \cancel{E}_T values. Therefore, the \cancel{E}_T distribution in SM $\gamma\gamma$ events is primarily modeled with $Z \rightarrow ee$ data. The motivation to use the $Z \rightarrow ee$ process, depicted in Figure 7.1(c), to model the \cancel{E}_T distribution in SM $\gamma\gamma$ events derives from the expectation that the calorimeter response to two electrons should be roughly equivalent to the response to two photons, and any associated jet activity that modifies the calorimeter response to the diEM final state should likewise be similar. The kinematic properties of the processes differ, however, so a comparison of data and MC is performed to verify that using $Z \rightarrow ee$ data to model the \cancel{E}_T in SM $\gamma\gamma$ events is reasonable, and that kinematic differences between the two processes have negligible impact on the \cancel{E}_T distribution.

A sample of $Z \rightarrow ee$ events is selected from the ee data sample. The diEM invariant mass in ee data and $Z \rightarrow ee$ MC events is restricted to the interval $80 < m_{ee} < 100$ GeV about the Z boson mass peak, to select the $Z \rightarrow ee$ events while suppressing the presence of genuine \cancel{E}_T events in ee data, such as $W + \text{jet}$, diboson, and $t\bar{t}$ events. The left plot in Figure 7.2 shows the invariant mass in ee data before and after the requirement, and illustrates the large fraction of $Z \rightarrow ee$ events in the sample. The right plot shows the \cancel{E}_T distribution before and after the requirement. As expected, the requirement reduces the number of events with large \cancel{E}_T .

Next, several kinematic distributions are compared for ee sample data, $Z \rightarrow ee$ MC,

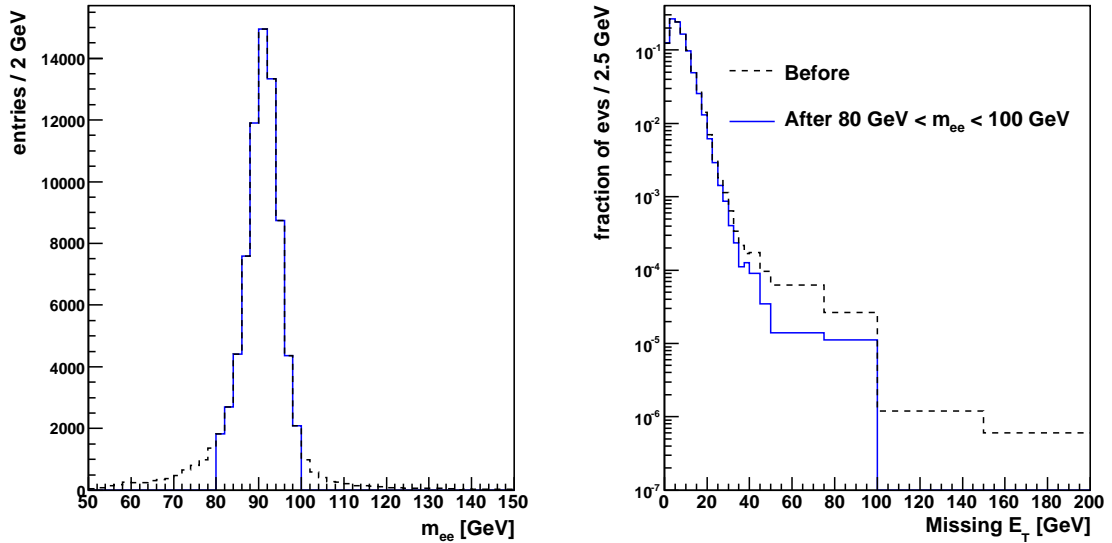


Figure 7.2: The invariant mass (left) and \cancel{E}_T (right) in the ee data sample before and after events are selected to be in an interval about the Z boson invariant mass peak.

and SM $\gamma\gamma$ MC. The sum of the E_T of the two EM clusters ($\sum E_T$) is shown in the left plot of Figure 7.3. The distribution is clearly peaked at the Z boson mass for the $Z \rightarrow ee$ process, while for SM $\gamma\gamma$ it decreases uniformly once beyond the value determined by the acceptance criteria. Despite the kinematic differences observed in the $\sum E_T$ distributions, the \cancel{E}_T response in the case when no reconstructed jets are present is very similar between the two processes, as shown in the right plot of Figure 7.3. Thus, the E_T dependence of the calorimeter resolution for EM clusters does not result in a significant difference in the \cancel{E}_T distribution for the two processes.

Jets are not measured on average as precisely as electrons and photons, so the presence of jets in the event appreciably modifies the \cancel{E}_T distribution in diEM final state events. Since this analysis allows for jets, the assumption that the $Z \rightarrow ee$ process continues to model well the SM $\gamma\gamma$ process in the presence of jets must be checked. Several kinematic variables characterizing the jet activity are studied. The top two plots in Figure 7.4 present the jet multiplicity (N_{jet}) and the magnitude of the vector sum of the transverse momenta of the photons (Q_T) for the two processes. The jet multiplicities are comparable. The variable Q_T

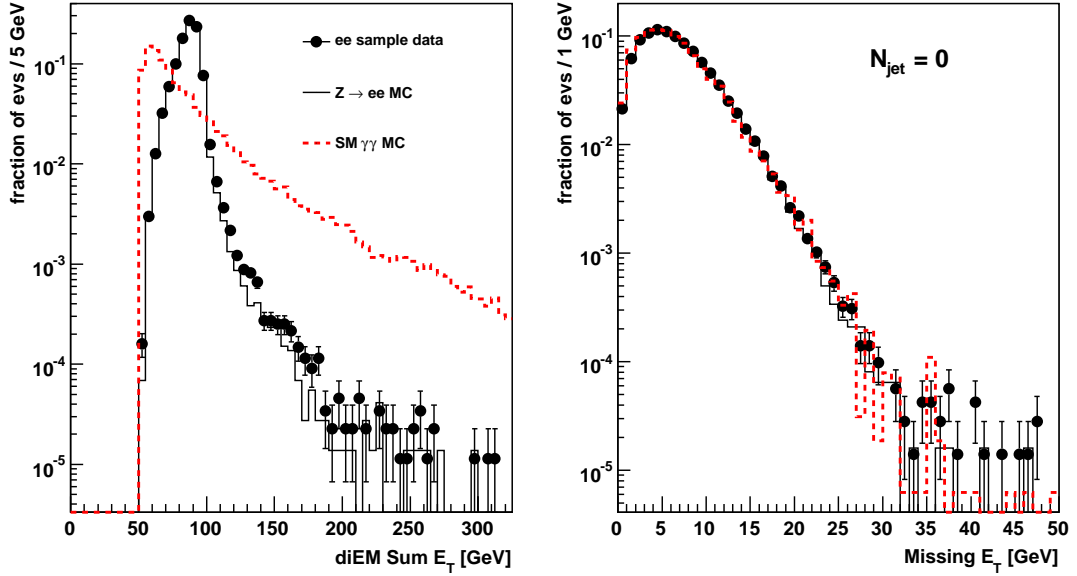


Figure 7.3: Normalized distributions of diEM $\sum E_T$ (left) and \cancel{E}_T in events with $N_{jet} = 0$ (right) for ee data, $Z \rightarrow ee$ MC, and SM $\gamma\gamma$ MC.

is a measure of the hadronic recoil to the diEM system, and the Q_T distributions are similar, though the SM $\gamma\gamma$ MC distribution is softer at large Q_T . The leading and second leading jet p_T distributions are shown in the middle of Figure 7.4, and are consistent with this observation. The bottom two plots of Figure 7.4 show the \cancel{E}_T distributions in the $N_{jet} = 1$ and $N_{jet} > 1$ cases. The \cancel{E}_T distribution of the two processes are similar in events with jets, though the SM $\gamma\gamma$ distribution is slightly softer at the highest values.

The \cancel{E}_T comparison is shown for all jet multiplicities in Figure 7.5. The agreement between ee data and $Z \rightarrow ee$ MC is good at low values of \cancel{E}_T , shown on a linear scale in the inlay. SM $\gamma\gamma$ MC also agrees well in this region, although it is slightly softer than ee data and $Z \rightarrow ee$ MC. At intermediate \cancel{E}_T values between 20 and 35 GeV, the agreement between ee data and $Z \rightarrow ee$ MC remains good, with SM $\gamma\gamma$ MC becoming noticeably softer. Not surprisingly, $Z \rightarrow ee$ MC no longer models ee data well beyond $\cancel{E}_T \approx 35$ GeV, as more instances of large mismeasurements are expected in ee data than are modeled in MC. However, residual genuine \cancel{E}_T contributions may also remain even after the ee invariant

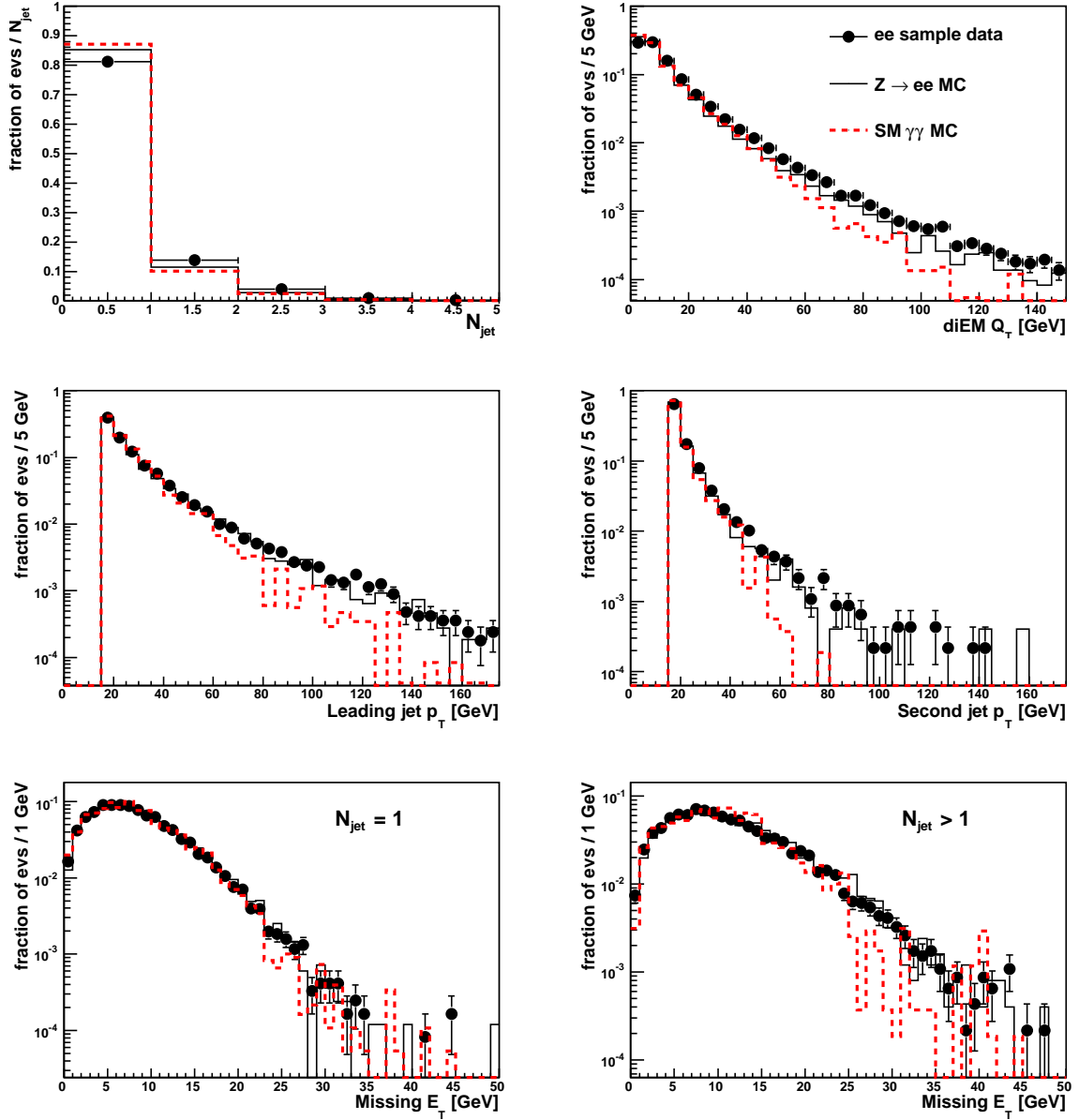


Figure 7.4: The top four plots display properties of the jet activity in ee data, $Z \rightarrow ee$ MC, and SM $\gamma\gamma$ MC. The bottom plots display the \cancel{E}_T distribution in events with one jet and with greater than one jet. Further details are described in the text.

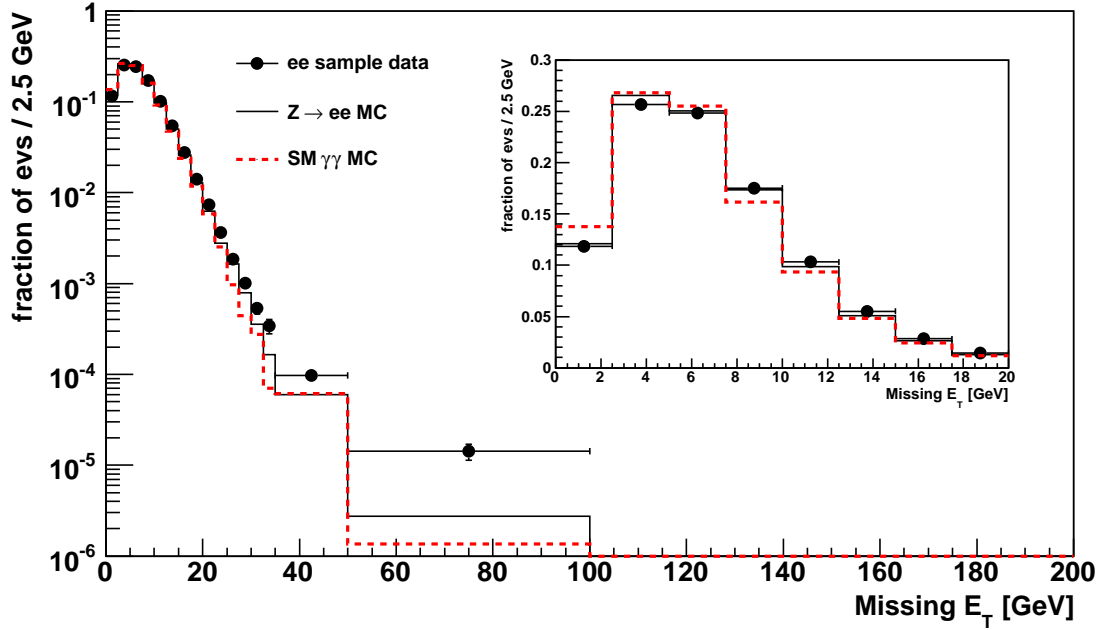


Figure 7.5: Comparison for all jet multiplicities of the \cancel{E}_T distribution in ee data, $Z \rightarrow ee$ MC, and SM $\gamma\gamma$ MC. The inlay shows the low \cancel{E}_T region on a linear scale.

mass is restricted to the Z boson peak region. As one extreme would be to use ee data, and the other to use SM $\gamma\gamma$ MC, we choose to model the \cancel{E}_T distribution in $\gamma\gamma$ events for $\cancel{E}_T > 20$ GeV with the average of the two distributions, and refer to this as the “corrected ee distribution”. The two extremes are used later to assign a systematic uncertainty.

The comparisons thus far have been between p20 data and MC. Figure 7.6 provides a comparison of normalized \cancel{E}_T distributions for p17 and p20 ee data. The two distributions are similar, though the \cancel{E}_T distribution is noticeably harder in p20 data, which has been collected at higher instantaneous luminosity. Figure 7.7 shows the \cancel{E}_T distribution in the p17 and p20 ee samples in three intervals of instantaneous luminosity. The luminosity profiles are shown in the bottom right of the figure. The difference in the \cancel{E}_T shape for p17 and p20 ee data reflects a dependence on the instantaneous luminosity. As the instantaneous luminosity increases, the number of $p\bar{p}$ interactions per event increases, resulting in a corresponding increase in the unclustered energy of the event and a degradation of the \cancel{E}_T resolution.

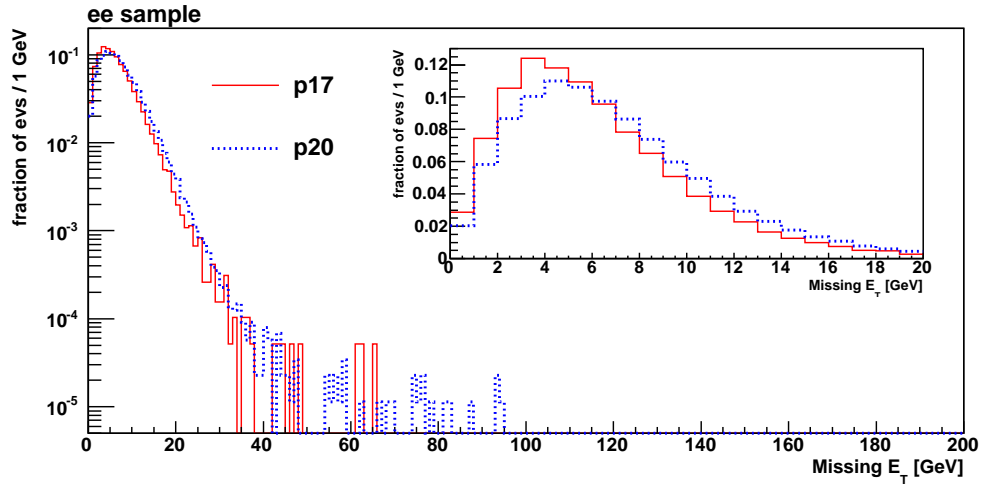


Figure 7.6: Normalized \cancel{E}_T distributions in the p17 and p20 ee data samples. The inlay shows the low \cancel{E}_T region on a linear scale.

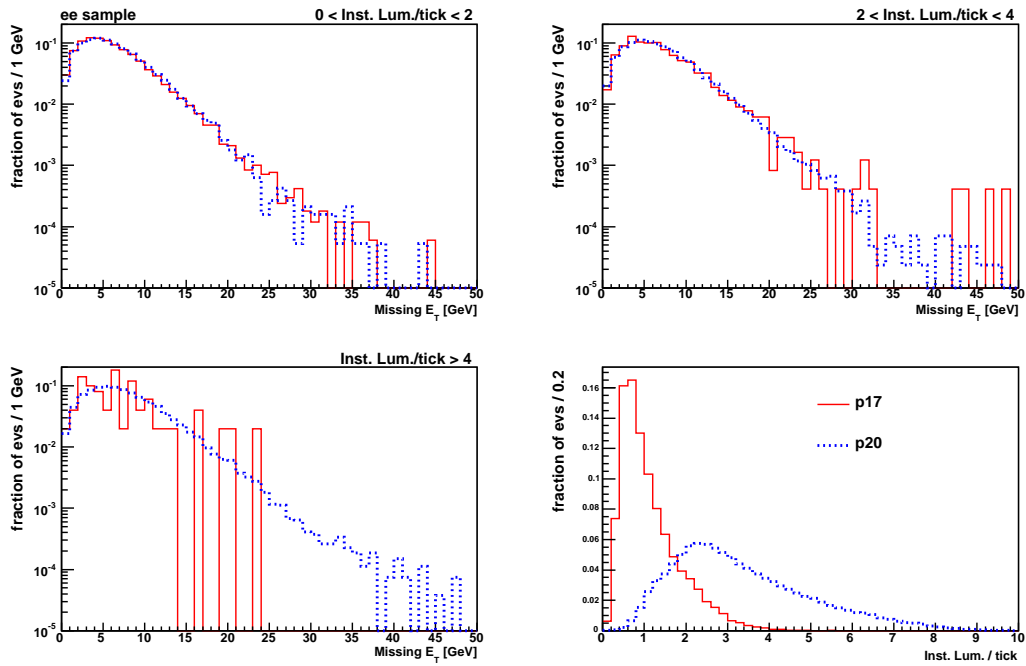


Figure 7.7: The p17 and p20 ee sample \cancel{E}_T distributions are plotted for three instantaneous luminosity intervals, where one unit of “Inst. Lum./tick” corresponds to $36 \times 10^{30} \text{ cm}^{-2}\text{s}^{-1}$. Luminosity profiles are shown for the two run periods in the bottom right plot.

7.1.2 Modeling \cancel{E}_T in SM Events with Jets Misidentified as Photons

In order to pass the photon identification requirements, the candidate EM cluster must have a high EM fraction, and be well isolated from other calorimeter energy depositions and nearby tracks. Those jets which pass this selection usually contain a leading neutral meson decaying to two highly collinear photons, such as $\pi^0 \rightarrow \gamma\gamma$, and very little additional visible activity. The calorimeter response to events with one or more fake photons is nonetheless different than the \cancel{E}_T response to real diEM events.

The jet misID sample was defined in Section 6.4. The main feature that distinguishes this sample from the candidate $\gamma\gamma$ sample is that at least one of the photon candidates is required to fail the NN criteria, which is $\approx 98\%$ efficient for real photons. A sizable uncertainty on the SM prediction for the \cancel{E}_T distribution in $\gamma\gamma$ events in the signal sensitive $\cancel{E}_T > 50$ GeV region arises from the statistical uncertainty on the jet misID contribution. The EM selection criteria for the jet misID sample is therefore relaxed to IsEM-L, as was defined in Table 6.4.

The relaxation of the jet misID sample is performed in stages to assess whether the change in selection criteria introduces a bias in the shape of the \cancel{E}_T distribution. Table 7.1 lists the different IsEM-L definitions considered. Definition A is the same as IsEM-T, while EM3w is loosened in two steps in Definitions B and C, and TrkIso is loosened in three steps in Definitions D, E, and F. Figure 7.8 depicts the increase in the number of events versus the progressively looser definitions. The normalized \cancel{E}_T distribution for each definition is shown in Figures 7.9 and 7.10 for p17 and p20 data, respectively. The figure inlays show the low \cancel{E}_T region on a linear scale, and the subfigures show the bin by bin pull of the given definition with respect to Definition A. The pull is the difference between the two distributions in a given bin after the two distributions have been normalized, divided by the total uncertainty. The pull distributions demonstrate that, within the statistical uncertainties, the relaxation procedure does not appreciably bias the shape of the \cancel{E}_T distribution, while significantly increasing the jet misID sample sizes. A systematic uncertainty on the shape of the jet misID \cancel{E}_T distribution is evaluated by examining the variation of the background prediction on the ISEM-L definition used.

Figure 7.11 compares normalized \cancel{E}_T distributions (IsEM-L) in p17 and p20 jet misID

| Selection | Definition | | | | | |
|-------------------------|------------|------|------|------|------|-----------|
| | A(IsEM-T) | B | C | D | E | F(IsEM-L) |
| EM3w (cm ²) | 14 (18) | 50 | 100 | 100 | 100 | 100 |
| TrkIso (GeV) | 2.00 | 2.00 | 2.00 | 2.50 | 3.75 | 5.00 |

Table 7.1: Different definitions which are considered in the relaxation of the jet misID sample. A number in parentheses indicates a p20 value if different than in p17.

data, and demonstrated that the p20 distribution is noticeably harder than the p17 distribution. Figure 7.12 shows the \cancel{E}_T distributions in three intervals of the instantaneous luminosity. As in the case of ee sample data, the difference in shape is attributed to the increased number of $p\bar{p}$ interactions per event in higher luminosity data, and the corresponding decrease in \cancel{E}_T resolution.

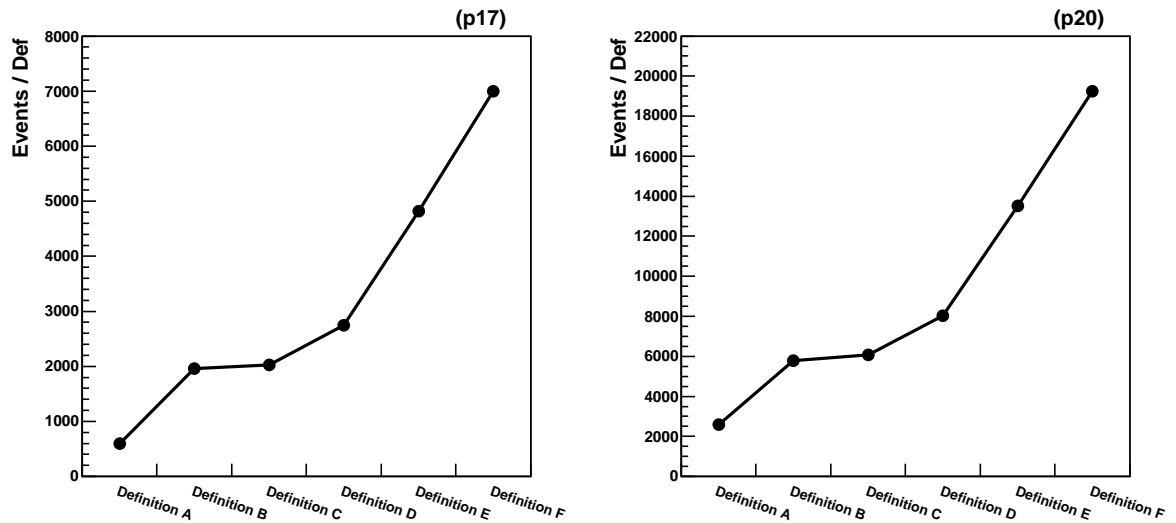


Figure 7.8: The total number of jet misID sample events in p17 (left) and p20 (right) as a function of the IsEM-L definitions listed in Table 7.1.

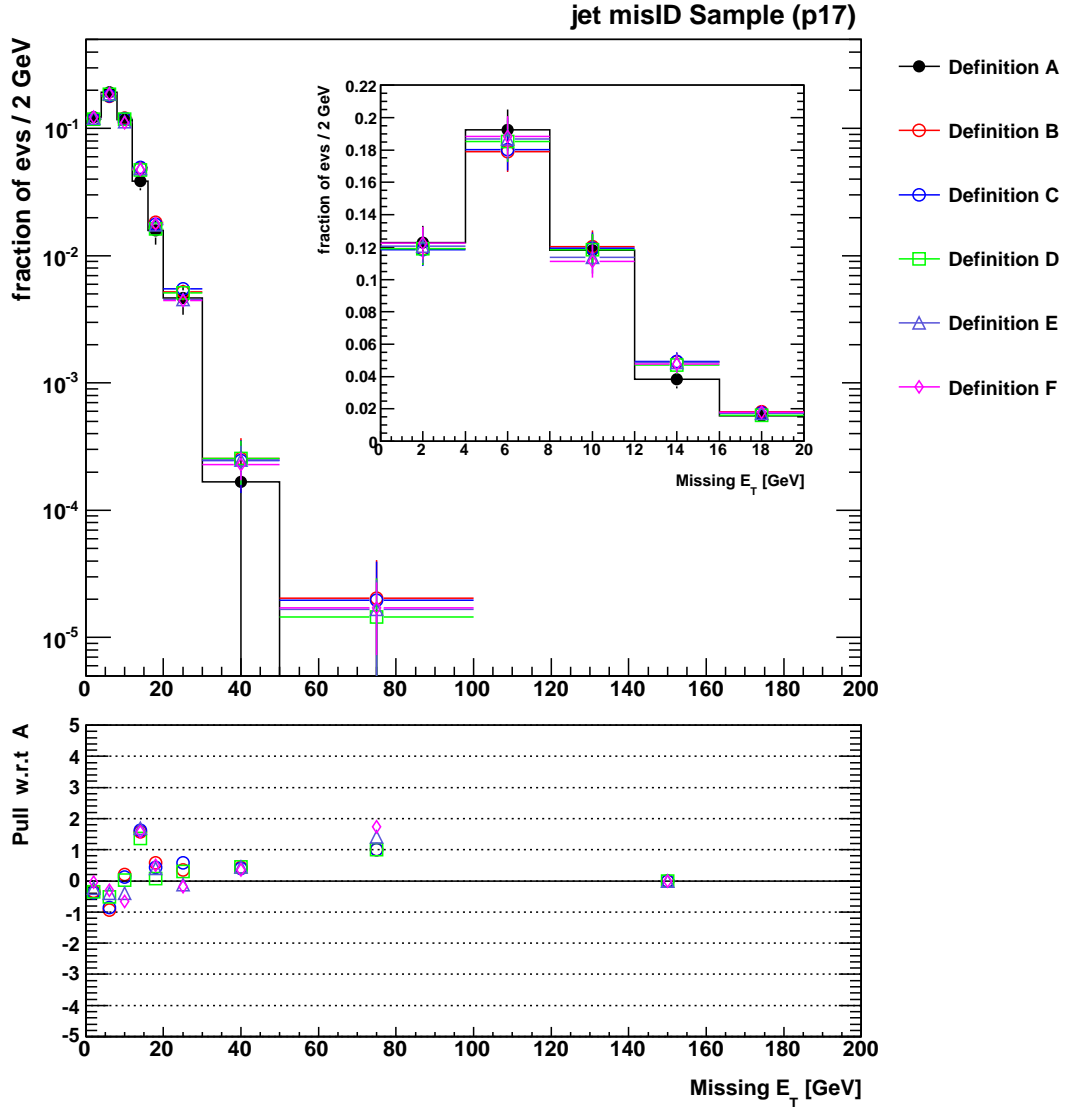


Figure 7.9: Effect on the \cancel{E}_T distribution as the p17 jet misID sample is relaxed according to the definitions in Table 7.1. The inset shows low \cancel{E}_T bins on a linear scale and, and the bottom figure shows the pull of the progressively looser definitions with respect to A.

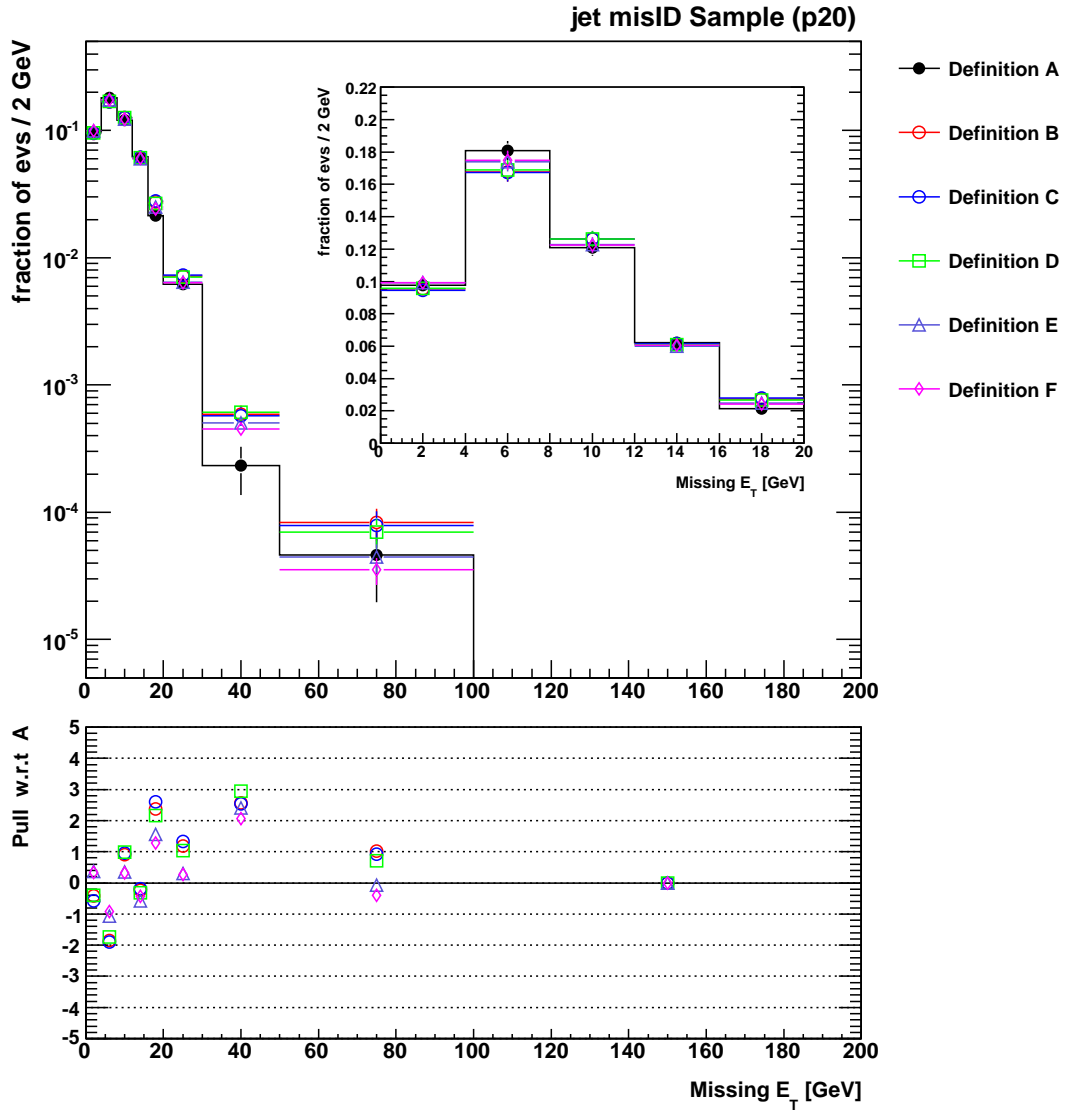


Figure 7.10: As described in the caption for Figure 7.9, but for p20 jet misID sample data.

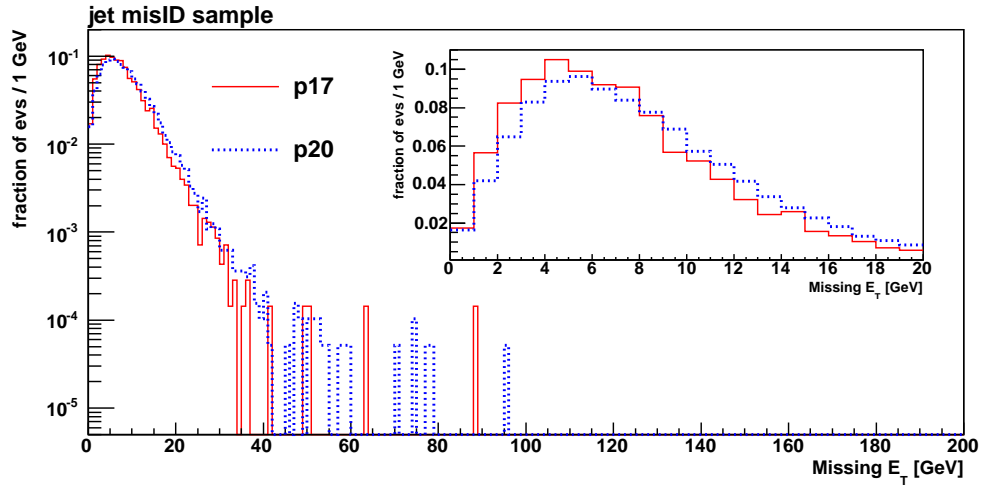


Figure 7.11: Normalized \cancel{E}_T distributions in the p17 and p20 jet misID samples. The inlay shows the low \cancel{E}_T region on a linear scale.

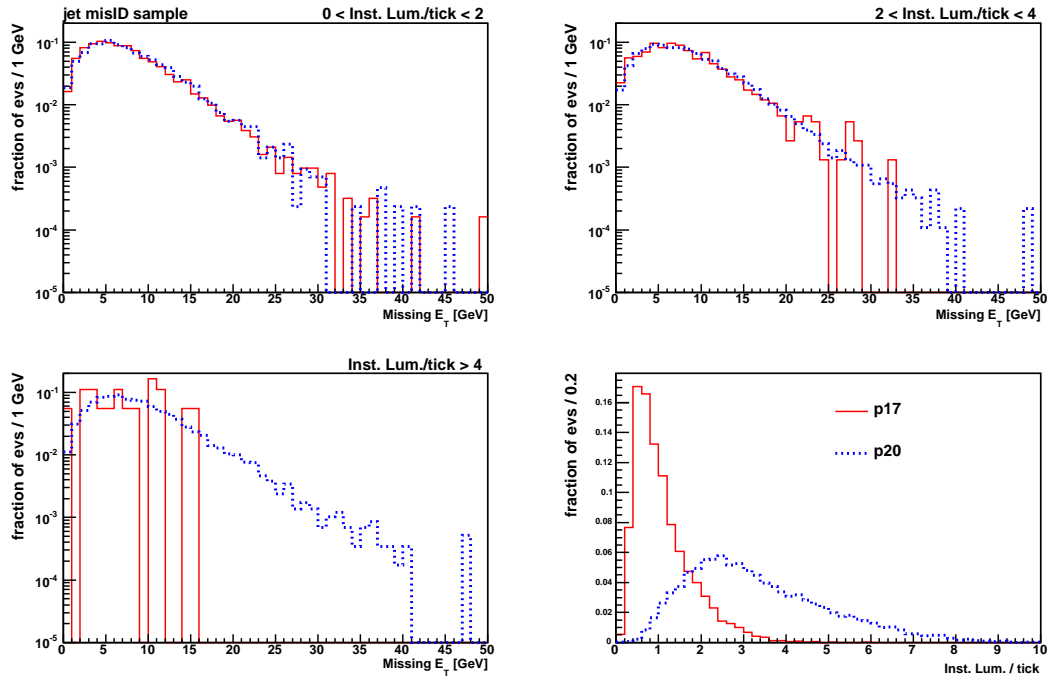


Figure 7.12: The p17 and p20 jet misID sample \cancel{E}_T distributions separated in three intervals of instantaneous luminosity (1 Inst. Lum./tick corresponds to $36 \times 10^{30} \text{ cm}^{-2} \text{ s}^{-1}$). Luminosity profiles are shown for the two run periods in the bottom right plot.

7.1.3 Normalization of the Instrumental \cancel{E}_T Contributions

The background prediction from instrumental \cancel{E}_T sources is normalized such that the number of events with $\cancel{E}_T < 10$ GeV is equal to that in the candidate $\gamma\gamma$ sample. Genuine \cancel{E}_T sources are therefore assumed to be negligible in this region. The validity of this assumption is demonstrated in Section 7.2.

The previously described corrected ee and jet misID \cancel{E}_T distributions are shown unit normalized and overlaid for shape comparison in Figure 7.13. The shapes are different, and the relative normalization of the two instrumental \cancel{E}_T components is determined by a fit to $\gamma\gamma$ sample data between 0 and 20 GeV. Let $N_{\gamma\gamma}^i$ denote the number of $\gamma\gamma$ sample events in the i^{th} bin of the \cancel{E}_T distribution. Similarly, let N_{ee}^i and $N_{jet\ misID}^i$ denote the corresponding number of events in the ee and jet misID distributions. Finally, let $N_{\gamma\gamma}^{10}$, N_{ee}^{10} , and $N_{jet\ misID}^{10}$ denote the number of events in each sample with $\cancel{E}_T < 10$ GeV. The predicted number of $\gamma\gamma$ events from instrumental \cancel{E}_T sources in the i^{th} bin is expressed as

$$\text{Pred}^i = p \left(\frac{N_{\gamma\gamma}^{10}}{N_{ee}^{10}} \right) N_{ee}^i + (1 - p) \left(\frac{N_{\gamma\gamma}^{10}}{N_{jet\ misID}^{10}} \right) N_{jet\ misID}^i . \quad (7.1)$$

One can easily verify that

$$\sum_{\cancel{E}_T < 10 \text{ GeV}} \text{Pred} = \sum_{\cancel{E}_T < 10 \text{ GeV}} N_{\gamma\gamma} . \quad (7.2)$$

The parameter p is a relative normalization factor and can be interpreted in terms of the purity of the $\gamma\gamma$ sample. The value of p is determined by a fit to the $\gamma\gamma$ sample \cancel{E}_T distribution between 0 and 20 GeV (corresponding to nBins, with nBins = 8 for the chosen bin width of 2.5 GeV). The fit minimizes the following χ^2 distribution,

$$\frac{\chi^2}{\text{nDoF}}(p) = \frac{1}{\text{nBins} - 1} \sum_{i=1}^{\text{nBins}} \frac{(\text{Data}^i - \text{Pred}^i(p))^2}{\sigma_{\text{Data}^i}^2 + \sigma(p)_{\text{Pred}^i}^2} . \quad (7.3)$$

The number of degrees of freedom is nDoF = nBins - 1, as Equation 7.2 represents a constraint. The uncertainties σ_{Data^i} and $\sigma(p)_{\text{Pred}^i}$ are statistical, and $\sigma(p)_{\text{Pred}^i}$ is derived from Equation 7.1.

The $\gamma\gamma$ sample \cancel{E}_T distribution is shown for the fit region in the inlay of Figure 7.14. The predicted SM $\gamma\gamma$ and jet misID contributions, determined from the first and second

terms in Equation 7.1, respectively, are displayed stacked according to the best estimate of the purity, p_0 . Figure 7.15 shows the χ^2/nDoF as a function of p for p17 and p20 data. The values of p where the minima are achieved are interpreted as the best estimates. The uncertainty on p_0 , $\pm\delta p$, is obtained from the purity values about the minima where the χ^2/nDoF has increased by 1 unit. The values are determined to be

$$p_0 \pm \delta p = \begin{cases} 0.34^{+0.29}_{-0.31} & (\text{p17}) \\ 0.46^{+0.15}_{-0.16} & (\text{p20}) \end{cases}, \quad (7.4)$$

and are consistent with each other within the uncertainties. Figure 7.16 displays the pull, data minus prediction over the combined uncertainty, for each bin used in the fit. The prediction is evaluated for p_0 and $p_0 \pm \delta p$, and the pull values indicate that the fits are well behaved and the definition of δp is reasonable.

Several studies were performed to check the validity of the fit result. For example, the fit was studied as a function of the number of bins used between 0 and 20 GeV. The minimum of the $\chi^2/\text{nDoF}(p)$ was stable for the number of bins ranging from four to twenty, though the uncertainty in p_0 increased as more bins were included. The fit was also performed using SM $\gamma\gamma$ MC instead of ee data, with the results of these fits being well within the uncertainties of those obtained with ee data. The small genuine \cancel{E}_T background component, determined in the next section, was added as an additional term, independent of p , to Equation 7.1. As expected, this term has a negligible impact on the fit result. Lastly, the fit was verified to be insensitive to signal contributions for model cross section values relevant to this analysis.

Figure 7.17 is similar to Figure 7.14 but shows only the total instrumental background prediction. The $\gamma\gamma$ sample data used in the fit is again displayed with the prediction in the inlay of the figure. As the prediction is in good agreement with $\gamma\gamma$ sample data in the low \cancel{E}_T region, the prediction is extrapolated to higher \cancel{E}_T values shown in the main plot of the figure. The impact on the extrapolation from the uncertainty on the fitted value of p is shown as the shaded region, representing the $\pm 1\sigma$ uncertainty obtained by varying the purity by $\pm\delta p$ about the central p_0 value. The impact is small and treated as a systematic uncertainty.

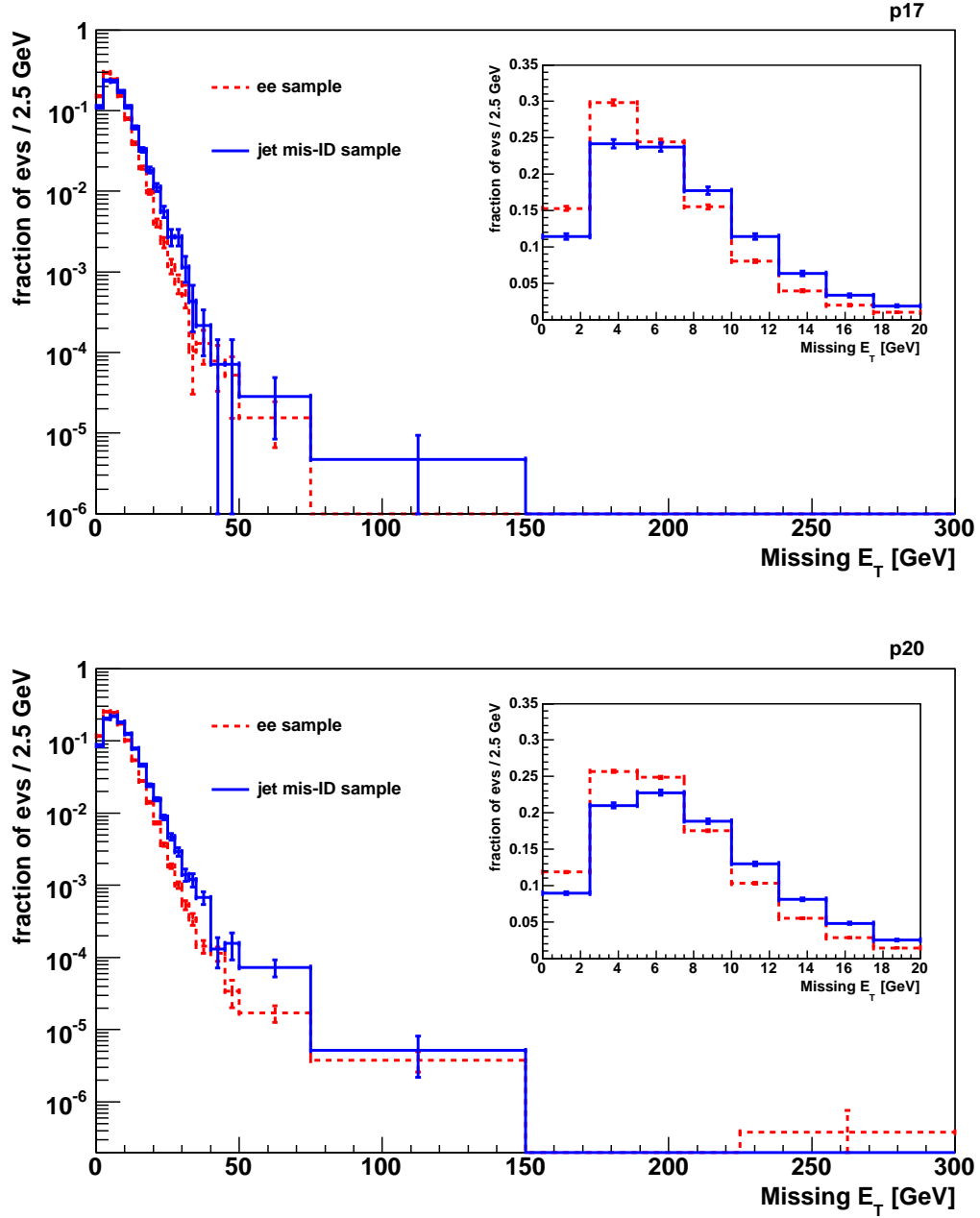


Figure 7.13: Unit normalized \cancel{E}_T distributions in p17 (top) and p20 (bottom) corrected ee and jet misID data that are used to model the instrumental backgrounds in the $\gamma\gamma$ sample. The uncertainties shown are statistical. The inlays show the $\cancel{E}_T < 20$ GeV region on a linear scale where the fit described in the text is performed.

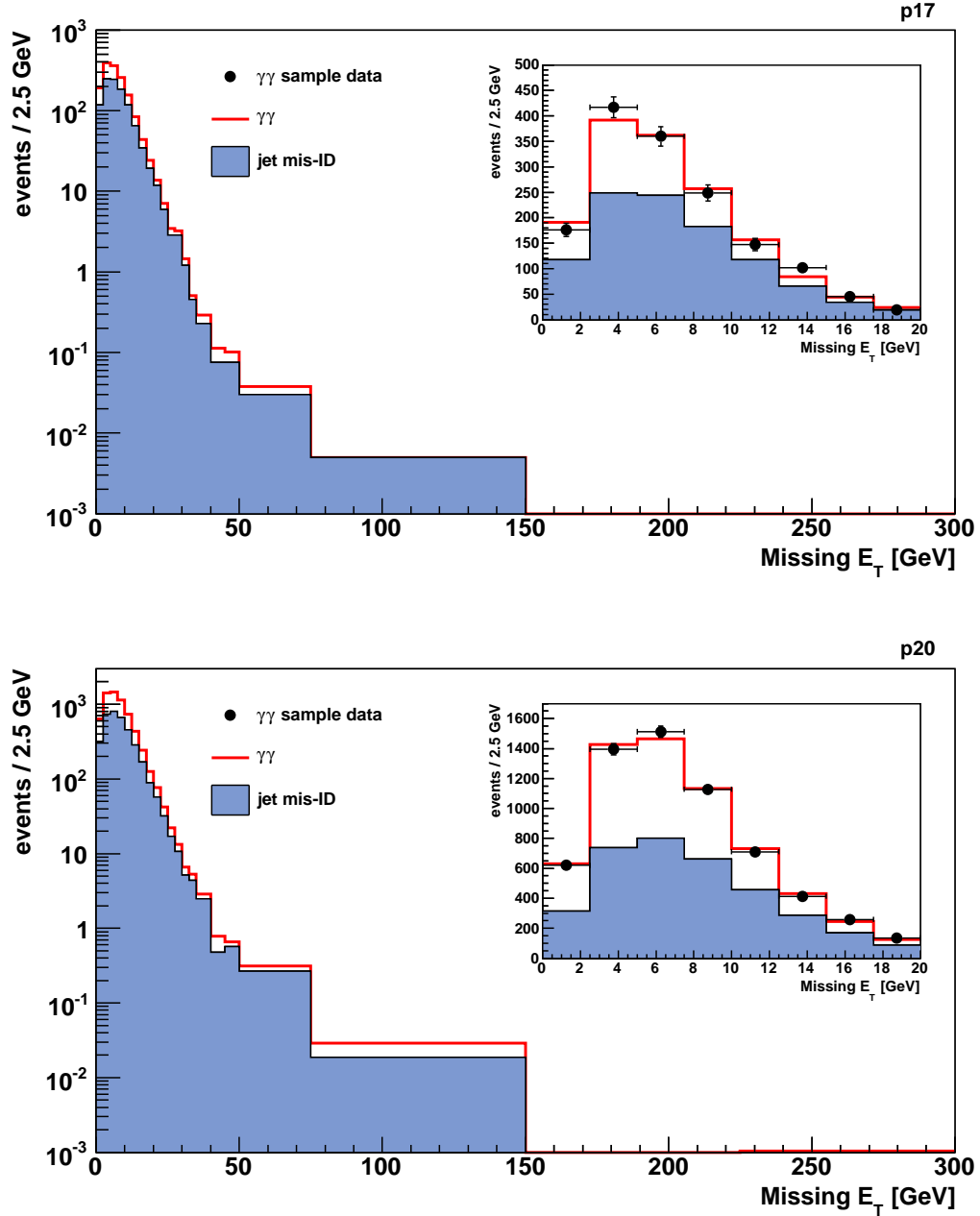


Figure 7.14: The predicted \cancel{E}_T distribution from instrumental backgrounds for p17 (top) and p20 (bottom). The $\gamma\gamma$ sample data used in the fit is shown in the inlay on a linear scale, and the corrected ee and jet misID distributions are combined according to the equation and fit results described in the text.

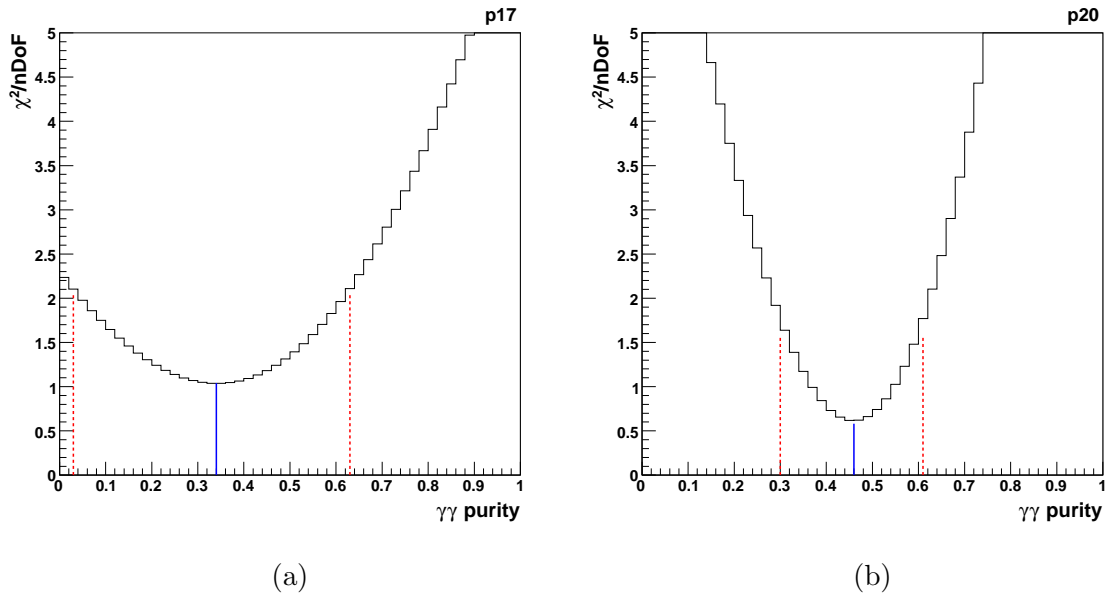


Figure 7.15: The $\chi^2/n\text{DoF}$ of the instrumental \cancel{E}_T prediction fit to p17 (a) and p20 (b) $\gamma\gamma$ sample data. The purity values denoted with a solid line are used in the instrumental \cancel{E}_T prediction (p_0), while the values denoted by dashed lines ($\pm\delta p$) are used in assessing the systematic uncertainty associated with the purity determination.

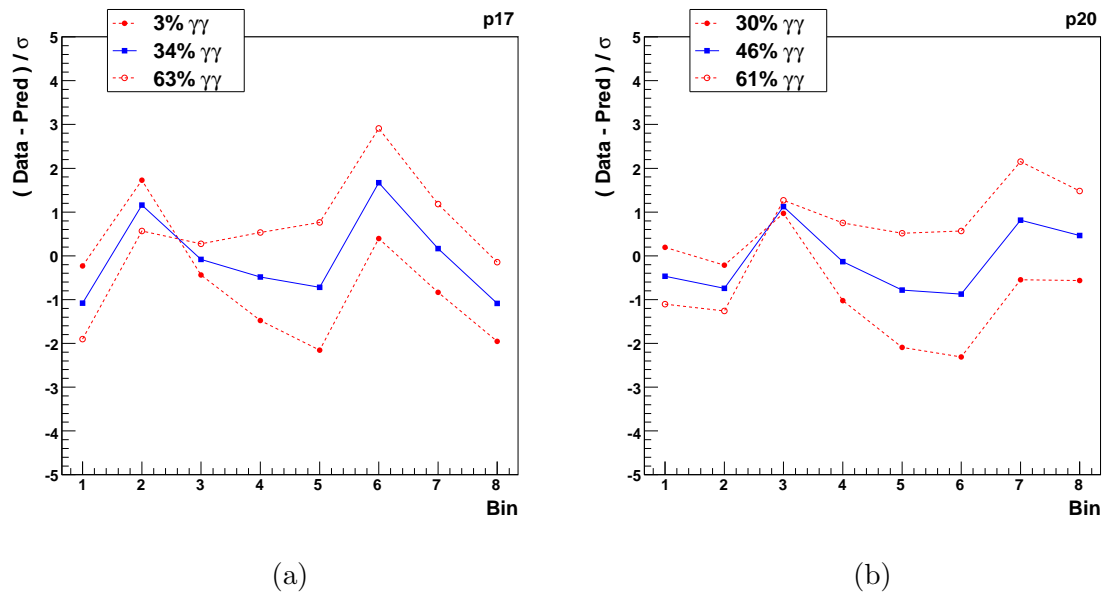


Figure 7.16: The pull of the data relative to the instrumental \cancel{E}_T prediction. The prediction is evaluated at p_0 (solid) and $p_0 \pm \delta p$ (dashed) in the 8 bins from 0-20 GeV used in the fit.

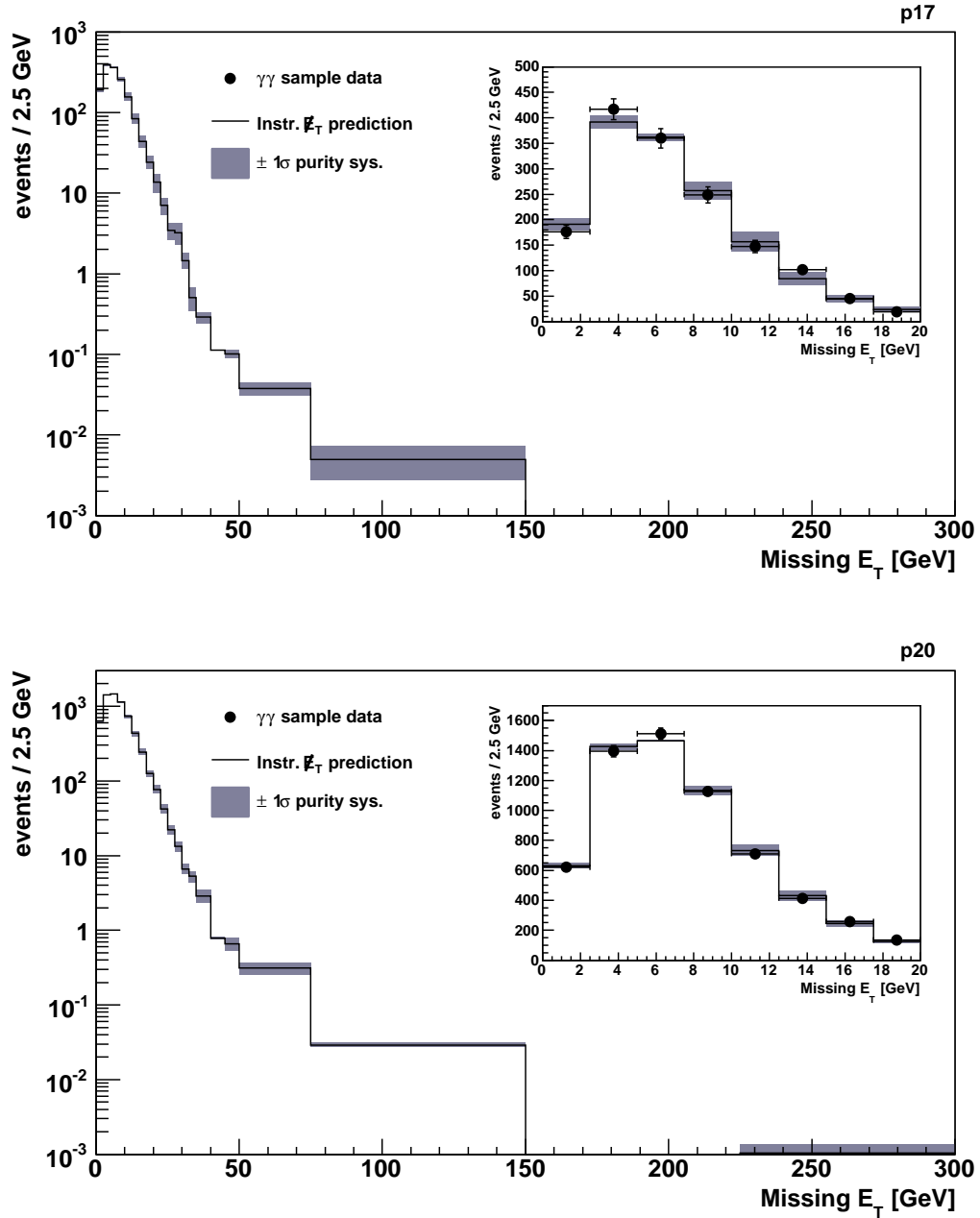


Figure 7.17: The predicted E_T distribution from instrumental backgrounds, as shown in Figure 7.14, but with the relative contributions suppressed. Instead, the shaded regions are displayed to indicate the $\pm 1\sigma$ shape uncertainty obtained by varying the central purity value, p_0 , by $\pm \delta p$.

7.2 Background Processes with Genuine \cancel{E}_T

Processes with genuine \cancel{E}_T contributing to the $\gamma\gamma$ sample are divided into two categories. The first category, described in Section 7.2.1, encompasses those events in which an electron from a W boson decay ($W \rightarrow e\nu$) is misidentified as a photon, and the escaping neutrino creates significant \cancel{E}_T . The second category, discussed in Section 7.2.2, consists of real SM $\gamma\gamma + \cancel{E}_T$ events. These processes are diphoton events produced in association with a W or a Z boson, which subsequently decays in a mode containing a neutrino.

7.2.1 Modeling \cancel{E}_T in SM Events with a Misidentified Electron

SM $W\gamma$ events are capable of faking the $\gamma\gamma + \cancel{E}_T$ signature if the W boson decays via $W \rightarrow e\nu$ and the electron is misidentified as a photon. Similarly, the production of W bosons in association with jets can also yield signal-like events if, in addition to the electron being misidentified as a photon, a jet is also misidentified as a photon. The rate that an electron fails the track veto was discussed in Section 6.3 and has been measured with data to be $f_{e \rightarrow \gamma} = 0.020 \pm 0.005$ [7]. The background contributions associated with a misidentified electron (referred to as “ele misID”) are determined with data using the $e\gamma$ sample.

The invariant mass distribution in $e\gamma$ sample events is shown in Figure 7.18. The contribution to the sample from events with a Z boson decaying via $Z \rightarrow ee$, with one of the electrons misidentified as a photon, is clearly visible. The number of $Z \rightarrow ee$ events in the $e\gamma$ sample is determined from a Gaussian fit to the peak with a polynomial background shape, as shown in Figure 7.18. The contribution is $40.0 \pm 3.6\%$ in p17 data, and $39.0 \pm 1.9\%$ in p20 data. The error is statistical and does not yet account for the systematic uncertainty associated with the fit model. In addition to $Z \rightarrow ee$ and genuine \cancel{E}_T processes resulting from a W boson decay, an appreciable contribution from multijet events is expected.

Figure 7.19 shows the \cancel{E}_T distribution in p17 and p20 $e\gamma$ sample events. The methods used to determine the four predicted contributions are now presented, with the estimation of the instrumental components, $Z \rightarrow ee$ and multijet (QCD), treated first. The shape of the \cancel{E}_T distribution for $Z \rightarrow ee$ events is the same shape introduced in Section 7.1.1, and is normalized to the number of events determined in the fit to the $e\gamma$ mass peak. With the

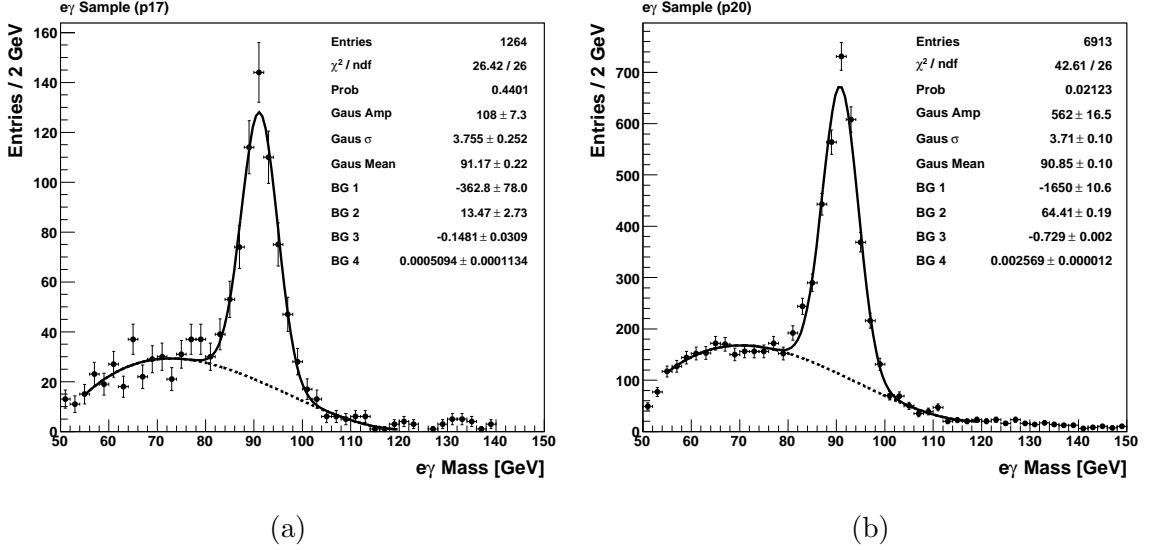
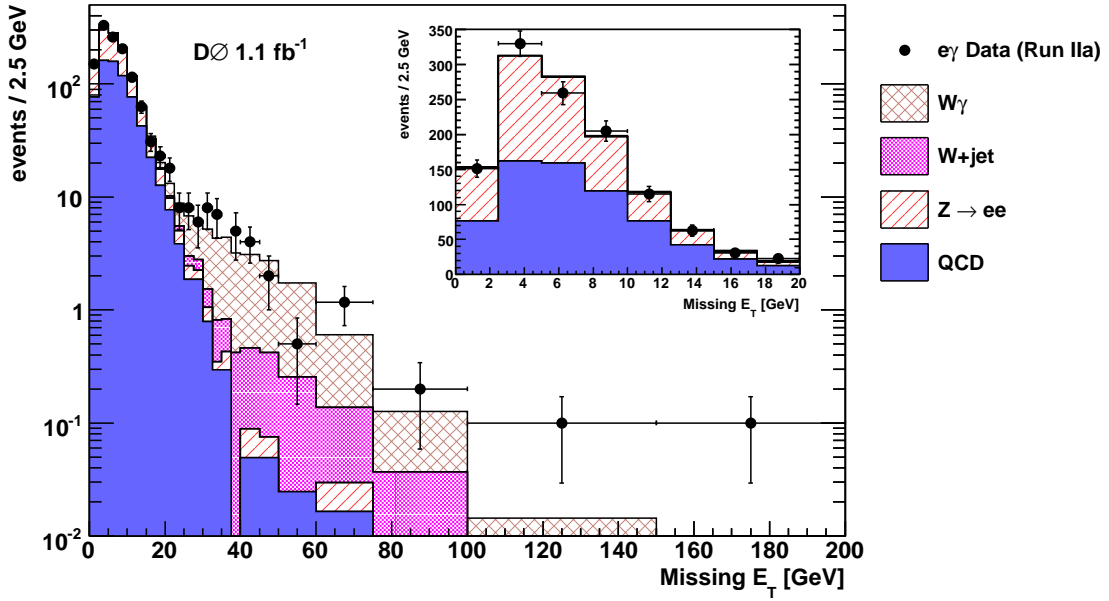


Figure 7.18: The $e\gamma$ invariant mass distribution for p17 (a) and p20 (b) data. A fit described in the text is performed to determine the $Z \rightarrow ee$ contribution.

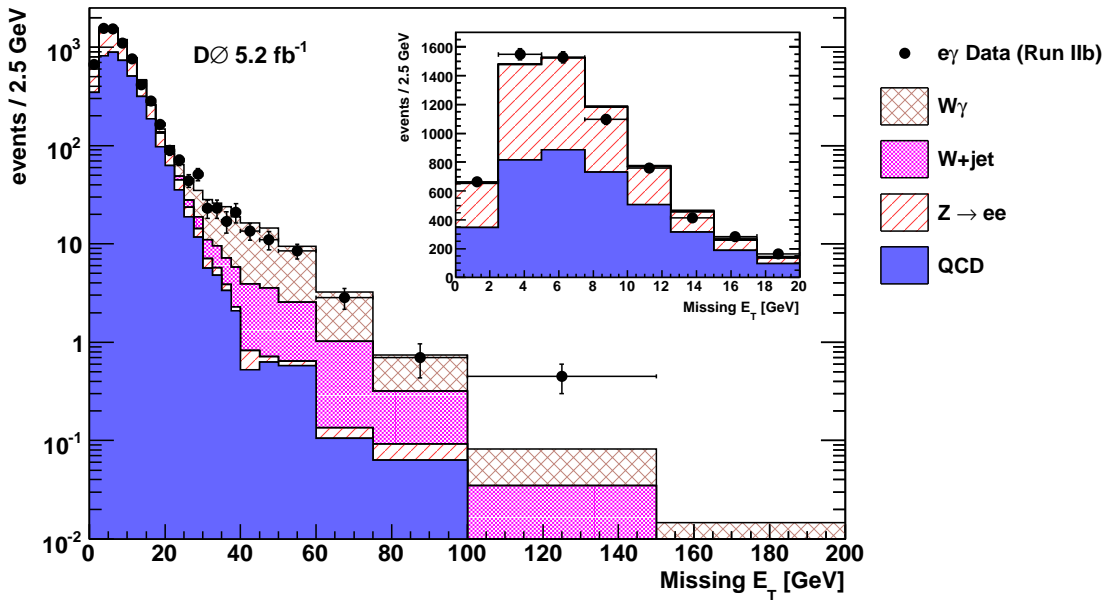
$Z \rightarrow ee$ contribution determined, the multijet contribution is normalized to the difference in the $\cancel{E}_T < 10$ GeV region between $e\gamma$ sample data and the $Z \rightarrow ee$ contribution, as contributions from genuine \cancel{E}_T events to this region are small. The multijet \cancel{E}_T shape is the same distribution introduced in Section 7.1.2.

Figure 7.19 reveals an excess, for \cancel{E}_T values greater than ≈ 20 GeV, of $e\gamma$ events beyond that predicted from the instrumental sources. This excess is referred to as the “inferred genuine \cancel{E}_T component”. When normalized using the $e \rightarrow \gamma$ fake rate, the inferred genuine \cancel{E}_T component, determined as the difference between $e\gamma$ data and the sum of instrumental backgrounds in Figure 7.19, represents the estimate used for the $e\gamma$ misID background contribution to the $\gamma\gamma$ sample.

To check our understanding of the composition of the inferred genuine \cancel{E}_T component, the $e\gamma$ sample events with $\cancel{E}_T > 30$ GeV are studied, as the instrumental \cancel{E}_T backgrounds are predicted to be small in this region. Figure 7.20 shows the transverse mass and photon NN for these events. The transverse mass distribution in PYTHIA $W(\rightarrow e\nu)\gamma$ MC events is also shown normalized to the number of data events for a comparison of the shapes of the distributions. The W boson peak in the transverse mass distribution indicates that the



(a)



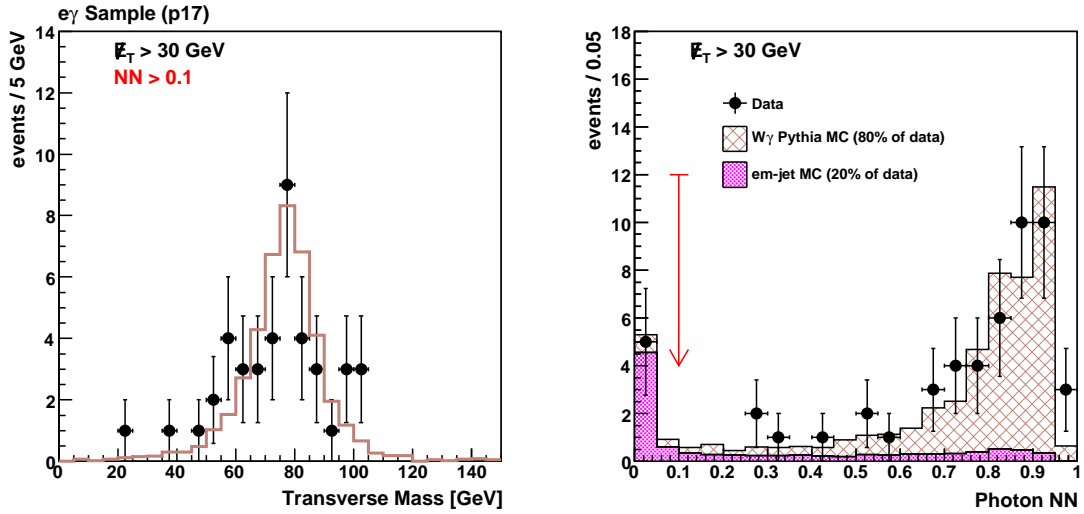
(b)

Figure 7.19: The E_T distribution for $e\gamma$ events in p17 (a) and p20 (b).

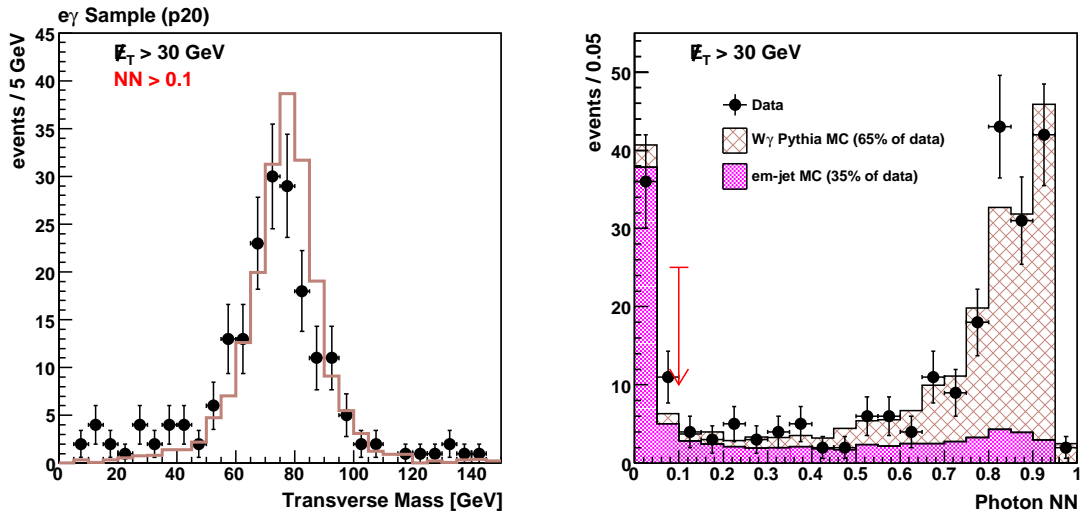
$\cancel{E}_T > 30$ GeV tail is dominated by $W(\rightarrow e\nu) + X$ events, where X denotes either a real photon or a jet that has faked a photon.

The photon NN is used to measure the $W + \text{jet}$ contribution. The $e\gamma$ sample requires that the photon satisfy $\text{NN} > 0.1$. However, the NN distributions in Figure 7.20 also show, to the left of the arrow, those events with $\text{NN} < 0.1$. These events are the $\cancel{E}_T > 30$ GeV events of the eh sample satisfying the standard IsEM-T criteria. When the eh sample selection is loosened to IsEM-L, the number of eh sample events becomes sufficient to see a transverse mass peak as well, indicative of $W + \text{jet}$ events. The $W + \text{jet}$ contribution for $\text{NN} > 0.1$ is determined by a fit of the data over the full NN range to a combination of a real photon MC NN distribution and a fake photon MC NN distribution. The fake photon MC NN distribution is obtained from EM-jet MC events where a jet has faked a photon satisfying the standard identification criteria. The fraction of the EM-jet distribution with $\text{NN} > 0.1$ is a measure of the $W + \text{jet}$ contribution. In p17, the $W + \text{jet}$ process is predicted to contribute $\approx 10\%$ to the $\cancel{E}_T > 30$ GeV region of the $e\gamma$ sample, while in p20 the predicted contribution is $\approx 20\%$. In Figure 7.19, the $W + \text{jet}$ contribution is represented by an ALPGEN-PYTHIA $W + \text{jet}$ \cancel{E}_T distribution normalized such that the $\cancel{E}_T > 30$ GeV tail is equal to this amount.

SM $W\gamma$ events are categorized as either production or final state radiation (FSR). Representative Feynman diagrams for the production processes at LO in α_s , that are simulated in PYTHIA, are shown in Figure 7.21 (a) and (b). NLO QCD corrections have been computed and made available in the simulation package WGAM_NLO [138]. Example virtual NLO correction diagrams are shown in Figure 7.21 (d) and (e), and an example real emission diagram is given in (f). Fully simulated PYTHIA $W\gamma$ MC events are used to determine the selection efficiencies and the \cancel{E}_T distribution. Kinematic distributions in PYTHIA, such as electron and photon p_T and η , and \cancel{E}_T , were studied at the level of MC truth and found to be similar to those from WGAM_NLO. Therefore, we treat the difference between NLO and LO by a k-factor which accounts for the difference in the predicted cross section. For the acceptance requirements of this analysis, the LO cross section is 70.38 fb in PYTHIA, compared with 65.80 fb for WGAM_NLO at LO, and 107.9 fb at NLO. In the following, PYTHIA MC events are scaled to the NLO cross section predicted by WGAM_NLO.



(a)



(b)

Figure 7.20: The transverse mass and photon NN variable for $\cancel{E}_T > 30$ GeV $e\gamma$ events in p17 (a) and p20 (b). The PYTHIA $W\gamma$ transverse mass shape is shown normalized to data for shape comparison. As described in the text, the NN variable is used to estimate the $W + \text{jet}$ contribution, and the remaining contribution is accounted for by $W\gamma$ production and FSR processes. The NN distributions show the $\text{NN} < 0.1$ region to the left of the red arrow. These are eh sample events.

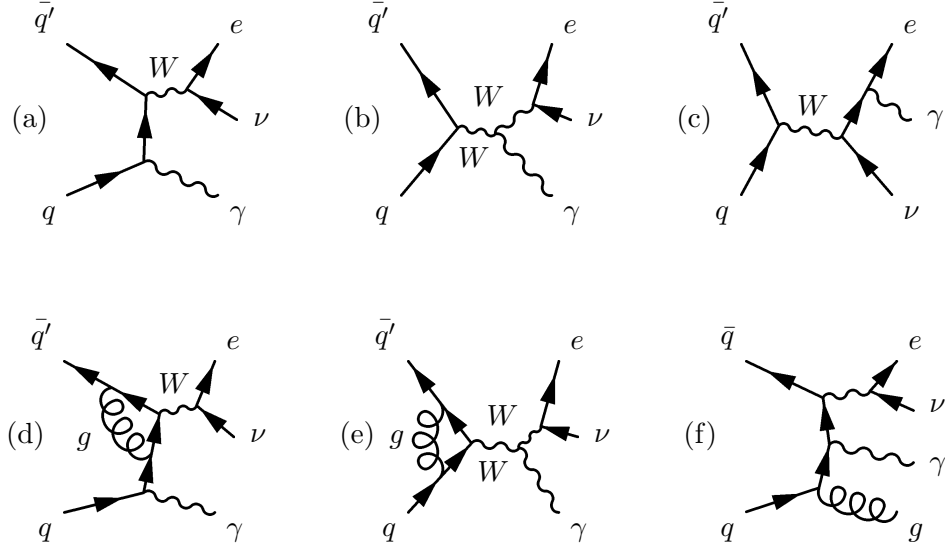


Figure 7.21: Representative Feynman diagrams for the SM processes contributing to the $p\bar{p} \rightarrow e\nu\gamma + X$ final state. Processes (a) and (b) are leading order in α_s , while processes (d), (e), and (f) illustrate higher order QCD corrections. Process (c) is the FSR process from inclusive W production.

The last $W\gamma$ process to consider is the FSR process shown in Figure 7.21 (c). This process is not included in either PYTHIA or WGAM_NLO. Figure 7.22 (a) shows the distribution of ΔR between the electron and the photon in $e\gamma$ events with $\cancel{E}_T > 30$ GeV for p17 and p20 data combined. The distribution for $W\gamma$ events is obtained from PYTHIA, and the distribution for $W + \text{jet}$ events is modeled using the eh sample. These two contributions are normalized as described in the preceding paragraphs. The excess of events at low $\Delta R(e, \gamma)$ is attributed to the $W\gamma$ FSR process. To verify this claim, a larger $e\gamma$ sample is studied, obtained by lowering the E_T requirements. The electron E_T requirement is lowered to $E_T > 20$ GeV, and the photon requirement to $E_T > 15$ GeV, as the radiated photon spectrum is expected to be rapidly decreasing with increasing E_T . Figure 7.22 (b) shows $\Delta R(e, \gamma)$ in the larger sample. The NLO prediction for $W\gamma$ production under these selection requirements is shown as well, and does not account for the large excess at low $\Delta R(e, \gamma)$ values, suggesting that the larger sample is dominated by the FSR process. The transverse mass is shown in Figure 7.22 (c), and appears bimodal, with the lower peak at

approximately 60 GeV. To illustrate that these are indeed $W\gamma$ FSR events, the transverse mass for events with $\Delta R(e, \gamma) < 1.0$ is shown in Figure 7.22 (d), computed with just the electron and then with the four-vectors of the electron and photon combined as one object. Including the photon restores the transverse mass peak at the expected value. Returning to Figure 7.22 (a), the difference between the data and the prediction is a measure of the $W\gamma$ FSR process contribution. To take this into account, the NLO $W\gamma$ prediction to the $e\gamma$ sample is scaled up by an additional 15%.

The \cancel{E}_T distribution for $e\gamma$ events is shown with the prediction for p17 and p20 combined in the top plot of Figure 7.23. The number of events with $\cancel{E}_T > 30$ and 50 GeV is given for the combined dataset, as well as for p17 and p20 separately, in Table 7.2. The predicted components are also listed. The methods used to determine the instrumental \cancel{E}_T contribution, and to account for the genuine \cancel{E}_T contributions in terms of $W + \gamma$ and $W + \text{jet}$, provide a good description of the data. The bottom plot in Figure 7.23 shows the inferred genuine \cancel{E}_T in $e\gamma$ events in the combined data set, *i.e.*, the difference between the data and instrumental \cancel{E}_T components. Also shown is the absolute prediction for $W\gamma$ production, FSR, and $W + \text{jet}$ events, validating our interpretation of the sources of the inferred genuine \cancel{E}_T .

The inferred genuine \cancel{E}_T distribution, obtained completely from data, constitutes the ele misID contribution to the $\gamma\gamma$ sample \cancel{E}_T distribution when scaled by $f_{e\rightarrow\gamma}/(1 - f_{e\rightarrow\gamma})$. The error bars on the inferred genuine \cancel{E}_T distribution combine the statistical uncertainty of the $e\gamma$ data and the statistical uncertainty on the scaled $Z \rightarrow ee$ and multi-jet distributions. The $e\gamma$ statistical uncertainty dominates for $\cancel{E}_T > 20$ GeV. The boundaries of the shaded region in Figure 7.23 represent the systematic uncertainty on the inferred genuine \cancel{E}_T when the $Z \rightarrow ee$ contribution is varied by $\pm 3\sigma$, where σ represents the statistical error on the $e\gamma$ mass peak fit. The 3σ variation corresponds to a $\sim 10\%$ uncertainty in the $Z \rightarrow ee$ contribution and is an estimate of the systematic uncertainty in the fit model. Varying the $Z \rightarrow ee$ contribution modifies the instrumental \cancel{E}_T prediction. The impact is mainly observed at low \cancel{E}_T as very little instrumental \cancel{E}_T is predicted relative to $e\gamma$ data beyond 30 GeV. The boundaries of the shaded region represent a shape uncertainty on the ele misID contribution which is treated as a systematic uncertainty.

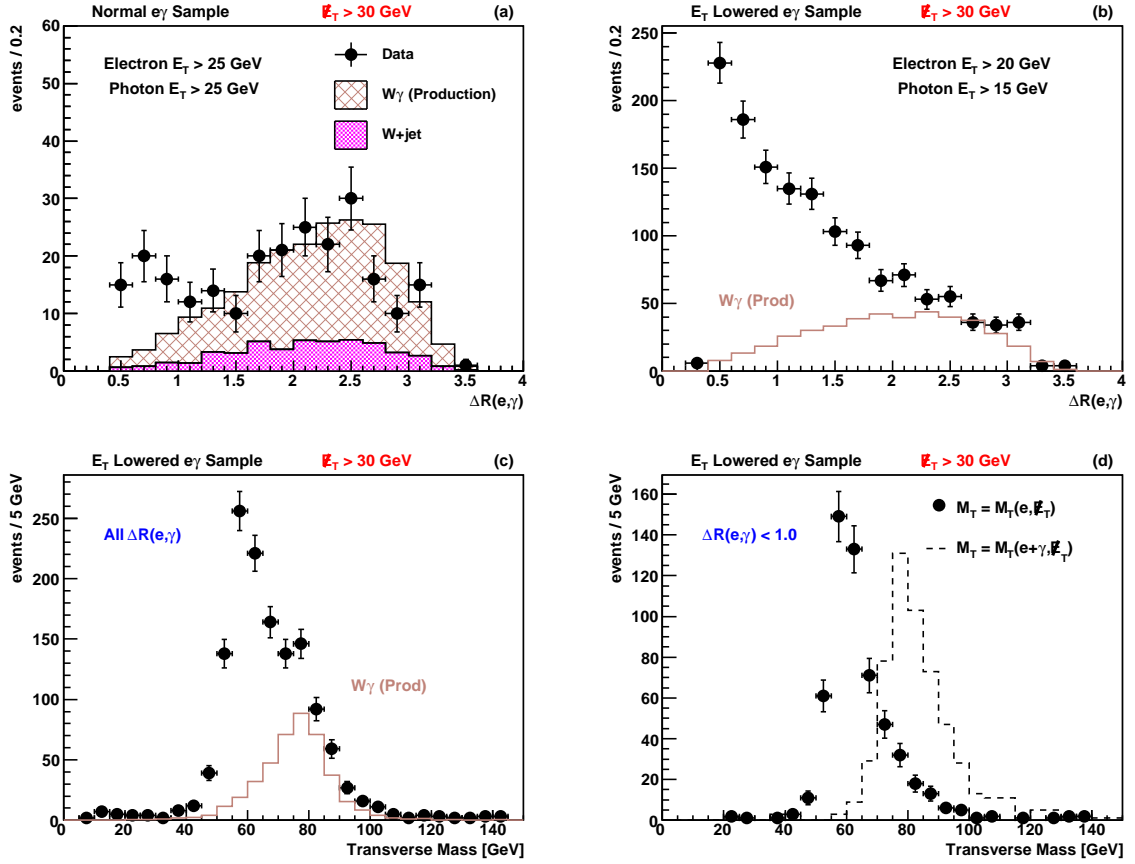


Figure 7.22: Figure (a) displays the $\Delta R(e, \gamma)$ distribution for $\cancel{E}_T > 30$ GeV $e\gamma$ events in the combined dataset. The $W\gamma$ and W + jet predictions are superimposed. A larger $e\gamma$ sample with lower E_T requirements is studied in (b,c,d). The $\Delta R(e, \gamma)$ distribution for this sample is shown in Figure (b). The $W\gamma$ production contribution is included for these acceptance requirements. The transverse mass is shown in (c) and displays a bimodal structure. The lower peak is isolated by requiring $\Delta R(e, \gamma) < 1.0$, as shown in (d). The peak near the W boson mass value is recovered when the photon vector is also included.

7.2.2 SM $W/Z + \gamma\gamma$ Events

In addition to genuine \cancel{E}_T events originating from $W \rightarrow e\nu$ events, with the electron misidentified as a photon, genuine \cancel{E}_T events may also be produced by real SM diphoton processes. These diphoton processes involve the production of an associated intermediate vector boson

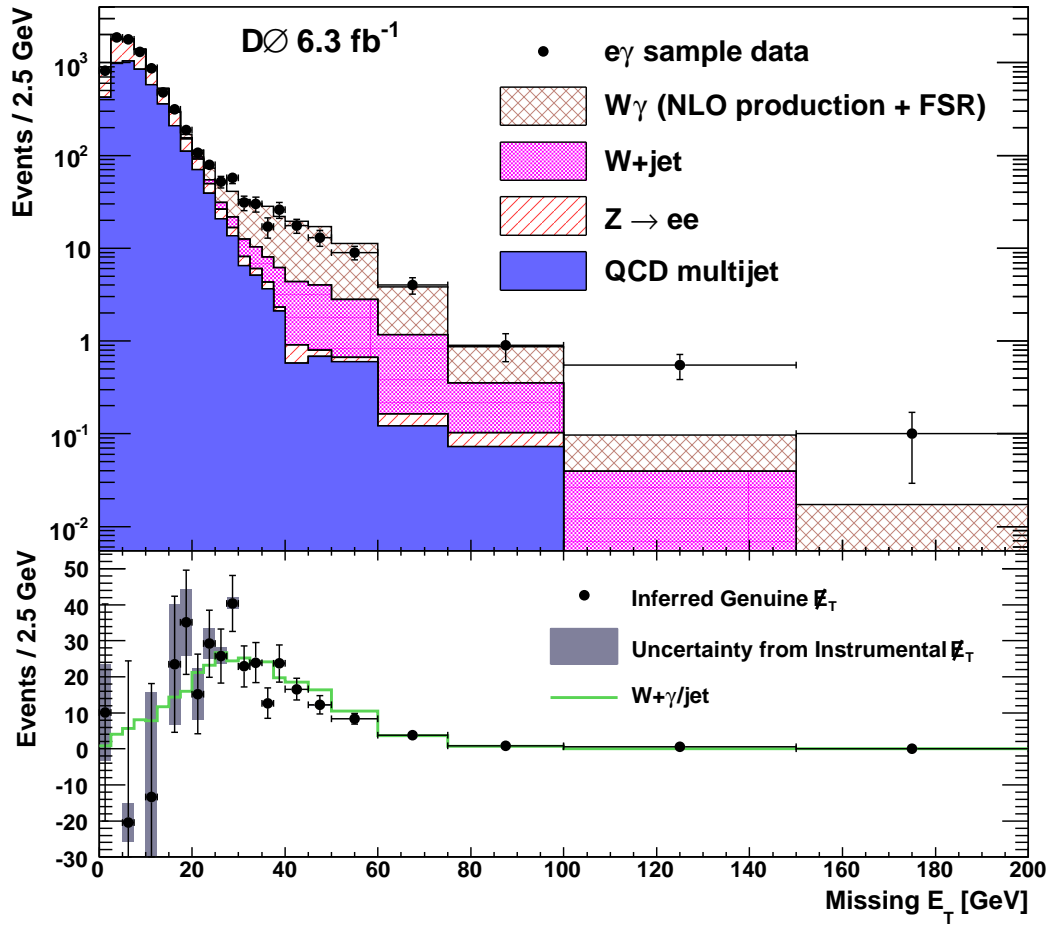


Figure 7.23: (Top) The E_T distribution for the combined $e\gamma$ sample with the predicted contributions from instrumental and genuine E_T processes. (Bottom) The inferred genuine E_T distribution, *i.e.* the difference between $e\gamma$ data and the instrumental E_T sources, shown on a linear scale, along with the $W + \gamma$ /jet cross-check.

| | Data | Prediction | $W\gamma$ | $W + \text{jet}$ | $Z \rightarrow ee$ | QCD |
|---------------------------------|------|-----------------|-----------------|------------------|--------------------|----------------|
| $\cancel{E}_T > 30 \text{ GeV}$ | | | | | | |
| p17 | 47 | 40.9 ± 0.8 | 33.3 ± 0.7 | 5.1 ± 0.2 | 0.7 ± 0.1 | 1.9 ± 0.4 |
| p20 | 200 | 225.2 ± 4.2 | 156.2 ± 3.3 | 42.6 ± 1.4 | 4.6 ± 0.4 | 21.8 ± 2.1 |
| Combined | 247 | 266.1 ± 4.3 | 189.5 ± 3.4 | 47.7 ± 1.4 | 5.3 ± 0.4 | 23.7 ± 2.1 |
| $\cancel{E}_T > 50 \text{ GeV}$ | | | | | | |
| p17 | 15 | 12.2 ± 0.4 | 9.9 ± 0.4 | 1.9 ± 0.1 | 0.1 ± 0.1 | 0.3 ± 0.2 |
| p20 | 67 | 66.7 ± 2.1 | 46.3 ± 1.8 | 16.0 ± 0.9 | 0.7 ± 0.1 | 3.6 ± 0.9 |
| Combined | 82 | 78.9 ± 2.1 | 56.2 ± 1.8 | 17.9 ± 0.9 | 0.8 ± 0.1 | 3.9 ± 0.9 |

Table 7.2: Observed and predicted number of $e\gamma$ events with $\cancel{E}_T > 30 \text{ GeV}$ and $\cancel{E}_T > 50 \text{ GeV}$ in p17, p20, and combined (6.3 fb^{-1}). The individual contributions from $W\gamma$, $W + \text{jet}$, $Z \rightarrow ee$, and QCD multijet are also listed.

which decays in a mode that contains a neutrino. Representative Feynman diagrams are shown in Figure 7.24. The small contributions of these processes to the $\gamma\gamma$ sample are estimated using MC. MADGRAPH and MADEVENT [130] were used to generate the relevant Feynman diagrams, amplitudes, and parton level events. Events with inclusive W and Z decays were generated, as all decay modes can enter the selected $\gamma\gamma$ sample. The events were then showered with PYTHIA followed by full GEANT detector simulation and event reconstruction. The cross section when the photons are required to satisfy $E_T > 25 \text{ GeV}$ and $\eta < 1.1$ is 2.22 fb for $Z + \gamma\gamma$ and 0.97 fb for $W + \gamma\gamma$.

Figure 7.25 shows the \cancel{E}_T distribution for $Z + \gamma\gamma$ and $W + \gamma\gamma$ events passing the event selection requirements. The histograms have been normalized to 1 fb^{-1} for reference. The integral is 0.58 ± 0.01 events per fb^{-1} for $Z + \gamma\gamma$ and 0.26 ± 0.01 events per fb^{-1} for $W + \gamma\gamma$. In both cases, $\approx 13\%$ of selected events have $\cancel{E}_T > 50 \text{ GeV}$. The shaded region shows the distribution of the subset of events where $Z \rightarrow \nu\nu$ and $W \rightarrow l\nu$. In the $Z\gamma\gamma$ case a small fraction of the high \cancel{E}_T events arise from $Z \rightarrow \tau\tau$. The inclusive distributions are used in the estimation of the small contribution to the $\gamma\gamma$ sample \cancel{E}_T distribution.

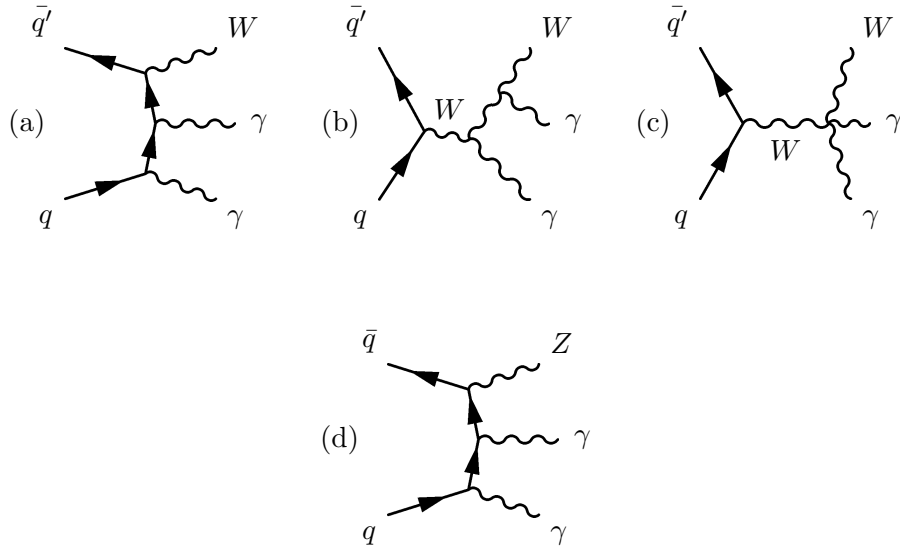


Figure 7.24: Representative Feynman diagrams for the SM processes $p\bar{p} \rightarrow W\gamma\gamma$ (a, b, c) and $p\bar{p} \rightarrow Z\gamma\gamma$ (d).

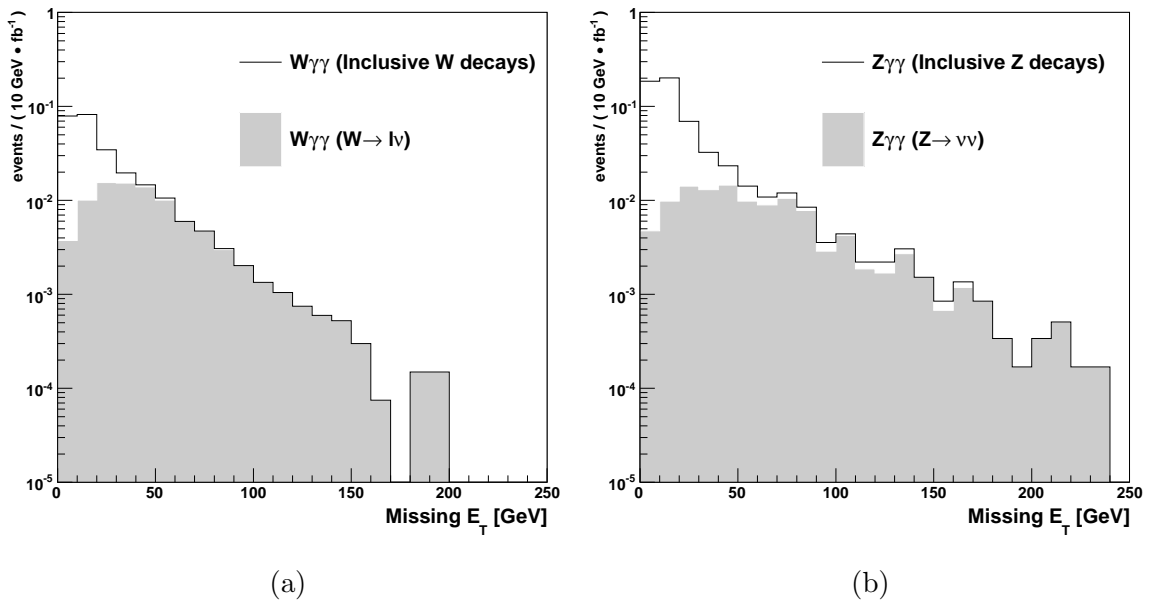


Figure 7.25: The \cancel{E}_T distribution in $W+\gamma\gamma$ (a) and $Z+\gamma\gamma$ (b) MC events. The distributions are shown after all selections have been made and are normalized to 1 fb^{-1} . The contribution from W/Z boson decay modes containing a neutrino are shown as the shaded regions.

Chapter 8

Results

After a discussion of the various sources of systematic uncertainties in the analysis, the final results of the search are presented.

8.1 Systematic Uncertainties

With the description of the event selection, expected signal production and efficiency, and background estimation methods now complete, the various systematic uncertainties are collected and reviewed. Uncertainties in the contributions from background components derived from data are considered first, followed by the uncertainties in the contributions from the SM $W/Z + \gamma\gamma$ and signal model processes.

Table 8.1 itemizes the systematic uncertainties for each component of the analysis. The first systematic uncertainty associated with the instrumental \cancel{E}_T prediction is the uncertainty in shape of the SM $\gamma\gamma$ \cancel{E}_T distribution. In order to account for the difference shown in Figure 7.5 between ee data and SM $\gamma\gamma$ MC at high \cancel{E}_T values, the average of the two distributions is used. The two extremes, fully ee data and fully SM $\gamma\gamma$ MC, define a systematic uncertainty on the shape of the SM $\gamma\gamma$ \cancel{E}_T distribution. Next, by examining the sensitivity of the jet misID sample \cancel{E}_T distribution to changes in the selection requirements on the variables comprising the IsEM definition, a shape uncertainty on this distribution is obtained. Lastly, as a consequence of the definition of instrumental \cancel{E}_T given in Equation 7.1, and the constraint expressed in Equation 7.2, the $\gamma\gamma$ and jet misID contributions are anticorrelated

as a function of purity. Uncertainty in the purity therefore results in an uncertainty in the overall instrumental \cancel{E}_T distribution prediction, as was shown in Figure 7.17.

Systematic uncertainties in the ele misID contribution are listed next in Table 8.1. The first ele misID uncertainty is similar to the purity systematic discussed above. As a consequence of the uncertainty in the $Z \rightarrow ee$ contribution to the $e\gamma$ sample, and the QCD multi-jet normalization to the difference between data and $Z \rightarrow ee$ for $\cancel{E}_T < 10$ GeV, there is a corresponding uncertainty in the prediction for the shape of the instrumental \cancel{E}_T contribution to the $e\gamma$ sample. Since the inferred genuine \cancel{E}_T distribution in the $e\gamma$ sample is the difference between the $e\gamma$ data and predicted instrumental \cancel{E}_T distributions, the uncertainty in the $Z \rightarrow ee$ contribution results in a corresponding uncertainty in the ele misID contribution. The uncertainty is presented as the boundary of the shaded re-

| Component | Systematic | Type |
|--|--|-------|
| Instrumental \cancel{E}_T (SM $\gamma\gamma$ + jet misID) | SM $\gamma\gamma$ \cancel{E}_T distribution: ee data vs. $\gamma\gamma$ MC | Shape |
| | jet misID \cancel{E}_T distribution | Shape |
| | Purity uncertainty | Shape |
| ele misID | Uncertainty in residual from instrumental \cancel{E}_T | Shape |
| | Normalization uncertainty (25%) from $e \rightarrow \gamma$ fake rate | Flat |
| $W/Z + \gamma\gamma$ | Luminosity (6.1%) | Flat |
| | CPS-PV scale factor (3%) | Flat |
| | PhotonID (3% per photon) | Flat |
| | Trigger (2%) | Flat |
| GMSB and UED Signal | Luminosity (6.1%) | Flat |
| | CPS-PV scale factor (3%) | Flat |
| | PhotonID (3% per photon) | Flat |
| | Trigger (2%) | Flat |
| | PDFs (GMSB 5%, UED 20%) | Flat |

Table 8.1: Compilation of the various sources of systematic uncertainties.

gion in the bottom plot of Figure 7.23. The uncertainty is mainly significant in the low \cancel{E}_T region, where it is comparable to the statistical uncertainty. The second ele misID contribution uncertainty reflects the uncertainty in the normalization of the inferred genuine \cancel{E}_T distribution, which arises from the 25% uncertainty in the electron faking photon rate, $f_{e \rightarrow \gamma} = 0.020 \pm 0.005$.

Uncertainties in the integrated luminosity, and trigger and selection efficiencies impact the contributions obtained with MC, *i.e.* the SM $W/Z + \gamma\gamma$ background and signal model processes. The luminosity uncertainty is 6.1%. The CPS-PV scale factor uncertainty discussed in Section 6.5 contributes 3% to the overall normalization, while the uncertainty in photon identification efficiencies contribute 3% per photon, and the trigger efficiency 2%. As listed in Table 8.1, these uncertainties are constant (flat) as a function of \cancel{E}_T .

Uncertainties arising from parton distribution functions (PDF) are evaluated [139] using `cteq61M` central value and associated error PDF sets [131]. Uncertainties in PDFs are found to have a very small impact on the signal acceptance. The uncertainty on the total cross section is conservatively assigned by using the error set yielding the highest uncertainty. For GMSB, the uncertainty is up to 5%, while for UED it is up to 20%.

8.2 Final Search Results

Figure 8.1 presents the \cancel{E}_T distribution for the $\gamma\gamma$ sample using the full 6.3 fb^{-1} dataset. Table 8.2 summarizes the SM background prediction and observed number of events in the signal sensitive $\cancel{E}_T > 50 \text{ GeV}$ region, the region which remained blinded during the course of the analysis. The table lists the contributions from instrumental and genuine \cancel{E}_T SM background sources, and also provides the expected number of events for the SM in the presence of signal events for the model points shown in Figure 8.1. The uncertainties shown include both statistical and systematic uncertainties, and the uncertainty in the signal contribution associated with PDFs is included. The data agrees well with the SM background prediction over the entire range of \cancel{E}_T values, and no significant excess beyond the expected SM background is observed.

Table 8.3 provides a more detailed breakdown of the SM background expectation, as well as the observed number of events, in three intermediate to high \cancel{E}_T intervals. The largest background contribution is from events with misidentified jets, which also typically contribute the most to the overall uncertainty in the background estimate. For large \cancel{E}_T values, beyond 75 GeV, the contributions from instrumental and genuine \cancel{E}_T sources are roughly similar. Tables 8.4 and 8.5 show the expected number of signal events for GMSB and UED, respectively, in the same three \cancel{E}_T intervals.

As the observed \cancel{E}_T distribution in $\gamma\gamma$ sample events is in good agreement with the expected SM background distribution, limits are derived on the GMSB and UED signal models using a Poisson log-likelihood ratio test [140]. The negative log-likelihood ratio (NLLR) is defined as

$$NLLR = 2 \sum_i \left(s_i - d_i \ln \left(1 + \frac{s_i}{b_i} \right) \right). \quad (8.1)$$

In this analysis, s_i , b_i , and d_i , represent the number of expected signal, expected background, and observed events, respectively, in the i^{th} bin of the $\gamma\gamma$ sample \cancel{E}_T distribution. Pseudo-experiments, or sets of Poisson pseudo-data $\{d_i\}$, are generated [141] according to background-only and signal-plus-background hypotheses, for different Λ and R_c^{-1} values. The quantities s_i and b_i vary over pseudo-experiments according to their uncertainties. For example, the uncertainty in the integrated luminosity is accounted for by uniformly shifting, according to a Gaussian distribution with standard deviation 6.1%, each s_i value by the same amount within a given pseudo-experiment. Additionally, as the backgrounds in this analysis are primarily estimated with data, statistical uncertainties in b_i are important. Uncertainties in \cancel{E}_T distribution shapes are accounted for by variations as a function of i over pseudo-experiments. The collection of $NLLR$ values for the two hypotheses constitute probability distributions (PDs) which are integrated according to the CL_s convention [140] to obtain an expected limit. The observed limit is obtained by using the observed data to evaluate Equation 8.1. This $NLLR$ value can be compared to the most probable values of the background-only and signal-plus-background PDs, and serves as a limit of integration in evaluating the observed limit.

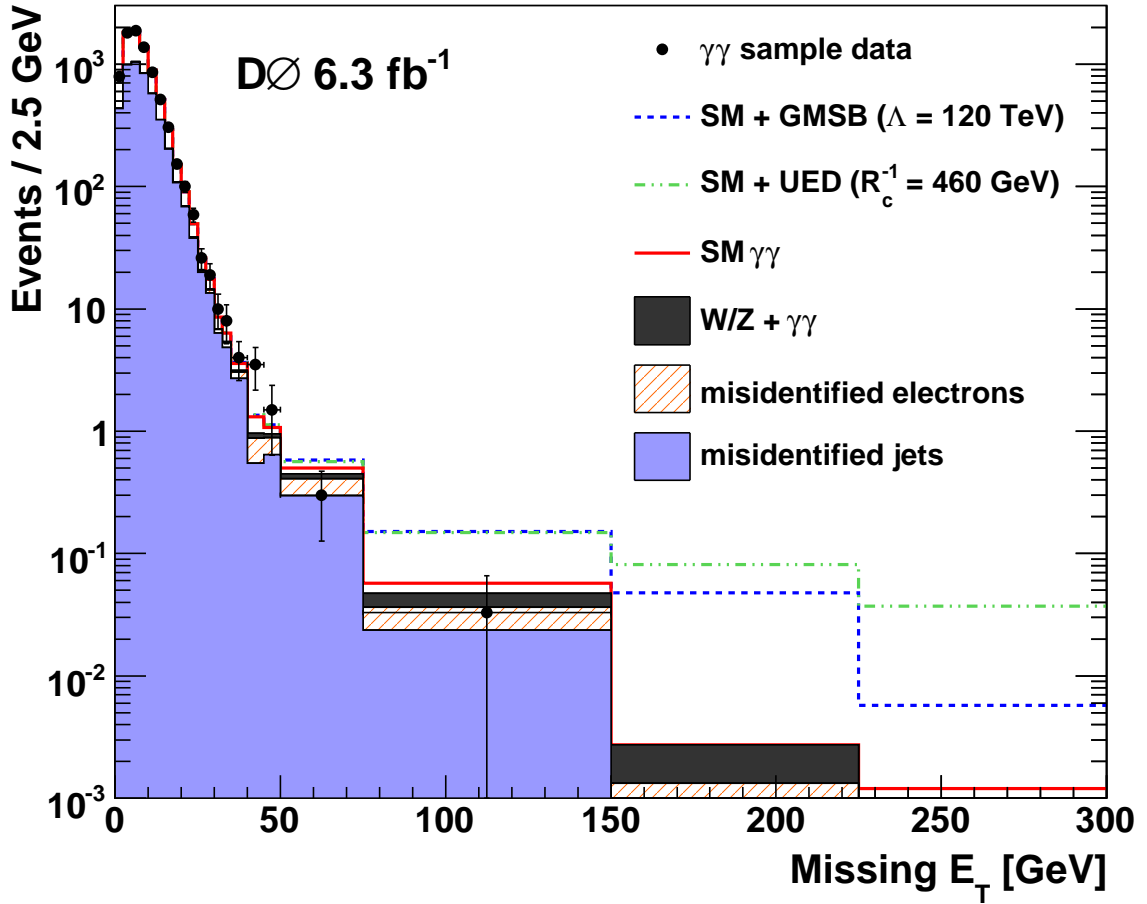


Figure 8.1: \cancel{E}_T distribution in the $\gamma\gamma$ sample shown with statistical uncertainty and expected SM background from events with a misidentified jet, a misidentified electron, $W/Z + \gamma\gamma$ events, and SM $\gamma\gamma$ events. The expected \cancel{E}_T distribution in the presence of GMSB and UED events is also displayed for example values of Λ and R_c^{-1} , respectively.

| $\cancel{E}_T > 50 \text{ GeV}$ | |
|-------------------------------------|-----------------------------------|
| Instrumental \cancel{E}_T | 4.56 ± 0.94 |
| Genuine \cancel{E}_T | 2.30 ± 0.31 |
| Total SM Background | 6.86 ± 0.99 |
| Observed Events | 4 |
| SM+GMSB $\Lambda = 120 \text{ TeV}$ | 12.04 ± 1.08 |
| SM+UED $R_c = 460 \text{ GeV}$ | 13.93 ± 1.74 |

Table 8.2: Expected number of background events from instrumental and genuine \cancel{E}_T sources, total expected SM background, and observed number of $\gamma\gamma$ events with $\cancel{E}_T > 50 \text{ GeV}$ for 6.3 fb^{-1} . The expected number of events for the SM in the presence of signal for two model points is also provided. Combined statistical and systematic uncertainty values are shown, and include PDF uncertainties.

| \cancel{E}_T interval, GeV | Observed Events | Expected SM Background Events | | | | |
|---------------------------------|--------------------|-------------------------------|-------------------|---------------|---------------|----------------------|
| | | Total | SM $\gamma\gamma$ | jet misID | ele misID | $W/Z + \gamma\gamma$ |
| 35-50 | 18 | 11.9 ± 2.0 | 1.8 ± 1.4 | 7.8 ± 1.4 | 1.9 ± 0.5 | $0.5 \pm (< 0.1)$ |
| 50-75 | 3 | 5.0 ± 0.9 | 0.5 ± 0.4 | 3.0 ± 0.7 | 1.1 ± 0.3 | $0.4 \pm (< 0.1)$ |
| > 75 | 1 | 1.9 ± 0.4 | 0.3 ± 0.2 | 0.8 ± 0.3 | 0.4 ± 0.1 | $0.4 \pm (< 0.1)$ |

Table 8.3: Observed number of $\gamma\gamma$ events and total expected SM background in three \cancel{E}_T intervals for 6.3 fb^{-1} . The expected SM background is also presented according to the contributions from SM $\gamma\gamma$ events, events with misidentified jets, events with misidentified electrons, and $W/Z + \gamma\gamma$ events. Combined statistical and systematic uncertainty values are shown.

| \cancel{E}_T interval, GeV | GMSB | | |
|---------------------------------|--|--|--|
| | $\Lambda = 110$ TeV ($\sigma = 13.3$ fb) | $\Lambda = 120$ TeV ($\sigma = 6.52$ fb) | $\Lambda = 130$ TeV ($\sigma = 3.15$ fb) |
| 35-50 | 0.87 ± 0.09 | 0.31 ± 0.03 | 0.18 ± 0.02 |
| 50-75 | 1.91 ± 0.18 | 0.83 ± 0.08 | 0.38 ± 0.03 |
| > 75 | 7.73 ± 0.73 | 4.35 ± 0.41 | 2.40 ± 0.22 |

Table 8.4: Expected number of GMSB events in 6.3 fb^{-1} for three Λ values in three \cancel{E}_T intervals. The displayed cross sections are NLO values. The combined statistical and systematic uncertainty values are listed, and include the uncertainty due to PDFs.

| \cancel{E}_T interval, GeV | UED | | |
|---------------------------------|---|---|---|
| | $R_c^{-1} = 440$ GeV ($\sigma = 11.0$ fb) | $R_c^{-1} = 460$ GeV ($\sigma = 5.70$ fb) | $R_c^{-1} = 480$ GeV ($\sigma = 2.99$ fb) |
| 35-50 | 0.75 ± 0.17 | 0.28 ± 0.06 | 0.11 ± 0.02 |
| 50-75 | 1.50 ± 0.33 | 0.62 ± 0.14 | 0.25 ± 0.06 |
| > 75 | 12.74 ± 2.80 | 6.45 ± 1.42 | 3.18 ± 0.70 |

Table 8.5: Expected number of UED events in 6.3 fb^{-1} for three R_c^{-1} values in three \cancel{E}_T intervals. The displayed cross sections are LO values. The combined statistical and systematic uncertainty values are listed, and include the uncertainty due to PDFs.

Figure 8.2 illustrates the impact of various uncertainties in this analysis for a representative GMSB model point. The expected cross section limit, and the $\pm 1\sigma$ and $\pm 2\sigma$ variations in the pseudo-experiments with respect to the central value, are shown for this model point as a function of different categories of uncertainty. The first noteworthy feature is the asymmetry of the variations of the expected limit with respect to the central value. This is an artifact of Poisson uncertainty in the expected number of events, and the limit when only this source of uncertainty is accounted for is given in the left-most category. The plot shows the progression as further uncertainties are added to the cross limit analysis. Statistical uncertainties dominate the total uncertainty in this analysis and the expected cross section limit is shown to degrade by only $\approx 10\%$ when all uncertainties beyond Poisson fluctuations in the expected number of events are included.

Figure 8.3 presents the predicted NLO cross section for the SPS8 GMSB model, and the 95% C.L. expected and observed exclusion limits, as a function Λ . The PDF uncertainty is shown as an uncertainty in the theoretical prediction and is not included in the limit setting analysis. The corresponding masses of the lightest neutralino (χ_1^0) and lightest chargino (χ_1^\pm) are also displayed. The observed cross section limit is in good agreement with the expectation and excludes $\Lambda < 124$ TeV and $m_{\chi_1^0} < 175$ GeV at 95% C.L. This represents improvements of 50 GeV [12] and 26 GeV [74] in the limit on the χ_1^0 mass with respect to previous limits on this model.

Figure 8.4 presents the predicted LO cross section for the UED scenario with $\tilde{\Lambda}R_c^{-1} = 20$, $N = 6$, and $M_D = 5$ TeV, and the 95% C.L. expected and observed exclusion limits, as a function of R_c^{-1} . The PDF uncertainty is shown as an uncertainty in the theoretical prediction and is not included in the limit setting analysis. The corresponding masses of the $SU(2)_L$ doublet KK quark (q_D^*) and KK gluon (g^*) are also displayed. The KK photon mass is $\approx R_c^{-1}$. The observed cross section limit is in good agreement with the expectation and excludes $R_c^{-1} < 477$ GeV, $m_{q_D^*} < 559$ GeV, and $m_g < 597$ GeV at 95% C.L. The cross section limit is slightly stronger than the GMSB limit as a result of the harder \cancel{E}_T distribution and slightly higher signal efficiency in UED. These are the first limits derived on this UED scenario.

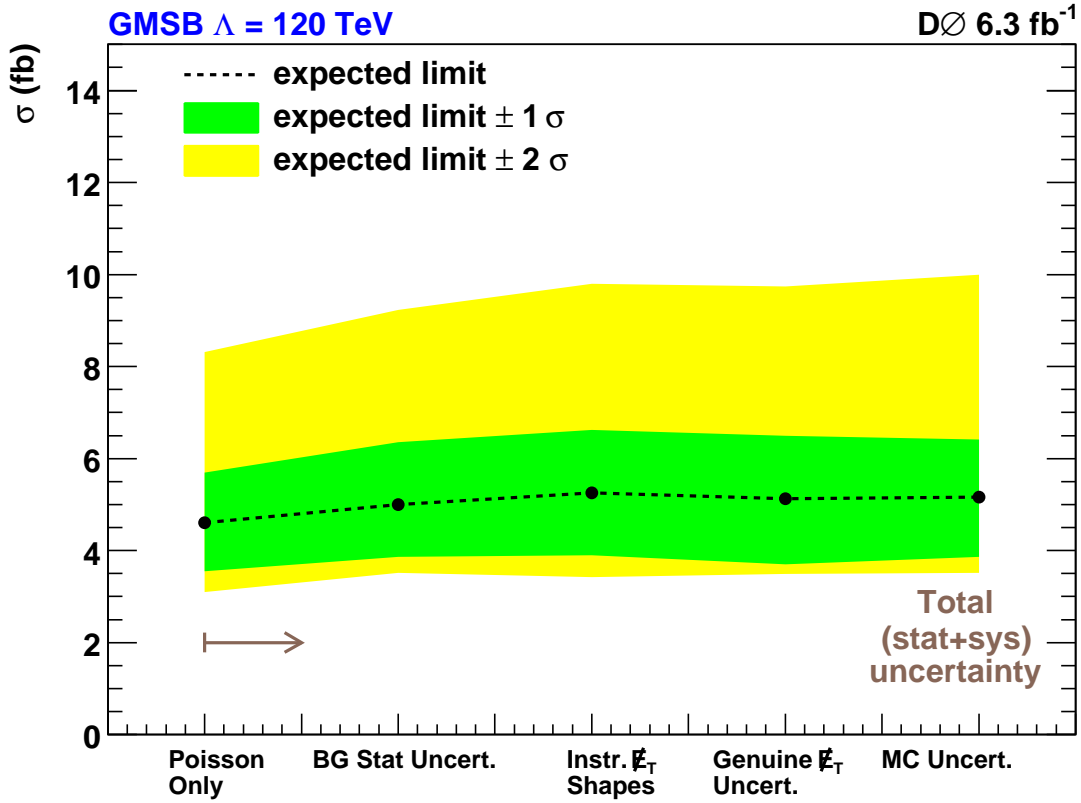


Figure 8.2: Illustration of the impact of various uncertainties on the expected cross section limit for the GMSB $\Lambda = 120$ TeV point. The expected 95% C.L. cross section limit, and $\pm 1\sigma$ and $\pm 2\sigma$ deviations of pseudo-experiments with respect to the central value are shown as the listed source of uncertainty is added in addition to the preceding sources in the limit setting analysis.

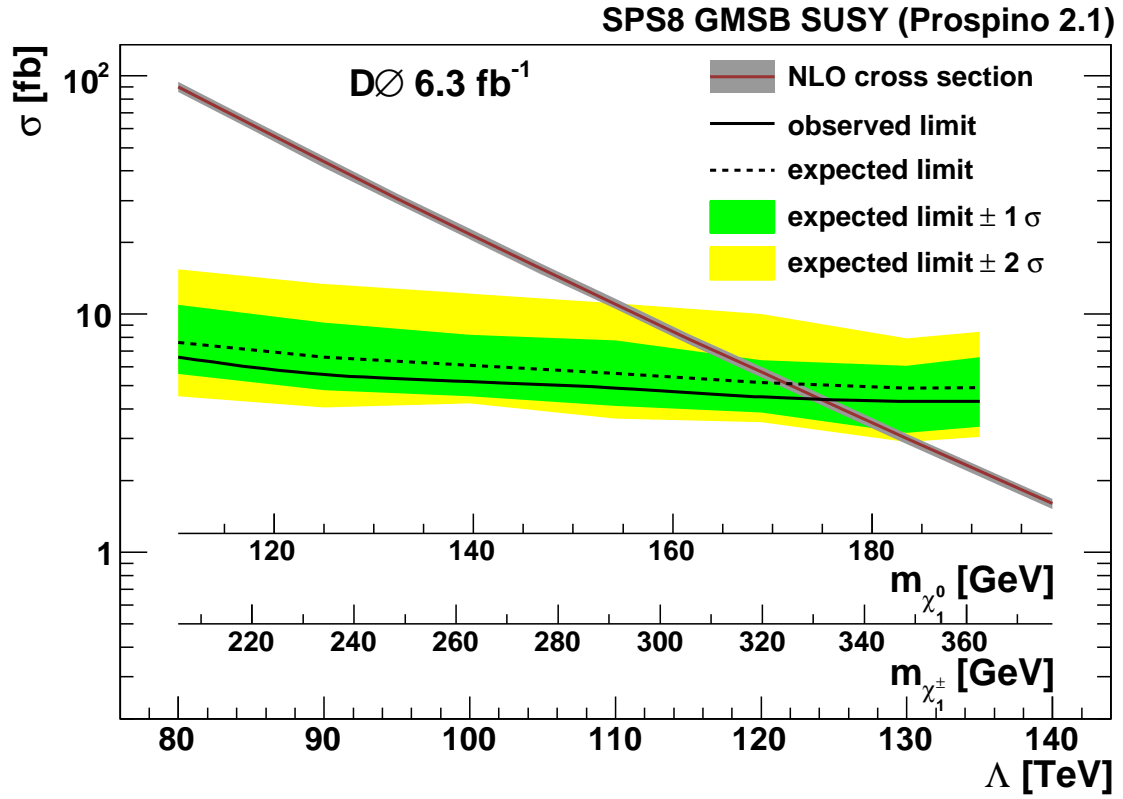


Figure 8.3: The predicted NLO cross section for the SPS8 GMSB model, and the 95% C.L. expected and observed exclusion limits, as a function of Λ . The corresponding masses of the lightest neutralino (χ_1^0) and lightest chargino (χ_1^\pm) are also displayed.

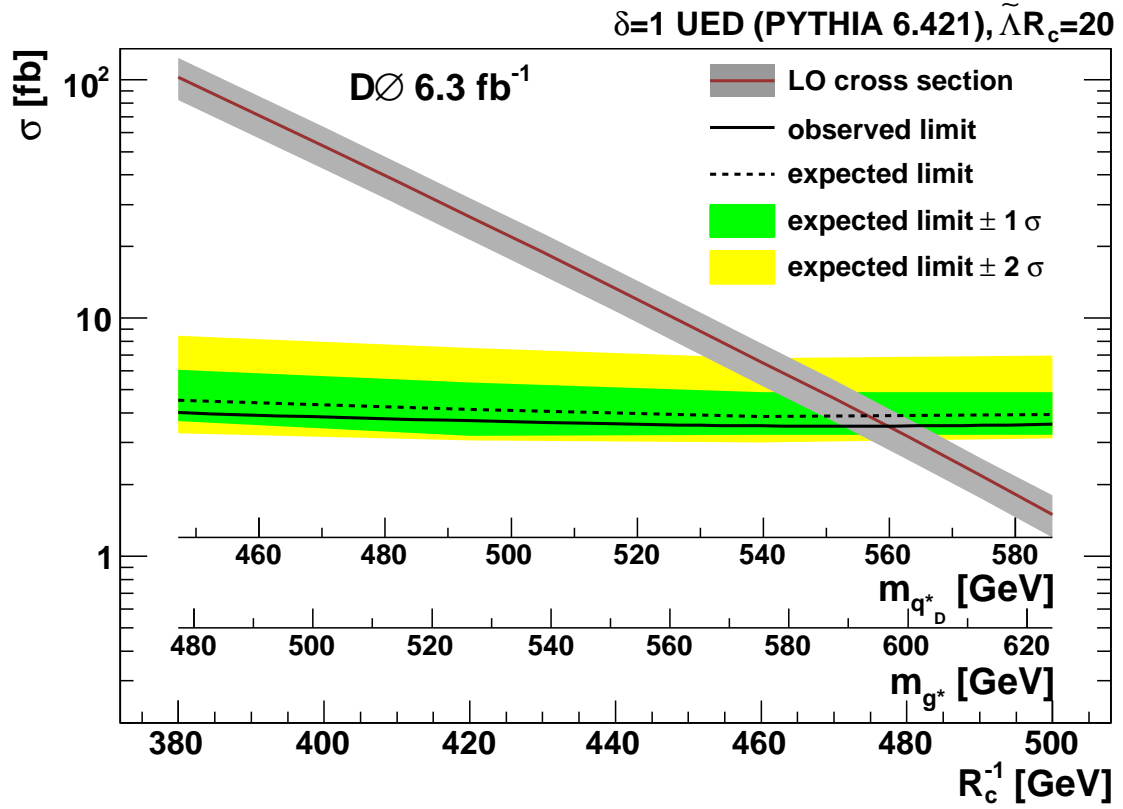


Figure 8.4: The predicted LO cross section for the UED model (with $\tilde{\Lambda} R_c^{-1} = 20$, $N = 6$, and $M_D = 5$ TeV), and the 95% C.L. expected and observed exclusion limits, as a function of R_c^{-1} . The corresponding masses of the $SU(2)_L$ doublet KK quark (q_D^*) and KK gluon (g^*) are also displayed. The KK photon mass is $\approx R_c^{-1}$.

Chapter 9

Conclusions and Outlook

A search for diphoton events with large missing transverse energy produced in $p\bar{p}$ collisions at $\sqrt{s} = 1.96$ TeV has been presented. The data were collected with the D0 detector at the Fermilab Tevatron Collider between 2002 and 2010, and correspond to 6.3 fb^{-1} of integrated luminosity. The observed missing transverse energy distribution is well described by the Standard Model prediction, and 95% C.L. limits were derived on two realizations of theories beyond the Standard Model. In a gauge mediated supersymmetry breaking scenario, the breaking scale Λ is excluded for $\Lambda < 124$ TeV, representing the strongest limit to date on the SPS8 model line. The limit excludes $m_{\chi_1^0} < 175$ GeV, $m_{\chi_1^\pm} < 332$ GeV, and squark and gluino masses below 1 TeV. In a universal extra dimension model including gravitational decays, the compactification radius R_c is excluded for $R_c^{-1} < 477$ GeV, as well as masses of strongly interacting first level KK modes below 550 GeV. The result provides the first experimental limits on this UED scenario.

The Tevatron is scheduled to run through 2011 and is expected to deliver a dataset corresponding to $\approx 12 \text{ fb}^{-1}$ (a proposal is also under consideration to extend running for an additional three years, in order to obtain a final dataset of $\approx 20 \text{ fb}^{-1}$). With a $\approx 12 \text{ fb}^{-1}$ dataset, and assuming the sensitivity of the analysis techniques presented here, the projected sensitivity would be $\Lambda \approx 140$ TeV and $R_c^{-1} \approx 500$ GeV for the GMSB and UED models, respectively.

The first year of operation of the CERN Large Hadron Collider (LHC), which delivers pp collisions at $\sqrt{s} = 7$ TeV, is currently in progress. Investigations of the $\gamma\gamma + \cancel{E}_T$ final

state in early data are already underway by the ATLAS [142] and CMS [143] collaborations. As a result of the higher center-of-mass energy, and the spectrum of states predicted by the UED model, the LHC has the ability to exclude R_c^{-1} values over 500 GeV with data already recorded (several pb^{-1}). For GMSB, the LHC would primarily produce squarks and gluinos, and the limits presented here place the masses of these particles in excess of 1 TeV. The gain in sensitivity between the Tevatron and the LHC is therefore not as dramatic for the GMSB model as for the UED model. Nonetheless, the LHC will likely reach a sensitivity in excess of $\Lambda \approx 140$ TeV with the $\approx 1 \text{ fb}^{-1}$ dataset collected in the first run, which is expected to last until late 2011. After the first LHC run, the machine will be refurbished to reach the design center-of-mass energy of $\sqrt{s} = 14$ TeV.

In conclusion, the analysis presented in this dissertation significantly extends the experimental sensitivity to sources of physics beyond the Standard Model that predict the production of $\gamma\gamma + \cancel{E}_T$ events at colliders. The models considered have not been excluded, but the energy scales to which they are limited by the results of this analysis are well into the regime where the physics associated with the loss of electroweak symmetry is expected to become manifest. Additional results are expected in the near future that will supersede those presented here, and will more definitely answer the question of whether this interesting final state holds clues to how the shortcomings of the SM will be resolved.

Bibliography

- [1] N.J. Buchanan *et al.*, “ATLAS liquid argon calorimeter front end electronics”, JINST **3**, P09003 (2008).
- [2] N. J. Buchanan *et al.*, “Design and implementation of the Front End Board for the readout of the ATLAS liquid argon calorimeters”, JINST **3**, P03004 (2008).
- [3] G. Aad *et al.* (ATLAS Collaboration), “The ATLAS Experiment at the CERN Large Hadron Collider”, JINST **3**, S08003 (2008).
- [4] M. Cooke, J. Parsons, and G. Brooijmans, “Chargino Decays to Sneutrinos in the mSUGRA Coannihilation Region”, ATL-COM-PHYS-2007-002 (2007).
- [5] M. Cooke *et al.*, “In situ commissioning of the ATLAS electromagnetic calorimeter with cosmic muons”, ATL-LARG-PUB-2007-013 (2007).
- [6] M. Cooke, “Commissioning of the ATLAS Liquid Argon Calorimeters”, Proceedings from CIPANP 2009, AIP Conf. Proc. **1182**, 184 (2009) [arXiv:0910.2991].
- [7] D. Bandurin *et al.*, “Photon Identification for Run II data” , D0 Note 6004 (2009).
- [8] V.M. Abazov *et al.*, “Search for Randall-Sundrum Gravitons in the Dielectron and Diphoton Final States with 5.4 fb^{-1} of Data from $p\bar{p}$ Collisions at $\sqrt{s} = 1.96 \text{ TeV}$ ”, Phys. Rev. Lett. **104**, 241802 (2010).
- [9] M. Cooke and J. Parsons, “A search for new physics in diphoton events with large missing transverse energy”, D0 Note 6072 (2010).

- [10] V.M. Abazov *et al.*, “Search for diphoton events with large missing transverse energy in 6.3 fb^{-1} of $p\bar{p}$ collisions at $\sqrt{s} = 1.96 \text{ TeV}$ ”, submitted to Phys. Rev. Lett. [arXiv:1008.2133].
- [11] M. Cooke, “Searches for Supersymmetry with the D0 Detector at the Fermilab Tevatron”, talk presented at SUSY10 (Bonn, Germany, August 2010).
- [12] V.M. Abazov *et al.* (D0 Collaboration), Phys. Lett. B **659**, 856 (2008); D0 Note 5425 (2007). An earlier 200 pb^{-1} Run II result is presented in V.M. Abazov *et al.* (D0 Collaboration), Phys. Rev. Lett. **94**, 041801 (2005); D0 Notes 4344 (2004) and 4378 (2004).
- [13] For a review of the historical development of the gauge invariance principle, see J.D. Jackson and L.B. Okun, Rev. Mod. Phys. **73**, 663 (2001).
- [14] C.N. Yang and R.L. Mills, Phys. Rev. **96**, 191 (1954).
- [15] S.A. Bludman, Nuovo Cimento **9**, 433 (1958).
- [16] S.L. Glashow, Nucl. Phys. **22**, 579 (1961).
- [17] Y. Nambu, Phys. Rev. Lett. **4**, 380 (1960); Y. Nambu and G. Jona-Lasinio, Phys. Rev. **122**, 345 (1961); Y. Nambu and G. Jona-Lasinio, Phys. Rev. **124**, 246 (1961).
- [18] P.W. Higgs, Phys. Lett. **12**, 132 (1964); Phys. Rev. Lett. **13**, 508 (1964).
- [19] F. Englert and R. Brout, Phys. Rev. Lett. **13**, 321 (1964); G.S. Guralnik, C.R. Hagen, and T.W.B. Kibble, Phys. Rev. Lett. **13**, 585 (1964).
- [20] P.W. Anderson, Phys. Rev. Lett. **130**, 439 (1963).
- [21] J. Goldstone, Nuovo Cimento **19**, 154 (1961); J. Goldstone, A. Salam, and S. Weinberg, Phys. Rev. **127**, 965 (1962).
- [22] S. Weinberg, Phys. Rev. Lett **19**, 1264 (1967).
- [23] A. Salam, in *Elementary Particle Theory, Proc. 8th Nobel Symposium*, edited by N. Svartholm (Almqvist & Wiksell, Stockholm, 1968) p 367.

- [24] G. t'Hooft, Nucl. Phys. B **33**, 173 (1971); G. t'Hooft, Nucl. Phys. B **35**, 167 (1971); G. t'Hooft and M. Veltman, Nucl. Phys. B **44**, 189 (1972); G. t'Hooft and M. Veltman, Nucl. Phys. B **50**, 318 (1972).
- [25] S.L. Adler, Phys. Rev. **177**, 2426 (1969); J.S. Bell and R. Jackiw, Nuovo Cimento A **60**, 47 (1969).
- [26] C. Bouchiat, J. Iliopoulos, and P. Meyer, Phys. Lett. B **38**, 519 (1972).
- [27] M. Gell-Mann, Phys. Lett. **8**, 214 (1964); G. Zweig, CERN Report No. 8181/Th 401 (January 1964); CERN Report No. 8419/Th 412 (February 1964).
- [28] O.W. Greenberg, Phys. Rev. Lett. **13** 598 (1964); M.Y. Han and Y. Nambu, Phys. Rev. **139**, B1006 (1965).
- [29] D.J. Gross and F. Wilczek, Phys. Rev. Lett. **30**, 1343 (1973); H.D. Politzer, Phys. Rev. Lett. **30**, 1346 (1973).
- [30] J.D. Bjorken, Phys. Rev. **179**, 1547 (1969).
- [31] E.D. Bloom *et al.*, Phys. Rev. Lett. **23**, 930 (1969).
- [32] K. Nakamura *et al.* (Particle Data Group), Journal of Physics G **37**, 075021 (2010).
- [33] ALEPH, DELPHI, L3, OPAL, SLD, LEP Electroweak Working Group, SLD Electroweak and Heavy Flavour Groups: S. Schael *et al.*, Phys. Reports **427**, 257 (2006); for updates see <http://lepewwg.web.cern.ch/LEPEWWG/>.
- [34] H. Georgi and S.L. Glashow, Phys. Rev. Lett. **32**, 438 (1974).
- [35] J.C. Pati and A. Salam, Phys. Rev. D **8**, 1240 (1973).
- [36] H. Georgi, H.R. Quinn, and S. Weinberg, Phys. Rev. Lett. **33**, 451 (1974).
- [37] E. Gildener, Phys. Rev. D **14**, 1667 (1976); Phys. Lett. B **92**, 111 (1980).
- [38] L. Susskind, Phys. Rev. D **20**, 2619 (1979).
- [39] C.H. Llewellyn Smith and C.G. Ross, Phys. Lett. B **105**, 38 (1981).

- [40] J. Sherk, *Rev. Mod. Phys.* **47**, 123 (1975).
- [41] R.J. Eden *et al.*, *The Analytic S-Matrix*, Cambridge University Press, 1966.
- [42] P. Ramond, *Phys. Rev. D* **3**, 2415 (1971).
- [43] A. Neveu and J.H. Schwartz, *Nucl. Phys. B* **31**, 86 (1971).
- [44] J.L. Jervais and B. Sakita, *Nucl. Phys. B* **34**, 632 (1971).
- [45] Y. Golfand and E. Likhtam, *JETP Lett.* **13**, 323 (1971); D.V. Volkov and V. Akulov, *Phys. Lett. B* **46**, 109 (1973); D.V. Volkov and V.A. Soroka, *JETP Lett.* **18**, 312 (1973).
- [46] Y. Nambu, *Proc. Intl. Conf. on Symmetries and Quark Models*, Wayne State Univ. (1969); H. Nielsen, *15th Conf. on High Energy Physics*, Kiev Conference (1970); L. Susskind, *Nuovo Cimento* **69**, 457 (1970).
- [47] C. Lovelace, *Phys. Lett. B* **34**, 500 (1971).
- [48] P. Goddard and C.B. Thorn, *Phys. Lett. B* **40**, 235 (1972).
- [49] J. Scherk and J.H. Schwarz, *Phys. Lett. B* **52**, 347 (1974).
- [50] E. Cremmer and J. Sherk, *Nucl. Phys. B* **103**, 399 (1976).
- [51] J. Wess and B. Zumino, *Nucl. Phys. B* **70**, 39 (1974); *Phys. Lett. B* **49**, 52 (1974).
- [52] S. Coleman and J. Mandula, *Phys. Rev.* **159**, 1251 (1967).
- [53] R. Haag, J.T. Lopuszanski, and M. Sohnius, *Nucl. Phys. B* **88**, 257 (1975).
- [54] M.T. Grisaru, M. Rocek, and W. Siegel, *Nucl. Phys. B* **159**, 429 (1979).
- [55] P. Fayet, *Phys. Lett. B* **64**, 159 (1976); P. Fayet, *Phys. Lett. B* **69**, 489 (1977).
- [56] U. Amaldi, W. de Boer, and H. Fürstenau, *Phys. Lett. B* **260**, 447 (1991).
- [57] J. Iliopoulos, and B. Zumino, *Nucl. Phys. B* **76**, 310 (1974).
- [58] S. Dimopoulos and H. Georgi, *Nucl. Phys. B* **193**, 150 (1981); S. Dimopoulos and D. Sutter, *Nucl. Phys. B* **452**, 496 (1995).

- [59] A. Salam and J. Strathdee, Nucl. Phys. B **87**, 85 (1975); P. Fayet, Nucl. Phys. B **90**, 104 (1975).
- [60] R. Barbier *et al.*, Phys. Rept. **420**, 1 (2005).
- [61] H. Pagels and J.R. Primack, Phys. Rev. Lett. **48**, 223 (1982).
- [62] S. Ferrara, D.Z. Freedman, and P. van Nieuwenhuizen, Phys. Rev. D **13**, 3214 (1976); S. Deser and B. Zumino, Phys. Lett. B **62**, 335 (1976); For a review see P. van Nieuwenhuizen, Phys. Rep. **68**, 189 (1981).
- [63] S. Deser and B. Zumino, Phys. Rev. Lett. **38**, 1434 (1977).
- [64] M. Dine, A.E. Nelson, Phys. Rev. D **48**, 1277 (1993); M. Dine, A.E. Nelson, and Y. Shirman, Phys. Rev. D **51**, 1362 (1995); M. Dine, A.E. Nelson, Y. Nir, and Y. Shirman, Phys. Rev. D **53**, 2658 (1996); For a review see G. Giudice and R. Rattazzi, Phys. Rep. **322**, 419 (1999).
- [65] L. Alvarez-Gaume, M. Claudson, and M.B. Wise, Nucl. Phys. B **207**, 96 (1982).
- [66] S.P. Martin, Phys. Rev. D **55**, 3177 (1997).
- [67] A. Djouadi, J-L. Kneur, and G. Moultaka, Comput. Phys. Commun. **176**, 426 (2007).
- [68] B.C. Allanach *et al.*, Eur. Phys. J. C **25**, 113 (2002).
- [69] A. Djouadi, M.M. Muhlleitner, and M. Spira, Acta Phys. Polon. B **38**, 635 (2007).
- [70] W. Beenakker *et al.*, Phys. Rev. Lett. **83**, 3780 (1999).
- [71] P. Fayet, Phys. Lett. B **70**, 461 (1977); Phys. Lett. B **86**, 272 (1979).
- [72] A. Heister *et al.* (ALEPH Collaboration), Eur. Phys. J. C **28**, 1 (2003); J. Abdallah *et al.* (DELPHI Collaboration), Eur. Phys. J. C **38**, 395 (2005); P. Archard *et al.* (L3 Collaboration), Phys. Lett. B **587**, 16 (2004); G. Abbiendi *et al.* (OPAL Collaboration), Phys. Lett. B **602**, 167 (2004).
- [73] B. Abbott *et al.* (D0 Collaboration), Phys. Rev. Lett. **80**, 442 (1998); F. Abe *et al.* (CDF Collaboration), Phys. Rev. D **59**, 092002 (1999).

- [74] T. Aaltonen *et al.* (CDF Collaboration), Phys. Rev. Lett. **104**, 011801 (2010); D. Acosta *et al.* (CDF Collaboration), Phys. Rev. D **71**, 031104 (2005).
- [75] R. Culbertson *et al.*, “Low-Scale and Gauge-Mediated Supersymmetry Breaking at the Fermilab Tevatron Run II,” [arXiv:hep-ph/0008070v2].
- [76] E. Witten, Nucl. Phys. B **471**, 135 (1996); J. D. Lykken, Phys. Rev. D **54**, 3693 (1996).
- [77] I. Antoniadis, Phys. Lett. B **246**, 377 (1990).
- [78] K.R. Dienes, E. Dudas, and T. Gherghetta, Phys. Lett. B **436**, 55 (1998).
- [79] N. Arkani-Hamed, S. Dimopoulos, and G. Dvali, Phys. Lett. B **429**, 263 (1998).
- [80] L. Randall and R. Sundrum, Phys. Rev. Lett. **83**, 3370 (1999).
- [81] T. Appelquist, H.C. Cheng, and B.A. Dobrescu, Phys. Rev. D **64**, 035002 (2001).
- [82] A. Datta, K. Kong, and K.T. Matchev, [arXiv:1002.4624].
- [83] H. Cheng, K. Matchev, and M. Schmaltz, Phys. Rev. D **66**, 036005 (2002).
- [84] M. ElKacimi *et al.*, Comput. Phys. Commun. **181**, 122 (2010).
- [85] C. Macesanu, C.D. McMullen, and S. Nandi, Phys. Rev. D **66**, 015009 (2002).
- [86] H. Cheng, K. Matchev and M. Schmaltz, Phys. Rev. D **66**, 056006 (2002).
- [87] C. Macesanu, C. D. McMullen, and S. Nandi, Phys. Lett B **546**, 253 (2002).
- [88] A. DeRujula *et al.* Phys. Lett B **482**, 195 (2000).
- [89] T.G. Rizzo, Phys. Rev. D **64**, 095010 (2001).
- [90] C. Macesanu Int. J. Mod. Phys. A **21**, 2259 (2006).
- [91] F.T. Cole (Ed.), E.L. Goldwasser (Ed.), and R. R. Wilson, (Ed.), “National Accelerator Laboratory design report”, FERMILABDESIGN-1968-01 (1968)
- [92] TeVI Group, “Design report Tevatron 1 project”, FERMILAB-DESIGN-1984-01.

- [93] P.C. Bhat and W.J. Spalding, “Fermilab collider Run II: accelerator status and upgrades”, AIP Conf. Proc. **753**, 30 (2005)[hep-ex/0410046].
- [94] S. Abachi *et al.* (D0 Collaboration), Nucl. Inst. Methods A **338**, 185 (1994).
- [95] S. Abachi *et al.*(D0 Collaboration), “The D0 upgrade: the detector and its physics”, FERMILAB-PUB-96/357-E (1996).
- [96] V.M. Abazov *et al.* (D0 Collaboration), Nucl. Instrum. Methods A **565** (2006) 463.
- [97] D0 Upgrade Collaboration, “D0 silicon tracker technical design report”, available online at: http://d0server1.fnal.gov/projects/silicon/www/silicon_old.html.
- [98] M. Weber, “The D0 silicon micro-strip tracker”, Nucl. Inst. Methods A **560**, 14 (2006).
- [99] D0 Upgrade Collaboration, “The D0 upgraded central fiber tracker technical design report”, available online at: http://d0server1.fnal.gov/projects/scifi/cft_home.html.
- [100] M. Adams *et al.*, “Design report of the central preshower detector for the D0 upgrade”, D0 Note 3014 (1996).
- [101] M. Bhattacharjee *et al.*, “Technical design report of the forward preshower detector for the D0 upgrade”, D0 Note 3445 (1998).
- [102] U. Bassler, “Online calorimeter calibration procedures and database design”, D0 Note 5316 (2007).
- [103] G. Bernardi *et al.*, “Improvements from the T42 algorithm on calorimeter objects reconstruction”, D0 Note 4335 (2004).
- [104] G. Bernardi and S. Trincaz-Duvoid, “Improvements of the NADA algorithm”, D0 Note 4057 (2002).
- [105] F. Couderc, “D0 Switch Capacitor Array Failures, Description and Detection”, D0 Note 5231 (2006).
- [106] T. Andeen *et al.*, “The D0 experiment’s integrated luminosity for Tevatron Run IIa”, FERMILAB-TM-2365 (2007).

- [107] D0 Algorithms Group, “How to run RECO”, available online at: <http://www-d0.fnal.gov/computing/algorithms/howto/howtoreco.html>.
- [108] H. Greenlee, “The D0 Kalman Track Fit”, D0 Note 4303 (2004).
- [109] A. Khanov, “HTF: histogramming method for finding tracks. The algorithm description”, D0 Note 3778 (2002).
- [110] G. Borissov, “Ordering a Chaos or... Technical Details of AA Tracking”, available online at: http://www-d0.fnal.gov/global_tracking/talks/20030228/talk-adm-030228.ps, (2003).
- [111] O. Atramentov, Y. Maravin, “Utilizing CFT and SMT hit counts for photon and electron reconstruction”, D0 Note 4444 (2004).
- [112] A. Schwartzman and C. Tully, “Primary Vertex Reconstruction by Means of Adaptive Vertex Fitting”, D0 Note 4918 (2005).
- [113] A. Schwartzman and M. Narain, “Probabilistic Primary Vertex Selection”, D0 Note 4042 (2002).
- [114] D. Cho, presentation at October 2009 D0 Collaboration Meeting - Tralgo Session, October 1, 2009.
- [115] F. Fleuret, “The D0 Electron and Photon Analysis Package EMAnalyze”, D0 Note 3888.
- [116] D. Chapin *et al.*, “Measuring $Z \rightarrow ee$ and $W \rightarrow e\nu$ Production Cross Sections Using One Tight Central Electron”, D0 Note 4897 (2005).
- [117] T. Andeen, J. Hays, and H. Schellman, “Electron Level Energy Correction in D0 Reconstruction p14 pass 2”, D0 Note 5104 (2006).
- [118] Y. Maravin, “Optimization of central track matching to electromagnetic objects by utilizing central preshower stereo clusters”, D0 Note 4411 (2004).
- [119] S.I. Kesisoglou, “Search for Gauge Mediated Supersymmetry in the $\gamma\gamma + \cancel{E}_T$ channel”, PhD Thesis, Brown University (2005).

- [120] G.C. Blazey *et al.*, “Run II Jet Physics: Proceedings of the Run II QCD and Weak Boson Physics Workshop”, [arXiv:hep-ex/0005012v2].
- [121] Aurelio Juste and Christophe Royon, “D0Preliminary Jet Energy Scale”, http://www-d0.fnal.gov/phys_id/jes/public/plots_v7.1/.
- [122] S. Trincaz-Duvoid, P. Verdier, “Missing ET Reconstruction in p17”, D0 Note 4474 (2004).
- [123] S. Calvet, P. Verdier, E. Kajfasz, “Towards MissingET Certification and Unclustered Energy Studies”, D0 Note 4927 (2005).
- [124] A. Dubey, “Missing ET in ZBMB Events”, presentation in Missing E_T Workshop, D0 Collaboration Meeting, Dec 8 2009.
- [125] D0 Common Samples Group: <http://www-d0.fnal.gov/Run2Physics/cs/index.html>
- [126] D0 Data Quality Group:
http://www-d0.fnal.gov/computing/data_quality/d0_private/forusers.html
- [127] D0 Trigger Studies Group: <http://www-d0.fnal.gov/computing/algorithms/tsg/tsg.html>.
D0 Notes 5409 (2007); 5783 (2008).
- [128] T. Sjostrand, S. Mrenna, and P. Skands, *Comput. Phys. Commun.* **135**, 238 (2001).
- [129] M.L. Mangano *et al.*, *J. High Energy Phys.* **07**, 001 (2003).
- [130] J. Alwall *et al.*, *J. High Energy Phys.* **09**, 028 (2007).
- [131] J. Pumplin *et al.*, *J. High Energy Phys.* **07**, 012 (2002); D. Stump *et al.*, *J. High Energy Phys.* **10**, 046 (2003).
- [132] R. Brun and F. Carminati, CERN Program Library Long Writeup W5013, 1993 (unpublished).
- [133] D. Bandurin, “Artificial neural network for photon selection”, D0 Note 5245 (2006).
- [134] X. Bu, Y. Liu, “Artificial neural network for Run IIb electron and photon identification”, D0 Note 5545 (2007).

- [135] V. M. Abazov *et al.* (D0 Collaboration), Phys. Rev. Lett. **102** (2009) 231801; D0 Notes 5846 (2009) and 5859 (2009).
- [136] V. M. Abazov *et al.* (D0 Collaboration), Phys. Lett. B **690**, 108 (2010); D0 Note 5959 (2009).
- [137] A. Askew, D. Duggan, “CPS variables for Photon Identification”, D0 Note 4949 (2005).
- [138] U. Baur, T. Han, J. Ohnemus, Phys. Rev. D **48** 5140 (1993).
- [139] K. Harder, “PDF systematics in CAF”, presentation in Common Samples Group Meeting, D0 Collaboration Meeting, June 21 2006.
- [140] T. Junk, Nucl. Instrum. Methods A **434** (1999) 435; A. Read, CERN 2000-005 (2000).
- [141] W. Fisher, FERMILAB-TM-2386-E; D0 Notes 5309 (2006), 5595 (2009), and 5818 (2009).
- [142] X. Anduaga *et al.*, “Search for a two photon + ETmiss final state in $\sqrt{s} = 7$ TeV pp collisions at the LHC using the ATLAS detector in the context of the One Universal Extra Dimension model with gravity mediated decays”, ATL-COM-PHYS-2010-534 (2010); ATL-PHYS-INT-2009-033 (2009); ATL-COM-PHYS-2009-071 (2009).
- [143] B. Heyburn, “Searches for SUSY in Di-photon Events”, talk presented at SUSY10 (Bonn, Germany, August 2010).

Appendix A

Distributions of Kinematic Variables

This appendix presents for reference several distributions of kinematic variables for the $\gamma\gamma$ sample, for several data control samples, and for example signal model points. The variables shown are the invariant mass of the two EM clusters, the leading and trailing cluster E_T values and their sum, the jet multiplicity, and leading jet p_T . After the figures of these distributions, several $\Delta\phi$ variable distributions are shown for the example signal model points. The variables are $\Delta\phi$ between \cancel{E}_T and the leading photon, $\Delta\phi$ between \cancel{E}_T and the trailing photon, the smaller of these two values, and $\Delta\phi$ between the two photons.

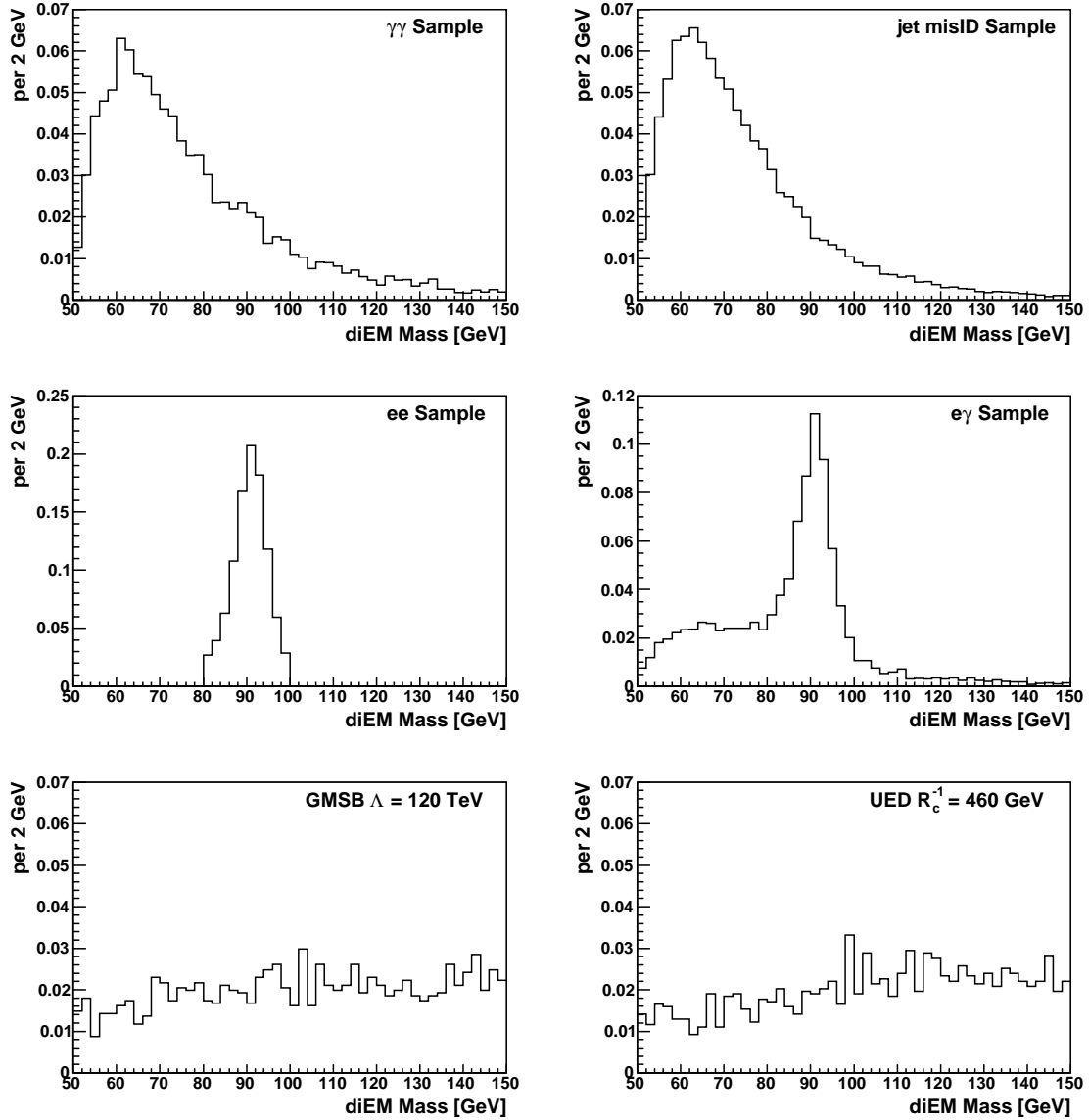


Figure A.1: Unit normalized distributions of diEM invariant mass for various data samples and example signal model points.

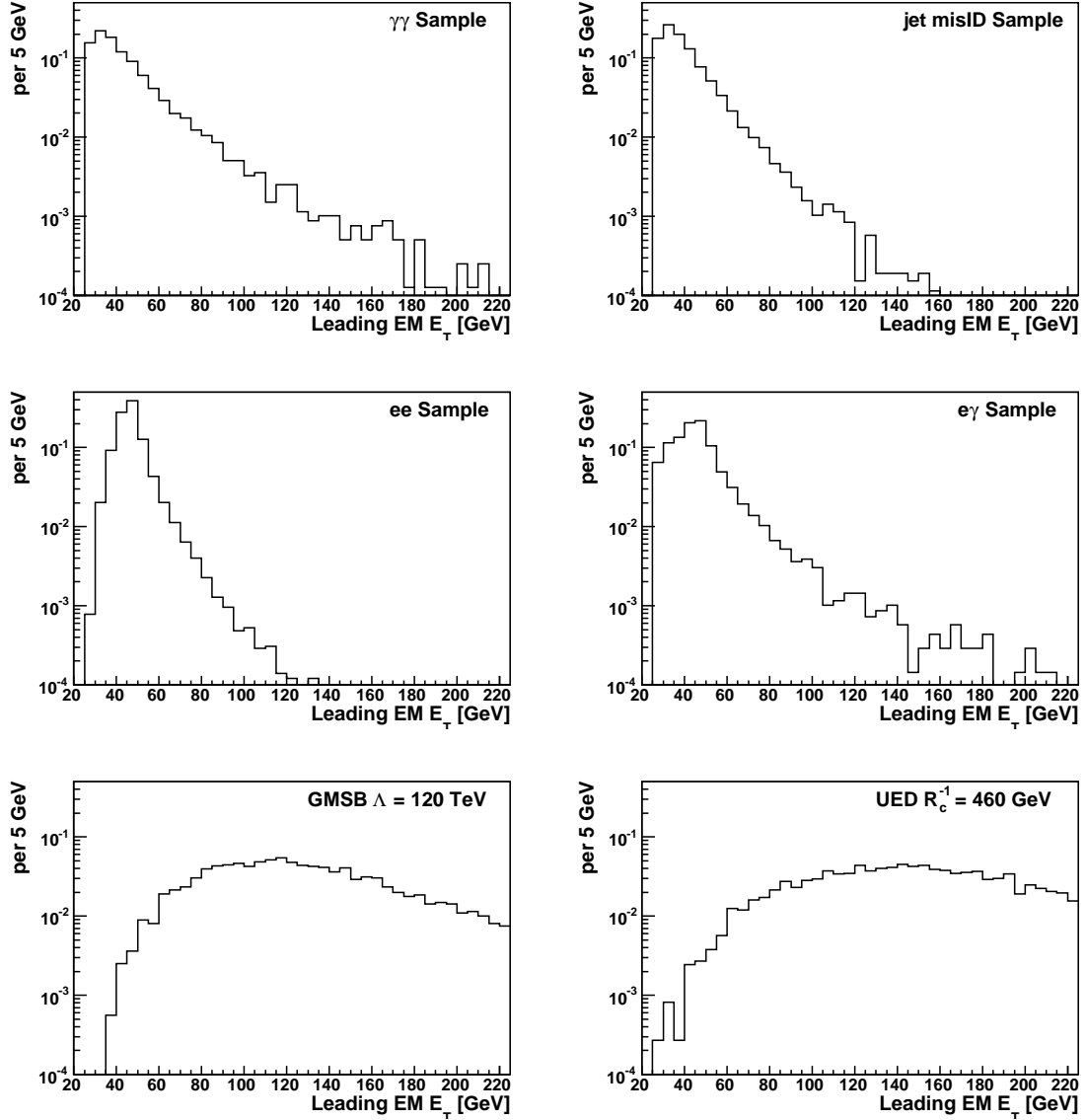


Figure A.2: Unit normalized distributions of leading EM cluster E_T for various data samples and example signal model points.

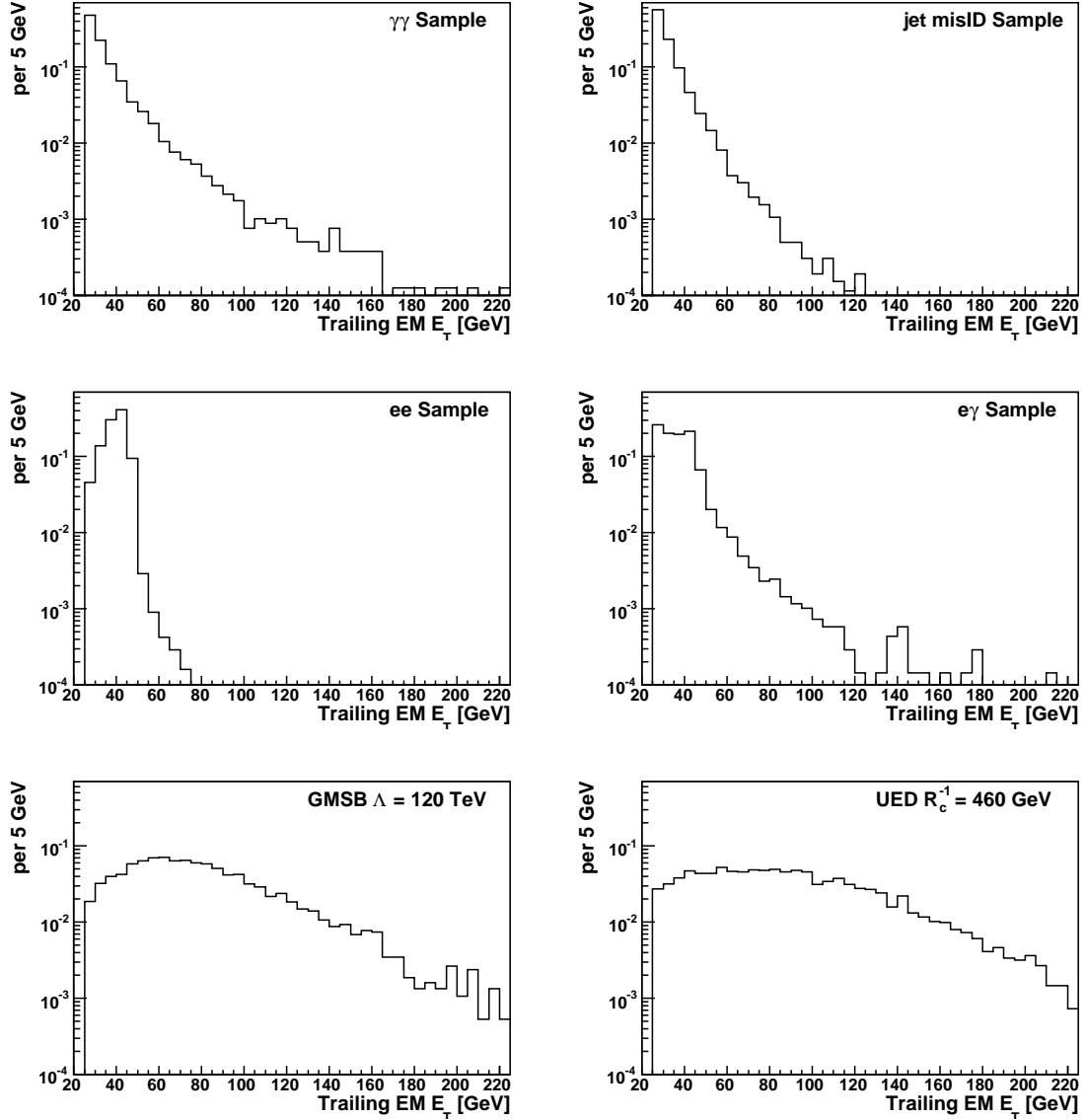


Figure A.3: Unit normalized distributions of trailing EM cluster E_T for various data samples and example signal model points.

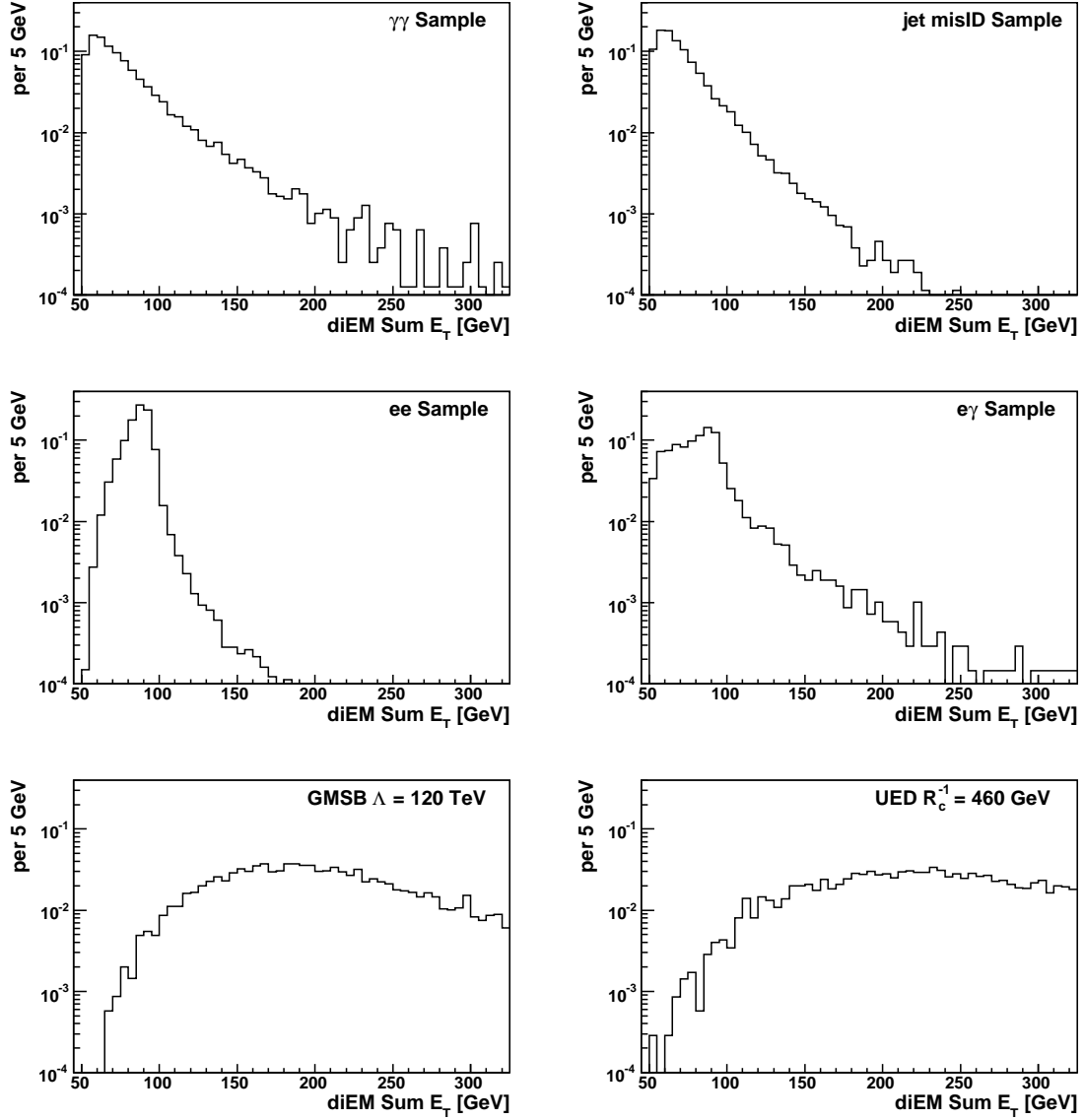


Figure A.4: Unit normalized distributions of the sum of EM cluster E_T for various data samples and example signal model points.

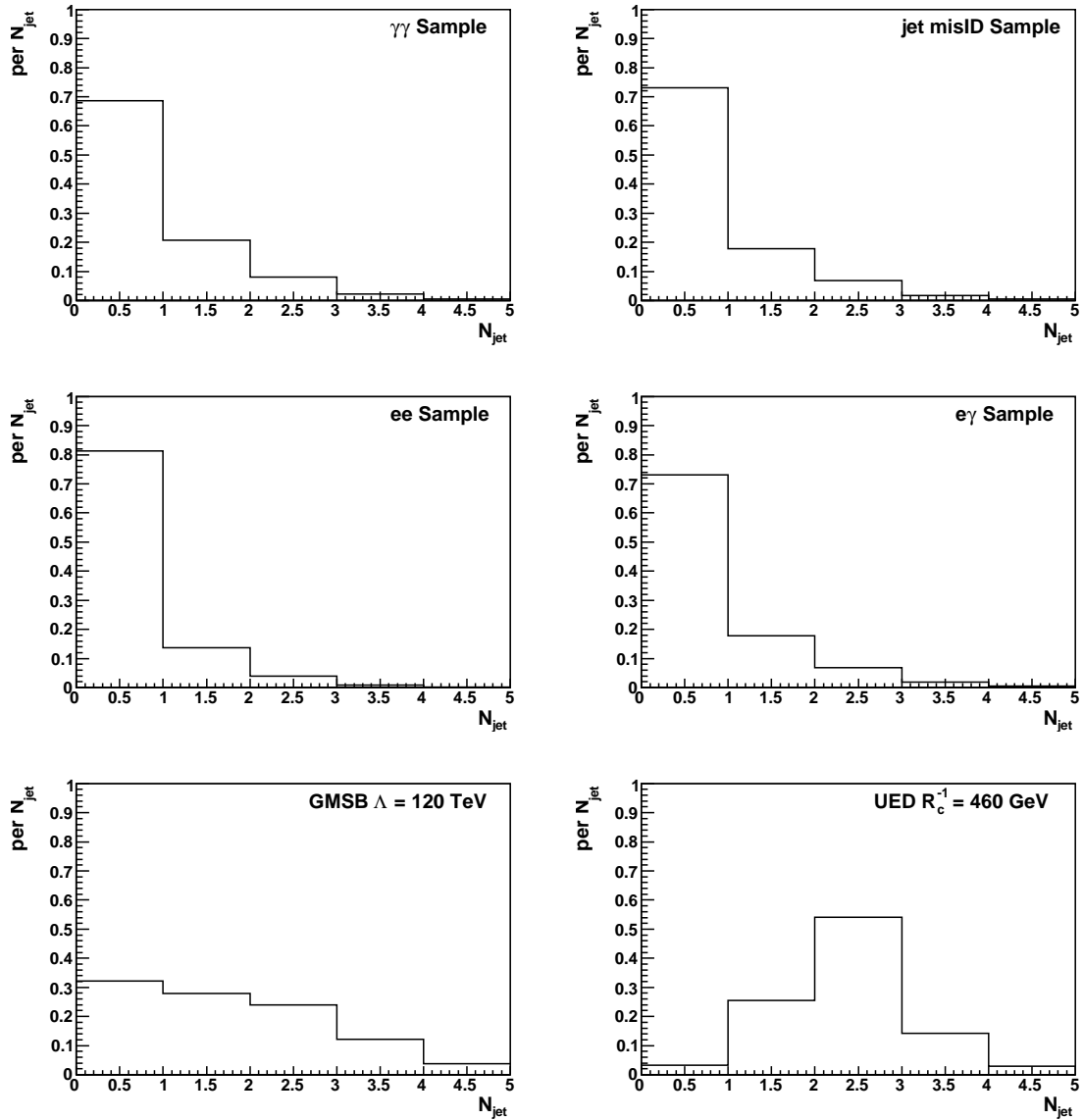


Figure A.5: Unit normalized distributions of jet multiplicity for various data samples and example signal model points.

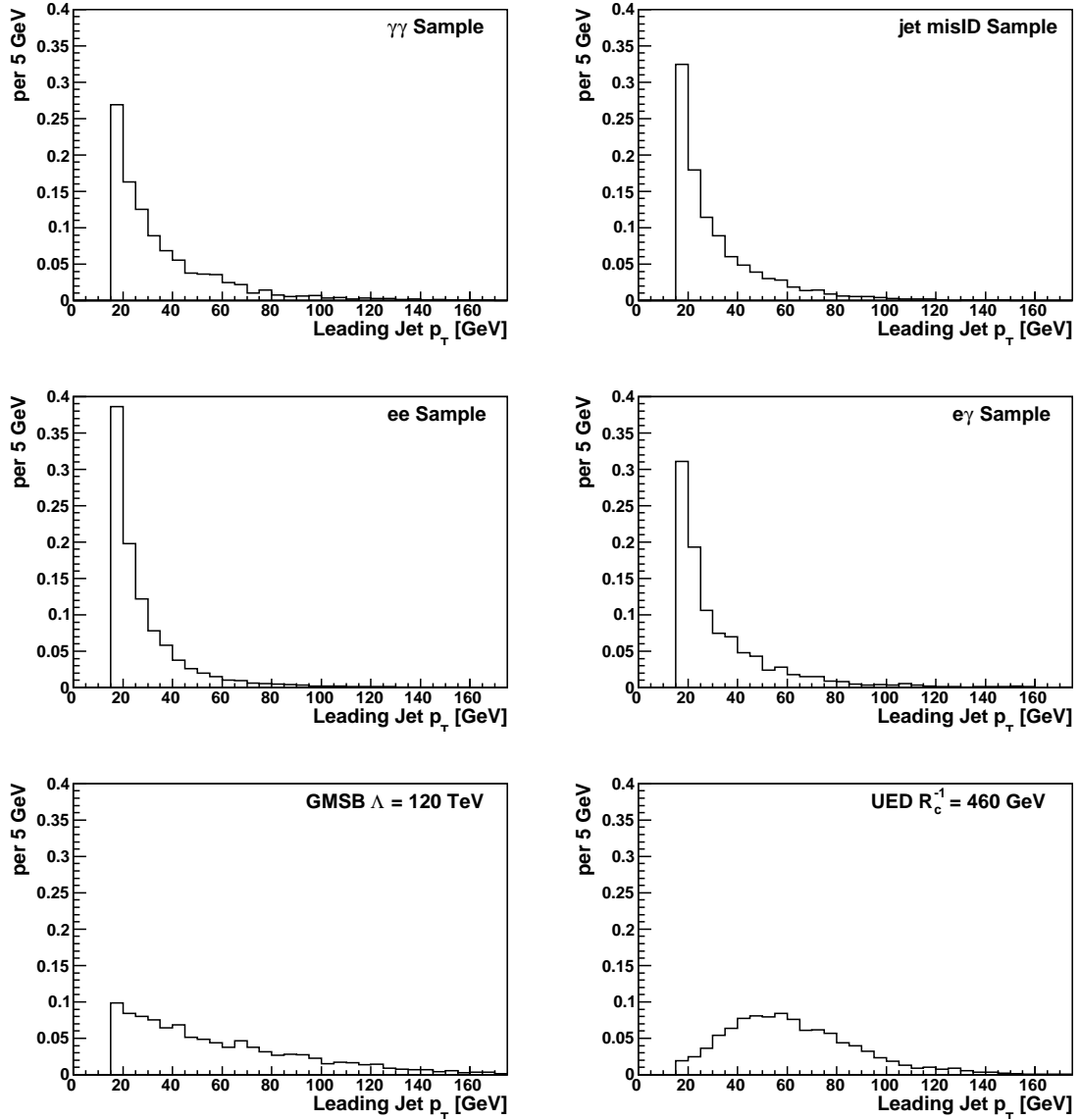


Figure A.6: Unit normalized distributions of leading jet p_T for various data samples and example signal model points.

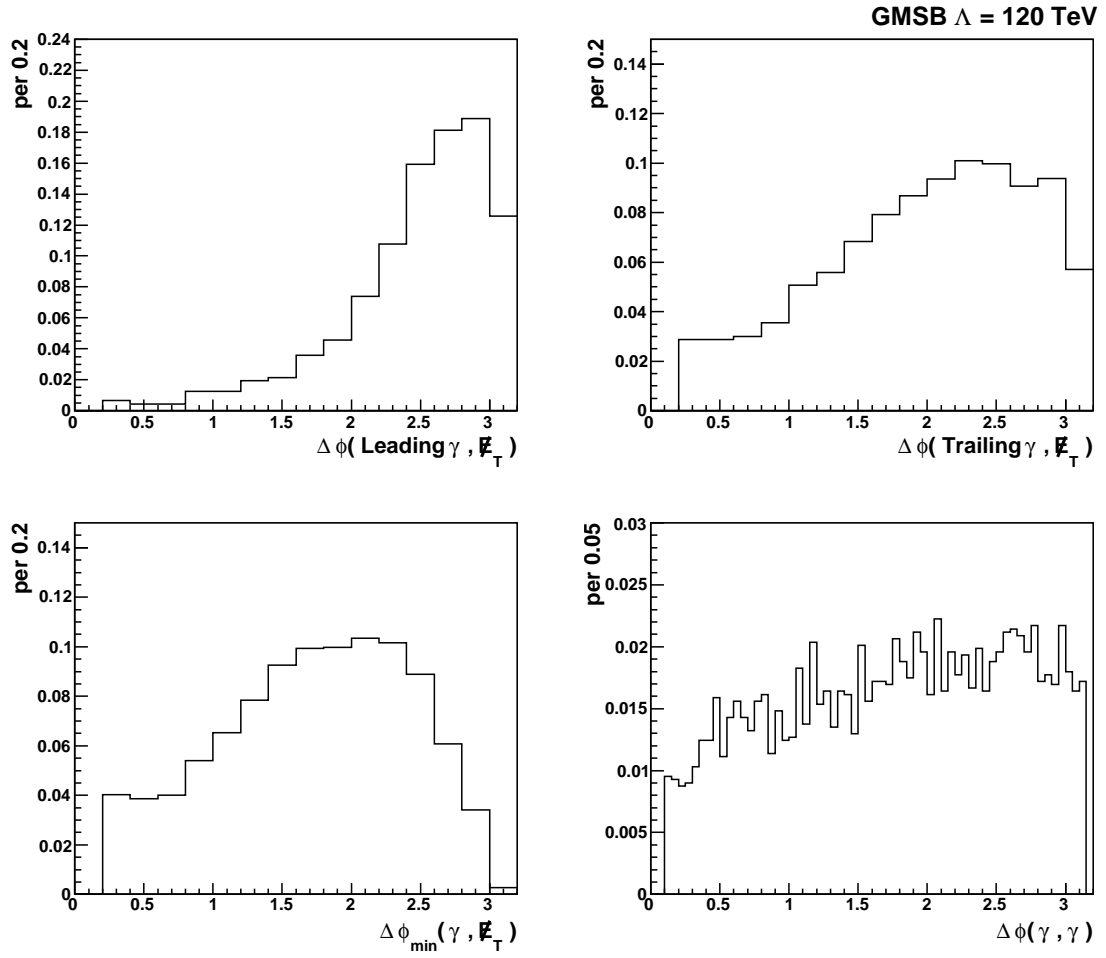


Figure A.7: Unit normalized distributions of $\Delta\phi$ variables for GMSB at $\Lambda = 120$ TeV.

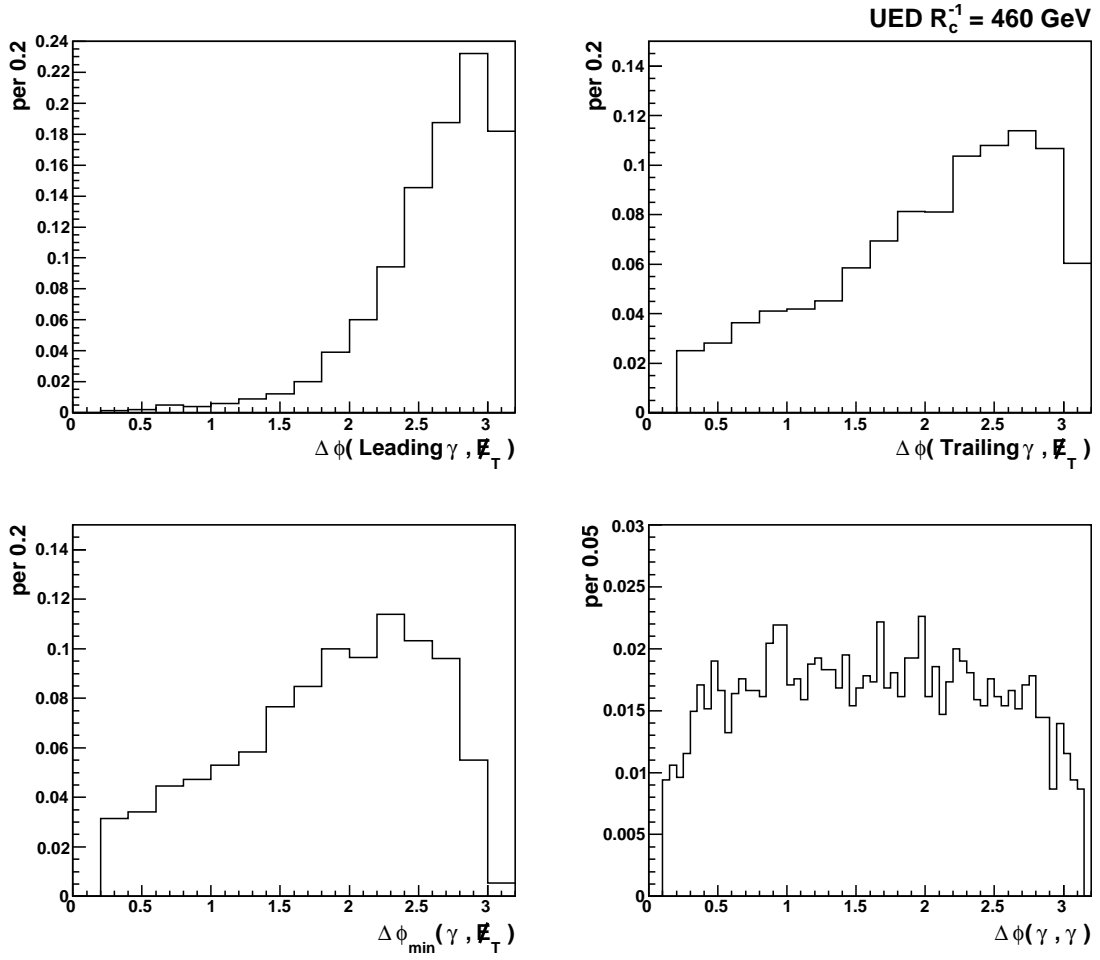


Figure A.8: Unit normalized distributions of $\Delta\phi$ variables for UED at $R_c^{-1} = 460$ GeV.